공학박사 학위논문

금속–기체 전지 화학을 이용한 차세대 대용량 이차전지 개발에 관한 연구

Exploring metal–gas chemistry for development of high-energy secondary batteries

2019 년 2 월

서울대학교 대학원

재료공학부

박 혁 준

Abstract

Exploring metal–gas chemistry for development of high-energy secondary batteries

Hyeokjun Park
Department of Materials Science and Engineering
College of Engineering
The Graduate School
Seoul National University

Nowadays, the demands for energy storage devices are explosively increasing with the market growth of energy storage applications including electric vehicles (EV) and large-scale energy storage systems (ESS). Li ion batteries are now regarded as the state-of-art energy storage chemistry owing to their high energy density and power density which satisfies requirements for the power sources of current portable electronic devices. However, current energy density of Li ion batteries is insufficient to be utilized in huge applications including EV and ESS because of the use of heavy transition metal compounds and limited storage capability of current cathode materials. Many research efforts have been devoted to discovery on next-generation energy storage chemistries (including Li–O_2, Li–S, and

Na ion batteries *etc.*) which can outperform current Li ion batteries. Among them, Li–O_2 batteries have attracted enormous attentions owing to the extraordinary high theoretical energy density with the absence of heavy elements. However, poor efficiency and reversibility in Li–O_2 chemistry hinders the practical realization of Li–O_2 batteries to date.

In this thesis, I explore novel metal–gas chemistry for devising new rechargeable batteries. Coupling various gas-phase actve materials with counter metal electrode can be an alternative to develop highly efficient and reversible secondary batteies, taking knowledge from the historical background and fundamental understnading on the Li–O_2 batteries. Here, I invent a new secondary battery chemistry by revisiting primary Li–SO_2 systems and develop high-performing Li–SO_2 batteries based on in-depth understanding on the energy storage mechanism. In addition, I enlighten a superoxide chemistry in recent emerging Na–O_2 batteries by addressing the chemical behaviors of discharge products and develop highly durable Na–O_2 batteries through the introduction of advanced electrolytes to control the discharge product.

Chapter 2 shed a new light on old primary Li–SO_2 battery chemistry as a way to devise a new secondary battery. Although primary Li–SO_2 battery has been only believed as a primary battery due to the foramtion of solid discharge prodcuts, a rechargeability of Li–SO_2 battery is demonstrated based on the reversible formation and decomposition of $Li_2S_2O_4$ discharge product. Novel rechargeable Li–SO_2 battery with the operation voltage of ~2.8 V and capacity of 5,400 mA h g^{-1} exhibits higher energy efficiency and cell reversibility compared to the Li–O_2

chemistry. Based on in depth mechanism studies on the critical role of electrolytes properties, conventional carbonate-based electrolytes, which have been widely used for practical Li ion batteries but not for current Li–O_2 battery, are exploited in Li–SO_2 rechargeable batteries. Li–SO_2 battery with carbonate-based electrolytes presents superior electrochemical properties including high power and reversibility. Application of soluble catalysts into newly developed Li–SO_2 battery is also demonstrated with achieving one of the most outstanding performances among previous Li–gas type batteries.

Chapter 3 reveals the origin of discrepency in discharge products and underlying reaction mehcanism of Na–O_2 batteries. NaO_2 chemistry has recently attracted many interests owing to extremely low charge polarizations about 200 mV of Na–O_2 batteries. It is unveiled that the spontaneous dissolution and ionization of primary discharge product NaO_2 liberates the free O_2^- in the electrolyte and promotes side reactions involving the formation of $Na_2O_2 \cdot 2H_2O$. The chemical phase transition results in higher polarization for charge process of Na–O_2 batteries with severe deterioration of cell efficiency and reversibility. On the basis of the mechanism, rational tuning of electrolyte is addressed to prevent the dissolution of NaO_2. The introduction of concentrated electrolytes with little amount of free solvents is verified to suppress chemical product transition from NaO_2 to $Na_2O_2 \cdot 2H_2O$ during storage period of Na–O_2 batteries. Highly durable Na–O_2 batteries is developed for longer shelf-life through the stabilization of NaO_2 with the use of concentrated electrolytes.

I believe that this thesis can open up a new research frontier of metal–gas type secondary high-energy battery and provide insights on the fundamental understanding of the energy storage mechanism of metal–gas batteries. The revisit study on Li–SO_2 battery in this thesis can also offer an avenue to devise a new rechargeable battery chemistry. In addition, successful electrolytes design and catalysts engineering in this thesis also provide guidelines how to develop high-performing metal–gas type rechargeable batteries.

Keywords: Electrochemistry, Secondary batteries, Metal-air batteries, Sulfur dioxide, Superoxide, Electrolytes, Soluble Catalysts.

Student Number: 2014-21476

Contents

List of Tables

List of Figures

sulfur dioxide cells with TEGDME electrolyte. (b) XRD pattern of discharged electrode of lithium–sulfur dioxide cells. (c–f) SEM images of discharge products on the carbon cathodes with (c,d) ether electrolyte and (e,f) carbonate electrolyte.

Figure 2.14. Electrochemical performance of lithium–sulfur dioxide batteries. (a,b) Discharge rate capability of lithium–sulfur dioxide cell: (a) with carbonate electrolyte, (b) with ether electrolyte, (c) Cycle properties of lithium–sulfur dioxide cells at 0.2 mA cm^{-2}. (d) Electrochemical profiles of lithium–sulfur dioxide cells with a soluble catalyst. (e) XRD spectra of discharged and recharged gas-electrode of lithium–sulfur dioxide cell with soluble catalyst. (f,g) Electrochemical performance of lithium–sulfur dioxide cells with soluble catalyst containing carbonate-based electrolyte: (f) Power capability of the cells under limited capacity of 0.5 mAh. (g) Cyclability of the cell at 1 mA cm^{-2}. (inset: electrochemical profiles during 450 cycles.)

Figure 2.15. Identification of discharge products and corresponding morphological observations. (a) XRD patterns of discharged cathode of lithium–sulfur dioxide cells with different current densities. (b–e), Corresponding SEM images of discharged cathodes at (b) 3 mA/cm^2, (c) 5 mA/cm^2, (d) 7.5 mA/cm^2, and (e) 10 mA/cm^2. The high-intensity peaks at 44° correspond to the Ni mesh current collector. Ni mesh was used particularly for the rate capability tests to achieve a high electric conductivity for the current collecting substrate when applying a high current density.

Figure 2.16. Cycle properties under a capacity of 1,000 mAh/g of lithium-sulfur

dioxide batteries with carbonate-based electrolytes.

Figure 2.17. Electrochemical properties of lithium–sulfur dioxide cells with carbonate electrolyte at high current density of 1 mA/cm^2. (a) Galvanostatic discharge/charge profiles of lithium–sulfur dioxide cells at 1 mA/cm^2 with voltage cut-offs of 2 and 4.5 V. (b) Electrochemical profiles of lithium–sulfur dioxide cells at 1 mA/cm^2 with capacity cut-off of 500 mAh/g for 5 cycles. (c) Corresponding cyclability of lithium–sulfur dioxide cells.

Figure 2.18. Redox potentials of DMPZ soluble catalyst under different electrolytes. (a) Cycle voltammogram of 50 mM DMPZ dissolved in 1 M $LiPF_6$ in EC/DMC at a scan rate of 100 mV/s with 3-electrode cell configuration. (working electrode: gold; counter electrode: platinum; reference electrode: 0.05 M $Ag/AgNO_3$ in acetonitrile) (b) Galvanostatic charge profiles of 50 mM DMPZ dissolved in 1 M $LiPF_6$ in EC/DMC and TEGDME at 0.2 mA/cm^2 under Ar atmosphere with 2-electrode cell configuration.

Figure 2.19. Electrochemical activity of DMPZ soluble catalyst in lithium–sulfur dioxide cells with carbonate electrolyte. (a) *Ex situ* XPS results of discharged and charged cathodes for lithium–sulfur dioxide cells with DMPZ catalyst. (b) *In situ* gas analysis results of lithium–sulfur dioxide cells with DMPZ catalyst during charge through DEMS.

Figure 2.20. Investigation of cycle degradation of lithium–sulfur dioxide batteries. (a,b) Cycle properties of rebuilt cells with cycled gas-electrode or cycled lithium anode: (a) under carbonate electrolyte. (b) under ether electrolyte. (c) Lithium symmetric cell test at a current density of 1

chemical reaction, NaO_2 is dissolved and ionized into the electrolyte (Reaction 3), which promotes the undesired degradation of the electrolyte (Reaction 4–6). $Na_2O_2{\cdot}2H_2O$ is formed during the subsequent chemical reactions (Reactions 7, 8).

Figure 3.11. (a) Symmetric cell configuration to generate O_2^-. The electrolyte was used with 10 mM $TBAClO_4$ in DEGDME and the electrode was used with commercial carbon GDL. (b) The electrochemical profile of simulated ORR experiment with the symmetric cell. The applied current was 0.1 mA and the controlled capacity was 5 mAh. (c) FTIR spectra and (d) Iodometric determinations of the electrolyte with simulated ORR.

Figure 3.12. XRD pattern of the chemically synthesized $Na_2O_2{\cdot}2H_2O$ according to the proposed mechanism. All the synthesis and characterizations were carried out in the Ar-filled glovebox.

Figure 3.13. Deep discharge profiles of sodium–oxygen battery using electrolytes with different concentration. The cell with 0.5 M electrolyte (red line) could deliver approximately 4.4 mAh discharge capacity at absolute current of 0.1 mA, which corresponds to the areal capacity of 3.47 mAh/cm^2, whereas slightly lower capacity of 3.7 mAh (2.93 mAh/cm^2) was obtained for that with 3 M electrolyte (blue line).

Figure 3.14. Detrimental effect of resting periods on the electrochemical properties of sodium–oxygen cells with conventional electrolytes. (a) Charge/discharge profiles of sodium–oxygen cells with various resting times from 6 to 24 h after discharge. (b) Pressure monitoring during discharge and (c) real-time gas profiles during charge of

between salt concentration and Cl–O bond intensity at ~945 cm^{-1}. (c) Raman spectra of linear ether family (DME, DEGDME, and TEGDME). (d) Magnified Raman spectra for the Raman shift within the range of 780–900 cm^{-1}.

Figure 3.19. Full infrared spectra of $NaClO_4$ in DEGDME electrolytes for wavenumbers from 750 to 3250 cm^{-1} as a function of concentration.

Figure 3.20. Schematic illustration of hypothetical solvation structures of $NaClO_4$ in DEGDME electrolytes. (a) SSIP structure in dilute (0.5 mol dm^{-3}) electrolytes. (b) CIP structure in concentrated (3 mol dm^{-3}) electrolytes. (Dark gray – C, Gray – H, Red – O, Purple – Na, Green – Cl) Figure 3.20 presents solvated Na^+ structures in two representative electrolyte systems (0.5 and 3 M), which show that Na^+ ions are in six O coordination of solvent-separate ion pair (SSIP) in a dilute solution and have five C–O–C bonds by contact ion pair (CIP) in a high-concentration system. Notably, the ratio of coordinating solvents in the high-concentration systems is approximately 72% for the 3 M system, which coincides with the value estimated from the Raman spectra in the Figure 3.17a.

Figure 3.21. Time-resolved characterizations of discharged electrode immersed in different electrolytes. (a) *Ex situ* XRD patterns of discharged electrodes retrieved from sodium–oxygen cells with aging in conventional electrolytes. (b) SEM images of as-discharged electrodes and (c) discharged electrodes stored for 1 day in conventional electrolytes. (d) *Ex situ* XRD patterns and (e) Raman spectra of discharged electrodes retrieved from sodium–oxygen cells

cell tests under a current density of 0.1 mA for 2.5 h within ±1.5 V.

Chapter 1. Introduction

1.1 Motivation and objectives

Energy and environmental issues such as exhaustion of fossil fuels and global warming have been continued for a few decades and now considered as one of the most serious problems. In response to these problems, electric vehicles (EV) and energy storage system (ESS) have been suggested as the key solution, leading to accelerating the development of renewable energy sources and applications. Among several candidates for energy storage systems, Li based rechargeable batteries have been considered as the most promising system due to their excellent performances. In particular, Li ion batteries have been regarded as the state-of-the-art in the battery field due to high energy and power density, which has been already successfully commercialized to portable devices. The working mechanism of Li ion battery is reversible lithium ion insertion/extraction within crystal framework of electrode materials. However, there is a critical limitation in improving gravimetric energy density of conventional Li ion batteries because their cathode materials use heavy transition metal based crystal structure as a redox host for Li ion storage. Since huge applications including EV and ESS require batteries which have much higher energy density beyond current Li ion batteries, the development of a next-generation battery with high energy density lies at the heart of the emerging energy storage technologies.[1-7]

Exploring a new metal-gas chemistry possesses an important key to open

the new possibility of ultra-high energy density battery since it offers exceptionally high energy density owing to the absence of heavy transition metals. Although it was previously conceived that a metal-gas system was only suitable for primary batteries, current Li–O_2 system has now become one of the most promising candidates for next-generation secondary batteries.[8] Despite intensive studies on the Li–O_2 battery to date, poor efficiency and reversibility of Li–O_2 chemistry impose a great huddle for realizing a practical commercialization of the batteries.[9-11] In this light, the objective of the thesis is mainly discovering new redox materials couples in metal-gas systems whose chemistry is highly reversible to devise a new battery that can realize both high energy density and efficiency as described in Figure 1.1.

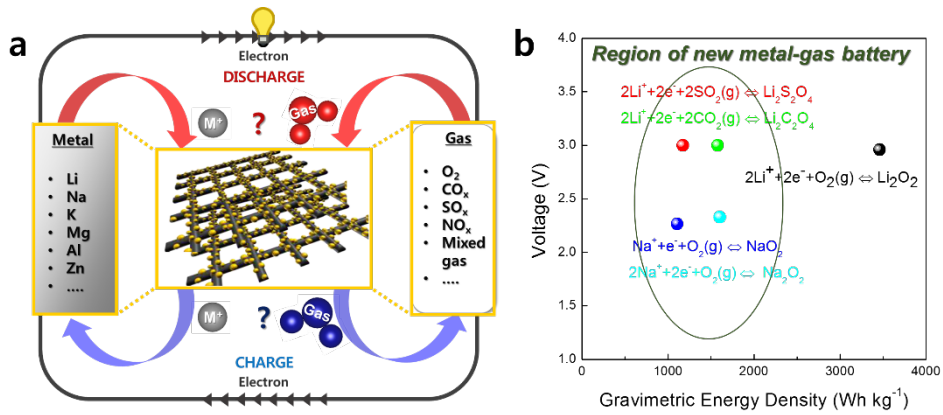

Figure 1.1. (a) Schematic description of working concept for rechargeable metal–gas battery. (b) Plots of theoretical voltage versus gravimetric energy density of several possible metal–gas compounds.

1.2 Introduction to metal–air battery

Metal–air battery has been regarded as one of the most promising next-generation energy storage devices owing to the highest theoretical energy density. Metal–air battery consists of metal anode and porous carbon cathode which offers reaction sites of electrochemically active gas phase materials separated by selective ion-conducting organic electrolytes. Based on the cell configuration, the battery is working based on the direct electrochemical reaction between metal and gas active materials without the need for heavy transition metals redox centers and crystal framework to store guest ion. Main energy conversion/storage mechanism of metal–air battery stems from the electrochemical conversion of gas-phase active materials to solid-phase ionic compounds with the combination of alkali metal species. In general, the reactions can be simply described as below.

(Anode) $\mathrm{AM(s)} \rightarrow AM^{+} + e^{-}$ (1)

(Cathode) $\mathrm{G(g)} + e^{-} \rightarrow G^{-}$ (2)

(Total) $\mathrm{xAM(s)} + \mathrm{yG(g)} \rightarrow AM_xG_y(s)$ (3)

(AM: Alkali metal, G: Gas-phase active materials, x, y: Stoichiometric index)

Accordingly, electrochemical properties of metal–air batteries are primarily dependent on the electrochemical activity of gaseous active materials (Figure 1.2a) and the energetics of their intermediate species (Figure 1.2b). Finally, the phase of discharge product is defined based on the phase stability of the complex between alkali metal and gas species (Figure 1.2c). Besides, materials natures of the solid

discharge products including electric conductivity, phase stability as well as solubility heavily affect subsequent discharge and charge process of metal–air batteries (Figure 1.2d). Unique electrochemical behaviors of metal–air batteries have therefore been proposed depending on the combinations of metal and gas active species.[12-22]

Among several kinds of metal–air batteries, Li–O_2 battery, a most representative, has primarily received tremendous attention as it has the highest theoretical energy density (~3500 W h kg^{-1}) at level unattainable by conventional Li ion battery due to the use of light element of lithium and oxygen. Total reaction of Li–O_2 battery can be expressed as below.

$$2\mathrm{Li(s)} + \mathrm{O_2}(g) \rightarrow Li_2O_2(s), E_{th}^{\circ} = 2.96\ V\ (vs.\ Li/Li^+) \qquad (4)$$

Despite great attentions to rechargeable Li–O_2 battery, there are also several problems in currently developed Li–O_2 battery where unwanted side-reactions by reactive species take place during battery operation, which results in low energy efficiency and low cycle property. It has been revealed that highly reactive oxygen species (oxygen radicals or singlet oxygen *etc.*) generated during Li–O_2 battery operation attack all of the battery components including carbon cathodes and electrolytes, which results in degradation and failure of the battery.[23-27] Accordingly, many researchers have been focusing on suppressing the side-reactions by modifying carbon electrodes, developing robust electrolytes or applying catalysts to improve the electrochemical properties of Li–O_2 battery.[28-36] However, these approaches cannot reach ultimate solutions to overcome the intrinsic problems of reaction

chemistry of Li–O_2 system. For the breakthrough of intrinsic reaction problems of Li–O_2 battery, it is important to devise new chemistry based on metal and gas for high energy storing rechargeable battery system.

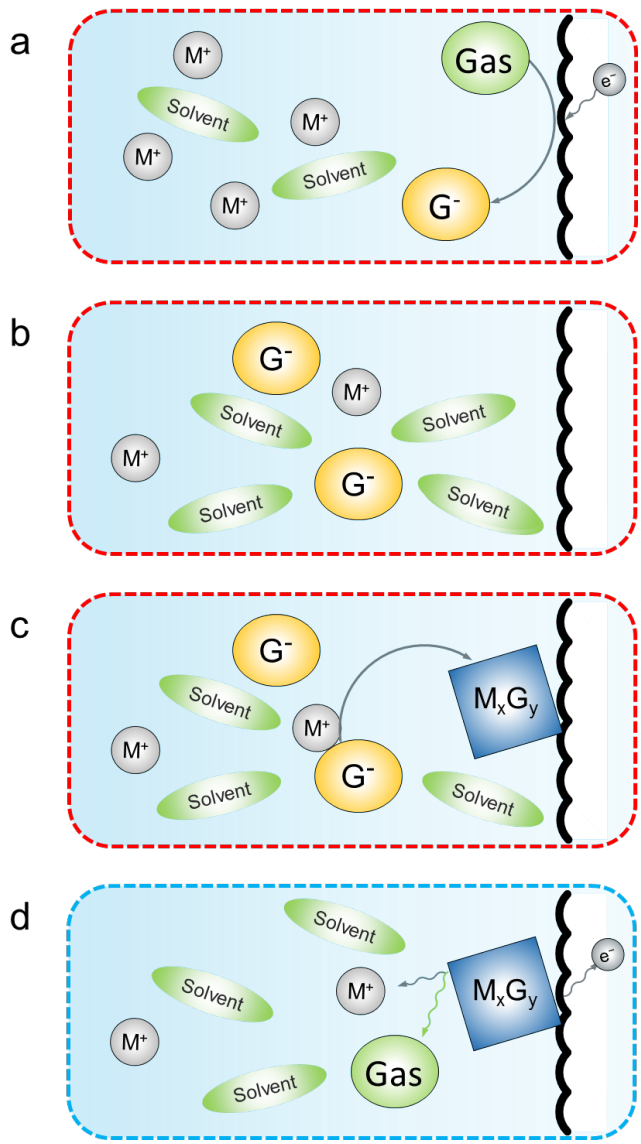

Figure 1.2. Schematic description of working principles for (a-c) discharge and (d) charge reaction of rechargeable metal–gas battery.

1.3 References

1 Tarascon, J. M. & Armand, M. Issues and challenges facing rechargeable lithium batteries. *Nature* **414**, 359-367 (2001).

2 Armand, M. & Tarascon, J. M. Building better batteries. *Nature* **451**, 652-657 (2008).

3 Choi, J. W. & Aurbach, D. Promise and reality of post-lithium-ion batteries with high energy densities. *Nature Reviews Materials* **1**, 16013 (2016).

4 Kang, K., Meng, Y. S., Bréger, J., Grey, C. P. & Ceder, G. Electrodes with High Power and High Capacity for Rechargeable Lithium Batteries. *Science* **311**, 977-980 (2006).

5 Bruce, P. G., Scrosati, B. & Tarascon, J. M. Nanomaterials for rechargeable lithium batteries. *Angewandte Chemie International Edition* **47**, 2930-2946 (2008).

6 Dunn, B., Kamath, H. & Tarascon, J.-M. Electrical Energy Storage for the Grid: A Battery of Choices. *Science* **334**, 928-935 (2011).

7 Arico, A. S., Bruce, P., Scrosati, B., Tarascon, J.-M. & van Schalkwijk, W. Nanostructured materials for advanced energy conversion and storage devices. *Nature Materials* **4**, 366-377 (2005).

8 Abraham, K. M. & Jiang, Z. A Polymer Electrolyte-Based Rechargeable Lithium/Oxygen Battery. *Journal of the Electrochemical Society* **143**, 1-5 (1996).

9 Aurbach, D., McCloskey, B. D., Nazar, L. F. & Bruce, P. G. Advances in understanding mechanisms underpinning lithium–air batteries. *Nature Energy* **1**, 16128 (2016).

10 Lim, H.-D. *et al.* Reaction chemistry in rechargeable Li-O_2 batteries. *Chemical Society Reviews* **46**, 2873-2888 (2017).

11 Ottakam Thotiyl, M. M. *et al.* A stable cathode for the aprotic Li–O_2 battery. *Nat Mater* **12**, 1050-1056 (2013).

12 Hartmann, P. *et al.* A rechargeable room-temperature sodium superoxide (NaO_2) battery. *Nature Materials* **12**, 228-232 (2013).

13 Ren, X. & Wu, Y. A Low-Overpotential Potassium–Oxygen Battery Based on Potassium Superoxide. *Journal of the American Chemical Society* **135**, 2923-2926 (2013).

14 Lim, H.-K. *et al.* Toward a Lithium–"Air" Battery: The Effect of CO_2 on the Chemistry of a Lithium–Oxygen Cell. *Journal of the American Chemical Society* **135**, 9733-9742 (2013).

15 Lim, H.-D. *et al.* A New Perspective on Li–SO_2 Batteries for Rechargeable Systems. *Angewandte Chemie International Edition* **54**, 9663-9667 (2015).

16 Hu, X., Dawut, G., Wang, J., Li, H. & Chen, J. Room-temperature rechargeable Na–SO_2 batteries containing a gel-polymer electrolyte. *Chemical Communications* **54**, 5315-5318 (2018).

17 Li, Y., Khurram, A. & Gallant, B. M. A High-Capacity Lithium–Gas Battery Based on Sulfur Fluoride Conversion. *The Journal of Physical*

Chemistry C **122**, 7128-7138 (2018).

18 He, M., Li, Y., Guo, R. & Gallant, B. M. Electrochemical Conversion of Nitrogen Trifluoride as a Gas-to-Solid Cathode in Li Batteries. *The Journal of Physical Chemistry Letters* **9**, 4700-4706 (2018).

19 Ma, J.-L., Bao, D., Shi, M.-M., Yan, J.-M. & Zhang, X.-B. Reversible Nitrogen Fixation Based on a Rechargeable Lithium-Nitrogen Battery for Energy Storage. *Chem* **2**, 525-532 (2017).

20 Yang, S. *et al.* A reversible lithium–CO_2 battery with Ru nanoparticles as a cathode catalyst. *Energy & Environmental Science* **10**, 972-978 (2017).

21 Shiga, T., Hase, Y., Kato, Y., Inoue, M. & Takechi, K. A rechargeable non-aqueous Mg–O_2 battery. *Chemical Communications* **49**, 9152-9154 (2013).

22 Reinsberg, P., Bondue, C. J. & Baltruschat, H. Calcium–Oxygen Batteries as a Promising Alternative to Sodium–Oxygen Batteries. *The Journal of Physical Chemistry C* **120**, 22179-22185 (2016).

23 Mahne, N. *et al.* Singlet oxygen generation as a major cause for parasitic reactions during cycling of aprotic lithium–oxygen batteries. *Nature Energy* **2**, 17036 (2017).

24 Wandt, J., Jakes, P., Granwehr, J., Gasteiger, H. A. & Eichel, R.-A. Singlet Oxygen Formation during the Charging Process of an Aprotic Lithium–Oxygen Battery. *Angewandte Chemie* **128**, 7006-7009 (2016).

25 McCloskey, B. *et al.* Twin problems of interfacial carbonate formation in

nonaqueous Li–O_2 batteries. *The Journal of Physical Chemistry Letters* **3**, 997-1001 (2012).

26 Ottakam Thotiyl, M. M., Freunberger, S. A., Peng, Z. & Bruce, P. G. The carbon electrode in nonaqueous Li–O_2 cells. *Journal of the American Chemical Society* **135**, 494-500 (2012).

27 Black, R. *et al.* Screening for superoxide reactivity in Li-O_2 batteries: effect on Li_2O_2/LiOH crystallization. *Journal of the American Chemical Society* **134**, 2902-2905 (2012).

28 Lim, H. D. *et al.* Enhanced Power and Rechargeability of a Li−O_2 Battery Based on a Hierarchical-Fibril CNT Electrode. *Advanced Materials* **25**, 1348-1352 (2013).

29 Ottakam Thotiyl, M. M. *et al.* A stable cathode for the aprotic Li–O_2 battery. *Nature Materials* **12**, 1050-1056 (2013).

30 Walker, W. *et al.* A rechargeable Li–O_2 battery using a lithium nitrate/N, N-dimethylacetamide electrolyte. *Journal of the American Chemical Society* **135**, 2076-2079 (2013).

31 Bae, Y. *et al.* Tuning the Carbon Crystallinity for Highly Stable Li–O_2 Batteries. *Chemistry of Materials* **28**, 8160-8169 (2016).

32 Gao, X., Chen, Y., Johnson, L. & Bruce, P. G. Promoting solution phase discharge in Li-O_2 batteries containing weakly solvating electrolyte solutions. *Nature Materials* **15**, 882-888 (2016).

33 Lim, H.-D. *et al.* Rational design of redox mediators for advanced Li–O_2

batteries. *Nature Energy* **1**, 16066 (2016).

34 Chen, Y., Freunberger, S. A., Peng, Z., Fontaine, O. & Bruce, P. G. Charging a Li–O_2 battery using a redox mediator. *Nature Chemistry* **5**, 489-494 (2013).

35 Lim, H.-D. *et al.* Superior Rechargeability and Efficiency of Lithium–Oxygen Batteries: Hierarchical Air Electrode Architecture Combined with a Soluble Catalyst. *Angewandte Chemie* **126**, 4007-4012 (2014).

36 Lim, H.-D. *et al.* A new catalyst-embedded hierarchical air electrode for high-performance Li–O_2 batteries. *Energy & Environmental Science* **6**, 3570-3575 (2013).

Chapter 2. Evolution of Li-SO_2 secondary battery

2.1 Revisiting Li-SO_2 primary batteries for rechargeable systems

(The essence of this chapter has been published in *Angewandte Chemie*. Reproduced with permission from [Lim, H.-D.† and Park, H.† *et al., Angew. Chem. Int. Ed.* **2015**, 54, 9663 –9667] Copyright (2015) WILEY-VCH)

2.1.1 Research Background

Primary Li-SO_2 batteries offer a high energy density in a wide operating temperature range with exceptionally long shelf life and have thus been frequently used in military and aerospace applications. Although these batteries have never been demonstrated as a rechargeable system, in this communication, we show that the reversible formation of $Li_2S_2O_4$, the major discharge product of Li-SO_2 battery, is possible with a remarkably smaller charging polarization than that of a Li-O_2 battery without the use of catalysts. The rechargeable Li-SO_2 battery can deliver approximately 5,400 mAh g^{-1} at 3.1 V, which is slightly higher than the performance of a Li-O_2 battery. In addition, the Li-SO_2 battery can be operated with the aid of a redox mediator, exhibiting an overall polarization of less than 0.3 V, which results in one of the highest energy efficiencies achieved for Li-gas battery systems.

Revisiting conventional primary batteries sometimes inspires new chemistry that can be adopted in rechargeable batteries. The recent rapid growth of the Li-O_2 battery field is an example of the successful evolution from a primary battery to a secondary battery.[1,2] Although it was previously conceived that a metal-O_2 system was only suitable for primary batteries, the current Li-O_2 system has become one of the most promising candidates for next-generation secondary batteries, specifically considering that it can deliver an exceptionally high energy density at a level unattainable by conventional lithium-ion batteries.[3-5] Exploring a new chemistry in metal-gas systems plays a key role in the development of ultra-high energy density batteries, as it enables electrochemical energy storage without the use of a heavy transition metal redox host. Recent reports on various metal-gas rechargeable batteries, such as Na-O_2, K-O_2, Al-O_2, and Li-CO_2 systems, reveal their potential applicability as high-energy-storage media with unique electrochemical properties depending on the combination of metal and gas.[6-12]

2.1.2 Experimental Method

2.1.2.1 Preparation of Li-SO_2 cells

The cathode was prepared from a mixture of Ketjen black (KB) and Kynar 2801 as a binder at a ratio of 8:2. The mixture was pasted onto a Ni-mesh current collector. The individual cells were assembled in the sequence of Li metal (3/8 inch diameter), glass fiber separator (Whatman GF/D microfiber filter paper, 2.7 μm pore size), and prepared KB electrode in a Swagelok-type cell. The cathode was open to sulfur dioxide gas. Before the test, all the cells were stabilized for 30 min. The electrolyte consisted of 1 M lithium bis(trifluoromethylsulfonyl)imide (LiTFSI) in tetraethylene glycol dimethylether (TEGDME). In the catalyst-loaded electrolyte, 0.05 M LiI was added to the solvent.

2.1.2.2 Electrochemical Characterization and Analyses

The electrochemical performances of Li-SO_2 cells were investigated using a potentio-galvanostat (WonA Tech, WBCS 3000, Korea). For the electrode characterization, X-ray diffractometry (XRD, Rigaku, D/MAX-RB diffractometer, Tokyo, Japan), X-ray photoelectron spectroscopy (XPS, Thermo VG Scientific, Sigma Probe, UK), and field-emission scanning electron microscopy (FE-SEM, Philips, XL 30 FEG, Eindhoven, Netherlands) were used. To measure the gas evolution *in-situ*, differential electrochemical mass spectroscopy (DEMS) was used. The DEMS system consisted of a mass spectrometer (MS) (HPR-20, Hiden Analytical) and a potentio-galvanostat (WonA Tech, WBCS 3000, Korea), as described in previous reports.[13,14] After the discharge process, the cell was transferred to the DEMS cell. Then, the DEMS cell was fully relaxed for 12 h with argon gas flowing (10 cc min^{-1}). The evolved gases were swept by argon gas to the MS chamber during the charge process.

2.1.3 Results and Discussions

The concept of a primary Li-SO_2 cell was first reported in the late 1960s.[15,16] It operates based on the reaction between lithium ions and sulfur dioxide, which produces $Li_2S_2O_4$ (lithium dithionite) as a discharge product, delivering an energy density of ~ 330 Wh kg^{-1}.[17-19] The sulfur dioxide is initially dissolved or liquefied in the electrolyte of a sealed cell with lithium metal as the anode and porous carbon as the cathode. Earlier Li-SO_2 systems needed to use a pressurized cell; however, recent works have successfully demonstrated that an ambient pressure cell is also achievable with the proper selection of an electrolyte that can dissolve a sufficiently large amount of sulfur dioxide.[18] Although the Li-SO_2 cell has never been demonstrated in rechargeable conditions with a gas inlet and outlet, the chemistry resembles that of the Li-O_2 system in many ways. During discharging, the gas phase receives electrons from the electrode surface, which subsequently combine with lithium ions to finally form lithium-containing solid discharge products. The porous electrode accommodates a large amount of solid products to achieve a high capacity and gradually fill the pores, which results in an increase in the impedance of the cell and finally the end of the discharge. Herein, we demonstrate that the charging reaction is also feasible in Li-SO_2 batteries, similar to Li-O_2, which can be reversibly operated using an organic electrolyte through the formation/decomposition of $Li_2S_2O_4$. The initial discharge capacity is as high as that of Li-O_2 batteries (~5,400 mAh g^{-1}); however, the energy efficiency is significantly better without the use of

catalysts. The working mechanism of rechargeable Li-SO_2 batteries can guide the development of a new metal-gas system and also aid in our understanding of the current limitation of the Li-O_2 system.

The working principle of a rechargeable Li-SO_2 battery is described in Figure 2.1a. Unlike the primary battery setup, the cell design consists of an electrode that is open to a SO_2 atmosphere using a Swagelok-type cell. During the discharge process, the porous carbon cathode enables an influx of SO_2 gas and provides reaction sites for the lithium ions and SO_2 to accommodate the discharge product, $Li_2S_2O_4$. During the charging process, the discharge products are expected to be decomposed and evolve SO_2 gas from the electrode. Figure 2.1b shows a typical discharge/charge profile of the Li-SO_2 battery along with that of the reference Li-O_2 battery under the same operation conditions. The discharge potential and profile are in a good agreement with those of the primary cell, indicating that the SO_2 reacted electrochemically with Li ions.[20,21] It is notable that the charging process is possible with overall electrochemical profiles similar to those of Li-O_2 cells. We observed that the charging process results in a significant amount of sulfur dioxide gas evolution, as demonstrated in Figure 2.1c. The *in-situ* DEMS experiment in Figure 2.1c detected the evolution of sulfur dioxide throughout the charging process without other gases such as carbon dioxide, oxygen, or hydrogen. The absence of other gases implies a stable charging reaction in the cell, in contrast to conventional Li-O_2 cells, which exhibit a detectable level of carbon monoxide or dioxide evolution resulting from the partial corrosion of the carbon electrode or decomposition of the

electrolyte.[22] The discharge capacity is comparable to that of a Li-O_2 cell; however, the voltage of the Li-SO_2 cell is higher by approximately 300 mV because the formation of the $Li_2S_2O_4$ discharge product yields a greater Gibbs free energy change in the reaction.[23] Note that the charging polarization of the Li-SO_2 cell is markedly lower than that of the Li-O_2 cell even without a catalyst. The completion of the charging process could be done below 4 V. Consequently, the observed energy efficiency of the Li-SO_2 system is significantly higher than that of the Li-O_2 system. In Figure 2.1d, we used the galvanostatic intermittent titration technique (GITT) to determine the thermodynamic potential of the reaction. After full relaxations, the quasi-open circuit potential of each step is close to the theoretical voltage of $Li_2S_2O_4$ formation, which also supports the conclusion that the discharge/charge reaction mainly involves the formation/decomposition of $Li_2S_2O_4$.

Using *ex-situ* analyses, we attempted to verify that the charging process was the result of the electrochemical decomposition of $Li_2S_2O_4$. Figure 2.2 presents *ex-situ* X-ray diffraction (XRD) patterns of the cathode in the Li-SO_2 battery at a few stages of discharge and charge. At each step, the cathode was carefully washed using the TEGDME solvent and dried before the test. All the procedures were performed in a glove box without air exposure. The results clearly demonstrate that the gradual formation and decomposition of $Li_2S_2O_4$ occur on the cathode. Upon discharge to step 1, the XRD peaks begin to evolve at 33.5° and 35.4°, which correspond to the characteristic peaks observed for $Li_2S_2O_4$. After further discharge, the peaks grow substantially with additional peaks appearing at 27.5° and 30.1°. However, the

intensities of these peaks decrease during charging and completely disappear at the end of the charge, suggesting that the decomposition of $Li_2S_2O_4$ primarily occurs during charging. The relatively sharp peaks of $Li_2S_2O_4$ appearing during a cycle are slightly different from those of the Li-O_2 cell, where the XRD signature of lithium peroxide (Li_2O_2) is sometimes difficult to detect.[24-27] This result hints at the relatively high crystallinity of the discharge product for the Li-SO_2 battery.

Consistent with the XRD results, the crystalline size of the discharge products was large after discharge, as observed in the SEM images in Figure 2.2. In the porous carbon electrode, the $Li_2S_2O_4$ gradually grows into a nano-ribbon-like morphology from discharge steps 1 to 3. The nano-ribbon shape of the discharge product with a length of a few micrometers and a width of hundreds of nanometers differs from the toroid or film-like morphology of Li_2O_2[28,29] in Li-O_2 cells or the cubic shape of NaO_2[8,30] in Na-O_2 cells. Because the morphology of the discharge products is closely related to the reaction mechanism involving the soluble intermediate discharge phase, a more detailed study will be required on this phenomenon.[31,32] Upon full discharge to 2.0 V, the nano-ribbon fills up nearly all of the void spaces of the carbon electrode (step 3). During the charging process, the discharge product gradually disappears; after step 5 (charge to ~3.8 V), most of the ribbon-like discharge products cannot be observed, and the pristine state of the carbon electrode is recovered. Additional SEM images of the cathode at lower magnification are presented in Figure 2.3.

The use of catalysts could further enhance the efficiency of the Li-SO_2 cell

by further reducing the charging polarization. As a model catalyst, a lithium iodide (LiI) soluble catalyst was adopted in the system, which was recently demonstrated to be an efficient redox mediator in the decomposition of Li_2O_2 in Li-O_2 batteries.[4,11,33] Figure 2.4a compares the electrochemical profiles of Li-SO_2 cells with (blue) and without (red) the catalyst. The addition of the catalyst led to a clear and significant decrease of the polarization during the charging process. The overall charge polarization was reduced to less than 0.3 V, which leads to a significant enhancement of the energy efficiency. Note that the oxidized form of LiI (I_2 or I_3^-) effectively decomposes $Li_2S_2O_4$ via a chemical reaction, similar to the reaction with Li_2O_2; however, it is more effective in the Li-SO_2 system because the equilibrium potential of $Li_2S_2O_4$ formation (~3.1 V) is closer to the redox potential of I^-/I^{3-} (or I^-/I_2) (~3.4 V) than that of Li_2O_2 formation (~2.96 V). Therefore, the theoretical charging efficiency using LiI in Li-SO_2 batteries can be as high as 91%, which is substantially higher than that in Li-O_2 batteries. The *ex-situ* XRD analysis (Figure 2.4b) demonstrates the reversible formation and decomposition of $Li_2S_2O_4$ within a much narrower voltage range (2.0–3.2 V) using the catalyst, which indicates that LiI could effectively decompose the discharge product. The catalytic activity of LiI in Li-SO_2 cells was also confirmed by *in-situ* DEMS analysis. The DEMS result in Figure 2.4c shows that sulfur dioxide (SO_2) was solely evolved during the charging process without any other gas evolution. Cycling of the cell using LiI was thus possible, and under a capacity-limited condition of 500 $mAhg^{-1}$, the cycling continued for more than 25 cycles, as demonstrated in Figure 2.4d.

The capacity retention was not remarkable at this stage, even though $Li_2S_2O_4$ could be electrochemically decomposed as demonstrated above. Less than 1,000 mAh g^{-1} could be retained after 10 cycles when operated without catalysts between 2.0–4.2 V, as shown in Figure 2.5. This performance level is only comparable to that of early Li-O_2 batteries.[34,35] To investigate the origin of the cycle degradation, we examined the cathode after the end of the cycling process using XRD, and the results are presented in Figure 2.6a. In addition to the main discharge product, $Li_2S_2O_4$, a trace of the Li_2SO_4 phase could also be detected, which was observed to cover the surface of the cathode by SEM (inset of Figure 2.6a). It implies that the rapid deterioration of the cell is most likely due to the residual byproducts on the surface of the cathode. For a closer investigation of the formation of byproducts on the surface, the surface was characterized by X-ray photoelectron spectroscopy (XPS), as shown in Figure 2.6b–c. After the first discharge, two major peaks dominated, corresponding to $Li_2S_2O_4$ and Li_2SO_3 in Figure 2.7 (S 2p XPS) with a trace of Li_2SO_4.[18] Although the peak of $Li_2S_2O_4$ disappears after charging, which again indicates the reversible decomposition of $Li_2S_2O_4$ during the charging process, the peaks from Li_2SO_3 and Li_2SO_4 do not completely disappear (Figure 2.6b). At the end of the cycling, residual amounts of Li_2SO_3 are still detected along with the unreacted $Li_2S_2O_4$. It is presumed that the byproducts remaining after charging are gradually deposited onto the carbon surface during cycling. This passivation layer may block the active pores while also contributing to the decrease in the electrical conductivity of the cathode. Suppression or elimination of the

byproducts will be key to further enhancing the cyclability.

Another practical barrier for the realization of a 'rechargeable Li-SO_2 battery' is the use of sulfur dioxide gas. Although sulfur dioxide is naturally released by volcanic activity and is widely used in winemaking as a preservative,[36] it is inherently a harmful gas. The emission of the gas into the atmosphere will not be desirable when charging the battery. As an alternative, in this respect, the rechargeable Li-SO_2 battery can be designed with a closed-cell type, where the circulation of the gas is confined within the cell. An interesting characteristic of SO_2 gas is that a substantially large amount of gas can be dissolved in the organic solvent, representing one of the highest solubilities among gases.[37] In addition, with slight pressurization, the soluble amount can be significantly increased, which explains why pressurized Li-SO_2 was one of the first systems to be commercialized in metal-gas batteries. Even without pressurization, it is noteworthy that the recent finding on ionic liquids as an electrolyte in primary Li-SO_2 could achieve a large amount of SO_2 gas dissolution at ambient pressure, resulting in a high energy density.[18] This finding implies that closed-type rechargeable Li-SO_2 batteries without the emission of harmful gases are feasible and that consideration of a smart cell design can make use of the high-energy rechargeable Li-SO_2 chemistry.

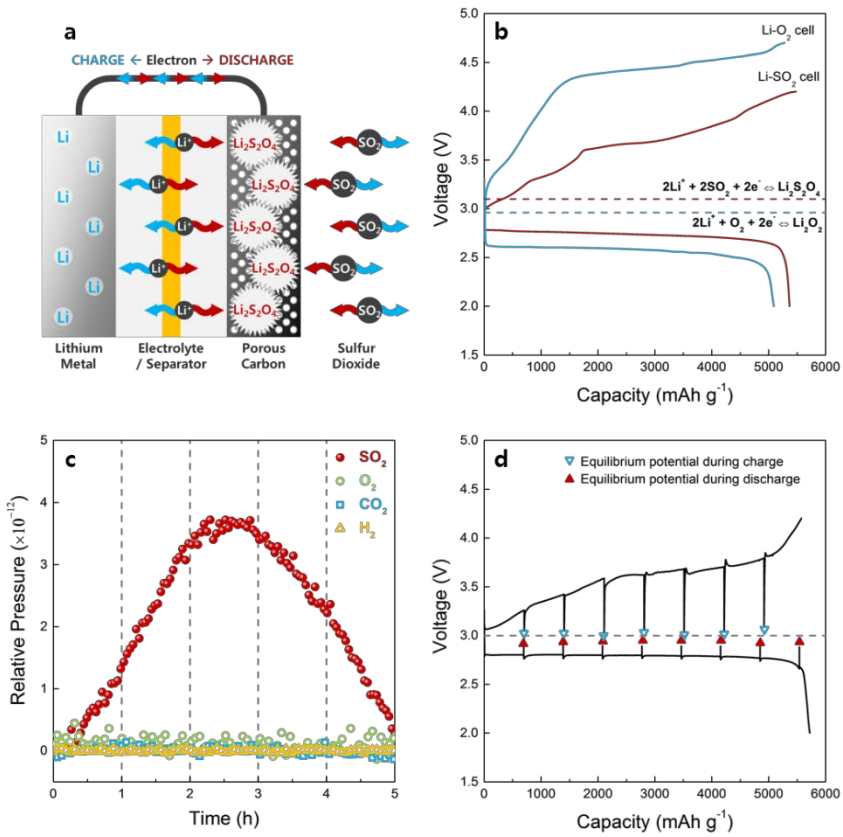

Figure 2.1. (a) Schematic illustration of the concept of a rechargeable Li-SO_2 battery during discharge and charge. (b) Comparison of the electrochemical profiles of Li-O_2 and Li-SO_2 batteries at a current density of 0.2 mA cm^{-2}. The theoretical formation potentials of Li_2O_2 and $Li_2S_2O_4$ are 2.96 and 3.1 V *vs.* Li/Li^+, respectively. (c) Gas evolution profile during charge process of Li-SO_2 cell with limited capacity of 1 mAh obtained using *in-situ* DEMS analysis. (d) Galvanostatic intermittent titration technique (GITT) voltage profile of Li-SO_2 cell. The discharge capacities were calculated based on the cathode carbon weight.

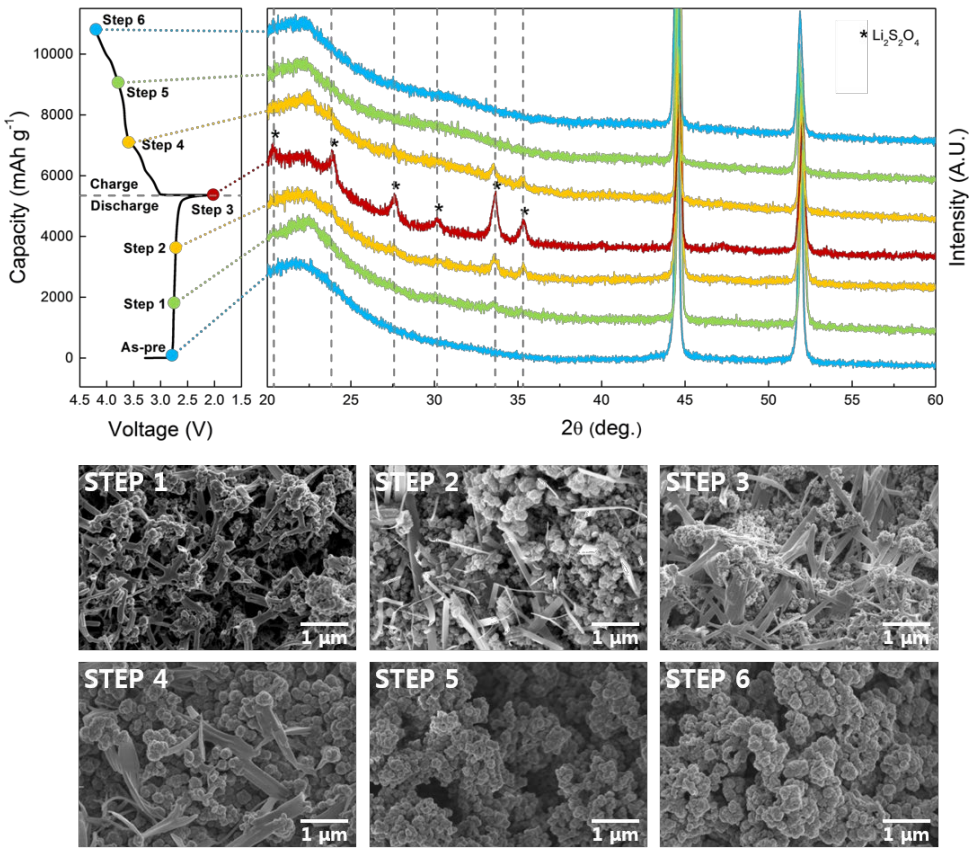

Figure 2.2. *Ex-situ* XRD and SEM analysis of a Li-SO_2 battery at each step. The dotted lines correspond to $Li_2S_2O_4$, and the high intensity peaks near 44° and 52° correspond to the Ni mesh current collector. All of the figures were viewed under the same magnification.

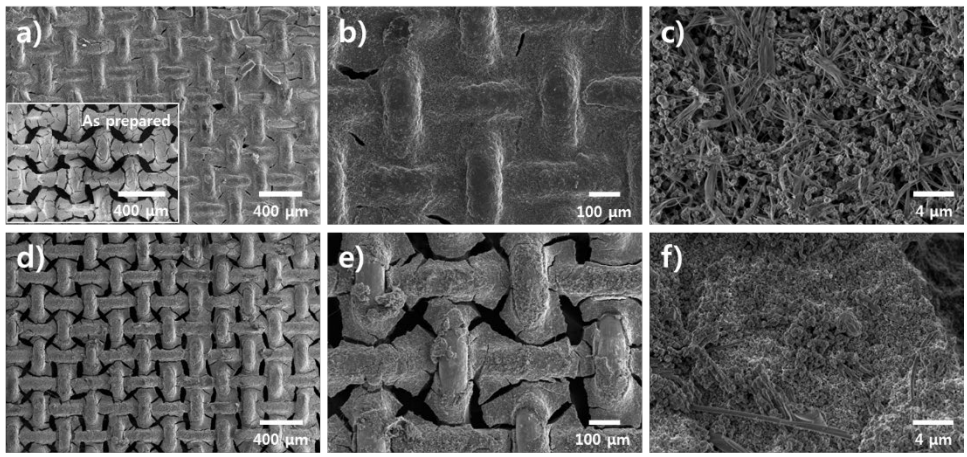

Figure 2.3. SEM images of cathode at low magnification (a-c) after the first discharge and (d-f) after re-charge (inset: SEM image of the as-prepared cathode).

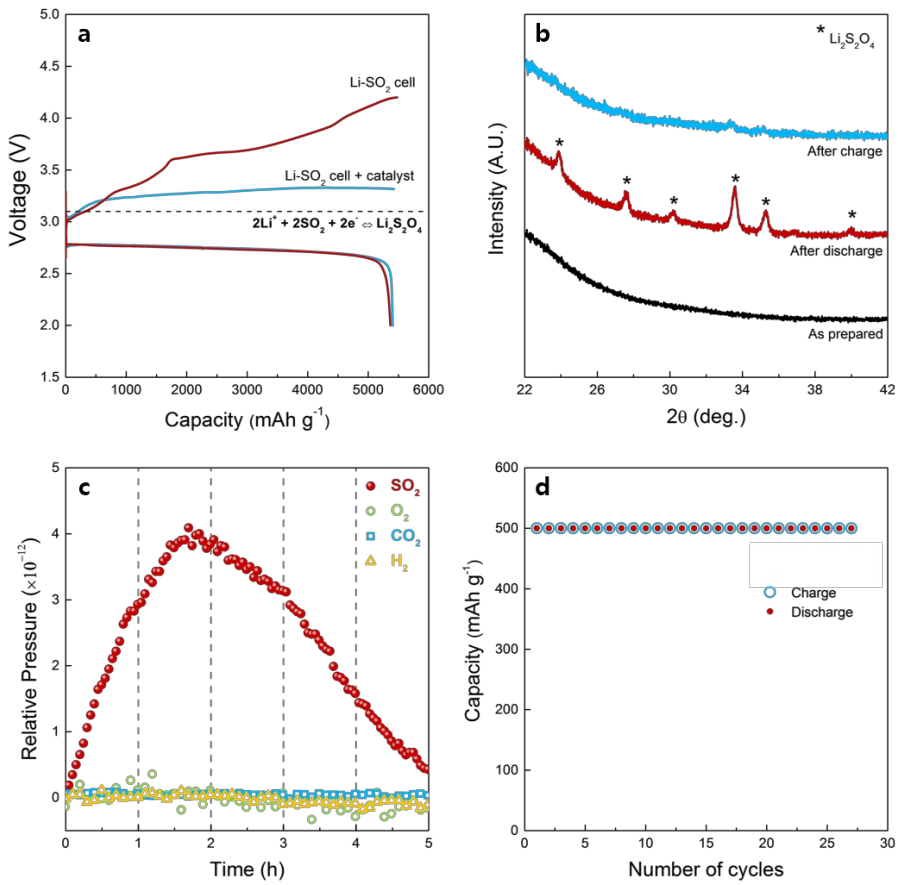

Figure 2.4. (a) Comparison of the electrochemical profiles of the Li-SO_2 cell without and with a catalyst. (b) XRD results of the Li-SO_2 cell using a catalyst. (c) *In-situ* DEMS result; gas evolution as a function of time during the charge process of the Li-SO_2 cell with LiI catalyst. (d) Cyclability of the Li-SO_2 cell with the catalyst utilized up to 500 mAh g^{-1}.

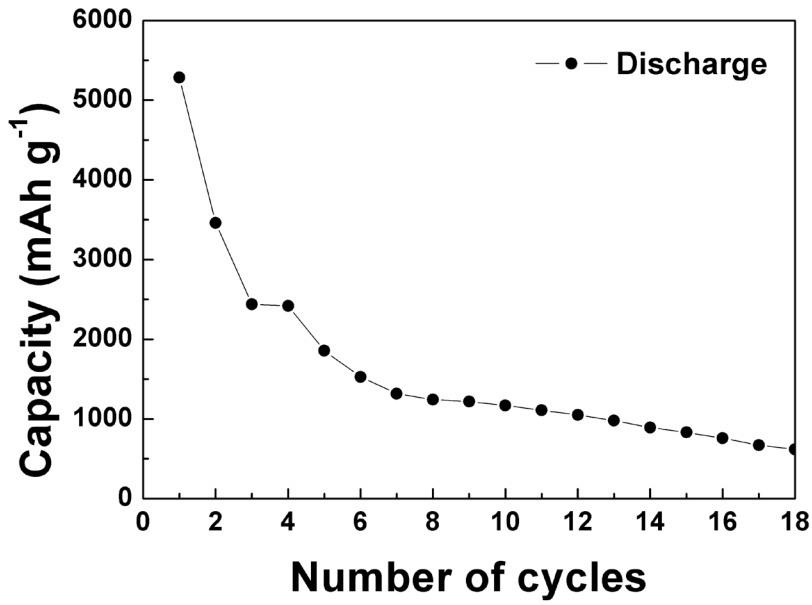

Figure 2.5. The cyclability of a Li-SO_2 battery at a constant current rate of 0.2 mA/cm^2 between 2.0–4.2 V.

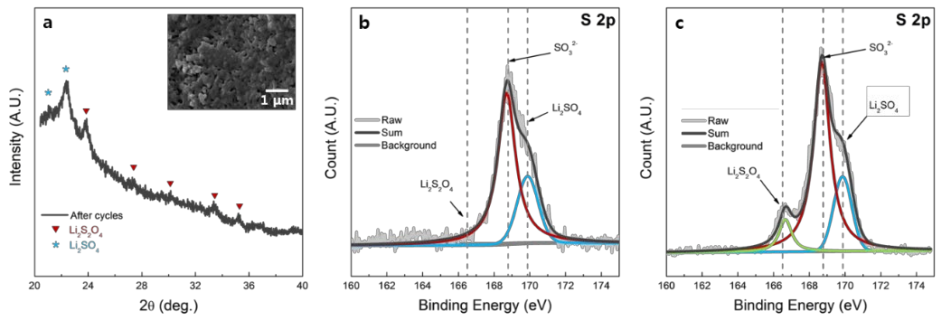

Figure 2.6. (a) XRD pattern of the cathode after cycling (inset: SEM image of the cathode after cycling). XPS spectra of S 2p: (b) after re-charge, and (c) at the end of cycling. The overall peaks are arranged based on the reference C-C bond at 284.5 eV.

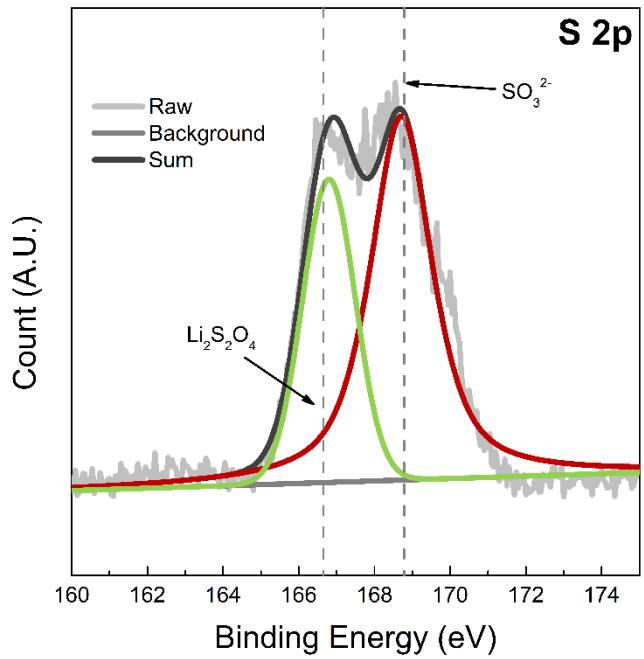

Figure 2.7. XPS spectra of S 2p after the first discharge.

2.1.4 Concluding Remarks

In summary, a rechargeable Li-SO_2 battery was demonstrated for the first time. The electrochemical formation and decomposition of $Li_2S_2O_4$, the major discharge product of a Li-SO_2 battery, was reversibly possible with a remarkably small charging polarization even without a catalyst. With the aid of a LiI redox mediator, it could exhibit a polarization lower than 0.3 V with one of the highest energy efficiencies achieved for Li-gas battery systems to date. The rechargeable Li-SO_2 battery could deliver approximately 5,400 mAh g^{-1} at 3.1 V, which is slightly higher than that of the Li-O_2 battery. However, at this stage, the level of cycle performance is limited because of the formation of byproducts, which gradually deposit on the cathode and hinder the efficient cycling. Although a step forward has been made for the secondary Li-SO_2 battery system, issues such as suppression of the byproducts to enhance the cyclability and the identification of an electrolyte capable of dissolving a large amount of SO_2 gas to minimize the emission remain to be resolved. This report may provide an interesting new direction for designing rechargeable battery systems by applying a conventional primary battery chemistry to a viable secondary battery system.

2.1.5 References

1 Abraham, K. M. & Jiang, Z. A Polymer Electrolyte-Based Rechargeable Lithium/Oxygen Battery. *Journal of The Electrochemical Society* **143**, 1-5 (1996).

2 Bruce, P. G., Freunberger, S. A., Hardwick, L. J. & Tarascon, J.-M. Li-O_2 and Li-S batteries with high energy storage. *Nat Mater* **11**, 19-29 (2012).

3 Débart, A., Paterson, A. J., Bao, J. & Bruce, P. G. α-MnO_2 Nanowires: A Catalyst for the O_2 Electrode in Rechargeable Lithium Batteries. *Angewandte Chemie* **120**, 4597-4600 (2008).

4 Lim, H.-D. *et al.* Superior Rechargeability and Efficiency of Lithium–Oxygen Batteries: Hierarchical Air Electrode Architecture Combined with a Soluble Catalyst. *Angewandte Chemie International Edition* **53**, 3926-3931 (2014).

5 Peng, Z., Freunberger, S. A., Chen, Y. & Bruce, P. G. A Reversible and Higher-Rate Li-O_2 Battery. *Science* **337**, 563-566 (2012).

6 Mori, R. A novel aluminium-air secondary battery with long-term stability. *RSC Advances* **4**, 1982-1987 (2014).

7 Ren, X. & Wu, Y. A Low-Overpotential Potassium–Oxygen Battery Based on Potassium Superoxide. *Journal of the American Chemical Society* **135**, 2923-2926 (2013).

8 Hartmann, P. *et al.* A rechargeable room-temperature sodium superoxide (NaO_2) battery. *Nat Mater* **12**, 228-232 (2013).

9 Gowda, S. R., Brunet, A., Wallraff, G. M. & McCloskey, B. D. Implications of CO_2 Contamination in Rechargeable Nonaqueous Li–O_2 Batteries. *Journal of Physical Chemistry Letters* **4**, 276-279 (2013).

10 Takechi, K., Shiga, T. & Asaoka, T. A Li-O_2/CO_2 battery. *Chemical Communications* **47**, 3463-3465 (2011).

11 Shiga, T., Hase, Y., Kato, Y., Inoue, M. & Takechi, K. A rechargeable non-aqueous Mg-O_2 battery. *Chemical Communications* **49**, 9152-9154 (2013).

12 Liu, Y., Wang, R., Lyu, Y., Li, H. & Chen, L. Rechargeable Li/CO_2-O_2 (2 : 1) battery and Li/CO_2 battery. *Energy & Environmental Science* **7**, 677-681 (2014).

13 Lim, H.-D. *et al.* Mechanism of Co_3O_4/graphene catalytic activity in Li–O_2 batteries using carbonate based electrolytes. *Electrochimica Acta* **90**, 63-70 (2013).

14 Adams, B. D. *et al.* The Importance of Nanometric Passivating Films on Cathodes for Li–Air Batteries. *ACS Nano* **8**, 12483-12493 (2014).

15 W. F. Meyers, B. B. a. J. W. S. *U.S. Patent* **3 423 242** (1969).

16 Fey, G. T. K. Li/SO_2 rechargeable batteries. *Journal of Power Sources* **35**, 153-162 (1991).

17 Ake, R. L., Oglesby, D. M. & Kilroy, W. P. A Spectroscopic Investigation of Lithium Dithionite and the Discharge Products of a Li / SO_2 Cell. *Journal of The Electrochemical Society* **131**, 968-974 (1984).

18 Xing, H. *et al.* Ambient Lithium–SO_2 Batteries with Ionic Liquids as Electrolytes. *Angewandte Chemie International Edition* **53**, 2099-2103 (2014).

19 Rupich, M. W., Pitts, L. & Abraham, K. M. Characterization of Reactions and Products of the Discharge and Forced Overdischarge of Li / SO_2 Cells. *Journal of The Electrochemical Society* **129**, 1857-1861 (1982).

20 Ratnakumar, B. V. *et al.* Potentiostatic Depassivation of Lithium-Sulfur Dioxide Batteries on Mars Exploration Rovers. *Journal of The Electrochemical Society* **154**, A715-A724 (2007).

21 Linden, D. & McDonald, B. The lithium—sulfur dioxide primary battery — its characteristics, performance and applications. *Journal of Power Sources* **5**, 35-55 (1980).

22 Ottakam Thotiyl, M. M., Freunberger, S. A., Peng, Z. & Bruce, P. G. The Carbon Electrode in Nonaqueous Li–O_2 Cells. *Journal of the American Chemical Society* **135**, 494-500 (2012).

23 Huggins, R. A. *Advanced batteries: materials science aspects, Springer Science* **New York**, pp. 159-195 (2008).

24 Zhai, D. *et al.* Raman Evidence for Late Stage Disproportionation in a Li–O_2 Battery. *Journal of Physical Chemistry Letters* **5**, 2705-2710 (2014).

25 Oh, D. *et al.* Biologically enhanced cathode design for improved capacity and cycle life for lithium-oxygen batteries. *Nature Communications* **4**, 2756 (2013).

26 Hassoun, J. *et al.* A Metal-Free, Lithium-Ion Oxygen Battery: A Step Forward to Safety in Lithium-Air Batteries. *Nano Letters* **12**, 5775-5779 (2012).

27 Shang, C. *et al.* Compatible interface design of CoO-based Li-O_2 battery cathodes with long-cycling stability. *Scientific Reports* **5**, 8335 (2015).

28 Ganapathy, S. *et al.* Nature of Li_2O_2 Oxidation in a Li–O_2 Battery Revealed by Operando X-ray Diffraction. *Journal of the American Chemical Society* **136**, 16335-16344 (2014).

29 Adams, B. D. *et al.* Current density dependence of peroxide formation in the Li-O_2 battery and its effect on charge. *Energy & Environmental Science* **6**, 1772-1778 (2013).

30 Hartmann, P. *et al.* A comprehensive study on the cell chemistry of the sodium superoxide (NaO_2) battery. *Physical Chemistry Chemical Physics* **15**, 11661-11672 (2013).

31 Johnson, L. *et al.* The role of LiO_2 solubility in O_2 reduction in aprotic solvents and its consequences for Li–O_2 batteries. *Nature Chemistry* **6**, 1091-1099 (2014).

32 Aetukuri, N. B. *et al.* Solvating additives drive solution-mediated electrochemistry and enhance toroid growth in non-aqueous Li–O_2 batteries. *Nature Chemistry* **7**, 50-56 (2015).

33 Yu, M., Ren, X., Ma, L. & Wu, Y. Integrating a redox-coupled dye-sensitized photoelectrode into a lithium–oxygen battery for photoassisted

charging. *Nature Communications* **5**, 5111 (2014).

34 Freunberger, S. A. *et al.* Reactions in the Rechargeable Lithium–O_2 Battery with Alkyl Carbonate Electrolytes. *Journal of the American Chemical Society* **133**, 8040-8047 (2011).

35 Lim, H.-D. *et al.* The potential for long-term operation of a lithium-oxygen battery using a non-carbonate-based electrolyte. *Chemical Communications* **48**, 8374-8376 (2012).

36 Compton, B. W. *Sulfur Dioxide: Properties, Applications and Hazards, Nova Science Publishers* **New York** (2011).

37 Gerrard, P. G. T. F. a. W. *Solubility of gases in liquids : a critical evaluation of gas/liquid systems in theory and practice, J. Wiley* **New York** (1991).

2.2 High-efficiency and high-power rechargeable Li–SO_2 batteries exploiting conventional carbonate-based electrolytes

2.2.1 Research Background

To satisfy the growing demand on energy storage devices for emerging electric vehicles and grid-scale energy storage markets, recent efforts have been devoted to exploring a new battery chemistry that can outperform the current state-of-the-art lithium-ion batteries (LIBs).[1-3] Revisiting the conventional primary batteries can offer insight for developing a novel rechargeable chemistry by taking advantage of the recent advances in the fundamental understanding of battery science.[4-6] One recent example is the development of rechargeable lithium–sulfur dioxide (Li–SO_2) batteries. The primary lithium–sulfur dioxide battery offers a high energy density in a wide operating temperature range with exceptionally long shelf life and has thus been commercialized for military and aerospace applications since it was developed in the late 1960s.[7-10]. Recently, the lithium–sulfur dioxide chemistry was newly revisited and proposed as a promising rechargeable battery chemistry.[11,12] Under an analogous cell configuration adopted from lithium–oxygen batteries, it was demonstrated that a

reversible electrochemical reaction between lithium and sulfur dioxide is possible with the formation and decomposition of lithium dithionite ($Li_2S_2O_4$). Similar to lithium–oxygen and lithium–sulfur batteries[6], the absence of heavy transition metals in the redox reaction can result in a high energy density reaching 1,132 Wh/kg based on the mass of $Li_2S_2O_4$. Moreover, the intrinsically smaller polarization and higher gas efficiency were observed to be advantageous compared with lithium–oxygen systems, making the lithium–sulfur dioxide battery a new potential metal–gas rechargeable battery chemistry.

Recent studies have revealed that the properties of the electrolyte in metal–gas batteries play a pivotal role in determining the nature of discharge products and the rechargeability of the system.[13-19] The discharge mechanisms and nature of discharge products such as their morphology and stability can be significantly altered by the properties of the electrolyte, such as donor numbers or dielectric constants.[20-25] The critical dependency on the electrolyte in the metal–gas system compared with conventional lithium/sodium-ion batteries is most likely due to the generation of gas radicals, which are an important intermediate for the discharge reaction. Depending on the stability of the electrolyte, the gas radicals can react with the electrolyte solvent rather than the desirable alkali ions, such as lithium or sodium, which can form rechargeable discharge products.[15,26,27] Moreover, the stability of the intermediate alkali–radical complex is governed by the nature of the electrolyte and can thus alter the discharge paths.[21-23] In the early development of rechargeable lithium–oxygen or sodium–oxygen batteries, the use of carbonate-

based electrolytes yielded side reaction products; thus, an appropriate charging process could not be achieved.[14,15,19] The organic carbonate was highly vulnerable to chemical attacks by the oxygen radicals generated during the discharge process.[14,15,26,28] This finding led to the overall perception that carbonate-based electrolytes cannot be considered for metal–air batteries. Nevertheless, carbonate-based electrolytes possess several benefits, including high ionic conductivity and wide electrochemical windows, which have made them a common electrolyte for the well-developed LIB technology.[29,30] Moreover, the good lithium metal compatibility and chemical stability can be potential merits for lithium–air battery systems, which are expected to use lithium metal anodes and operate in an open system.

In this work, we evaluate the feasibility of implementing a conventional carbonate-based electrolyte in a lithium–sulfur dioxide battery and investigate how the electrochemical properties are affected. Although the stability of sulfur dioxide gas radicals during the discharge process is unknown, we observe that the chemical reactivity of SO_2^- toward organic carbonates is both thermodynamically and kinetically prohibited according to density functional theory (DFT) calculations. It is also experimentally verified that a lithium–sulfur dioxide battery employing ethylene carbonate (EC) and dimethyl carbonate (DMC) as electrolytes can reversibly operate with the formation and decomposition of a $Li_2S_2O_4$ discharge product. Furthermore, it is revealed that the power capability and cycling properties of the lithium–sulfur dioxide batteries are remarkably

improved compared with those using an ether-based electrolyte because of its higher ionic conductivity and better compatibility with the lithium metal anode. By introducing a soluble catalyst, cycling over 450 cycles is demonstrated with a high energy efficiency, exhibiting an overall polarization of 0.2 V during cycling, which has not yet been achieved in either lithium–oxygen or lithium–sulfur dioxide batteries. This report is the first to demonstrate that conventional carbonate-based electrolytes can be successfully applied in rechargeable metal–gas systems, opening up a new avenue toward high-efficiency rechargeable metal–gas batteries.

2.2.2 Experimental Method

2.2.2.1 Computational details

DFT calculations were performed using the Jaguar 8.9 software[31] for molecular reaction energies under the PB implicit solvation condition. We used the exchange-correlation functional of B3LYP[32,33] along with the Pople 6-311++G** basis set[34]. The ground electronic and geometric structures for molecular reaction intermediates were fully optimized for both gas and solution phases. Single-point solution-phase calculations without relaxing the gas phase structure were conducted only for the transition state obtained from a simple quasi-Newton method that searches for the transition state nearest to the input guessed geometry. The initial guess for the transition state search was obtained by scanning the most unstable geometry along the expected reaction coordinates, and the obtained transition states were validated by checking the number of imaginary frequency from vibrational modes. We also used the Vienna Ab initio Simulation Package (VASP)[35] for the calculations of the cohesive energy of crystal structures with the exchange-correlation function of Perdew–Burke–Ernzerhof (PBE)[36]. The electron–ion interaction was considered in the form of the projector augmented wave (PAW) method with a plane wave up to an energy of 400 eV. Gamma-centered k-point grids of 10 × 10 × 10 for lithium metal, 5 × 5 × 5 for $Li_2S_2O_4$, and 4 × 6 × 4 for Li_2SO_4 were generated. The ground electronic and geometric structures were fully optimized for the crystal and corresponding formula unit molecule for each crystal structure.

Further details including solvent parameters and hypothetical crystal structure are discussed in Table 2.1 and Figure 2.8, respectively.

Table 2.1. Parameters for Poisson–Boltzmann implicit solvation calculation. The dielectric constant (ε) and probe radii (R) for the electrolyte solvents were determined based on experimental literature values.

Solvent	Dielectric constant, ε	Molar mass, Mw (g/mol)	Density, ρ (g/cc)	Probe radius, R (Å)
Ethylene carbonate (EC)	95.3	88.06	1.32	2.36
Dimethyl carbonate (DMC)	3.1	90.08	1.07	2.56
EC/DMC (1:1 vol%)	35.0	88.95	1.20	2.45
Tetraethylene glycol dimethyl ether (TEGDME)	7.8	222.28	1.01	3.52

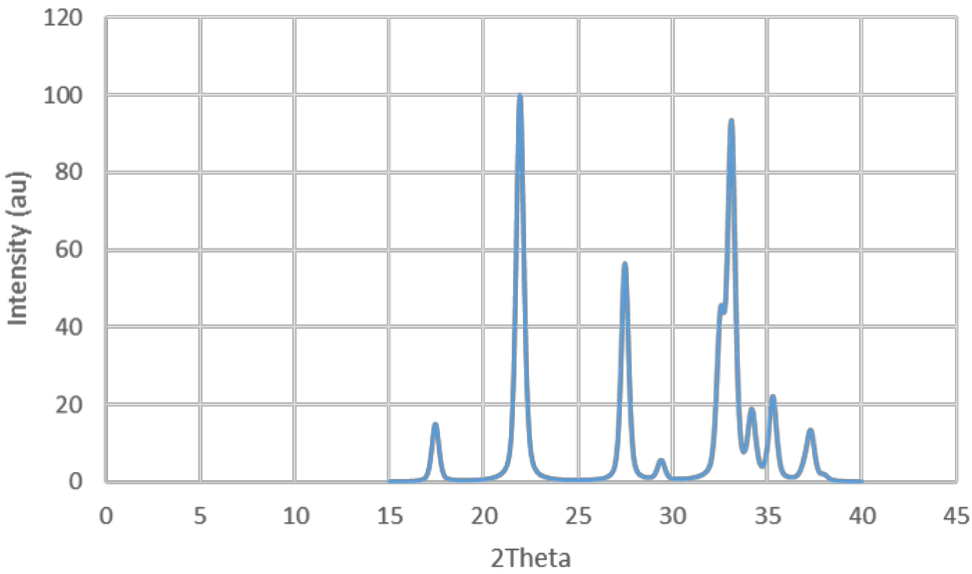

Figure 2.8. Simulated XRD pattern of theoretically optimized $Li_2S_2O_4$ crystal structure based on $Na_2S_2O_4$. The crystal structure for $Li_2S_2O_4$ was hypothetically generated by substituting Na atoms with Li atoms based on the $Na_2S_2O_4$ structure because there is no experimentally determined crystal structure (only available powder diffraction peak data, JCPDS #36-1101). The simulated XRD pattern indicates that the hypothetical $Li_2S_2O_4$ crystal structure was reasonably selected.

2.2.2.2 Preparation and assembly of Li–SO_2 cells

For the preparation of carbon paste, Ketjen black carbon (EC 600JD, Ilshin Chemtech) was dispersed with polytetrafluoroethylene (PTFE, 60 wt% dispersion in H_2O) binder in a mass ratio of 8:2 into a solution of isopropanol (IPA, >99.7%, Sigma-Aldrich) and N-methyl-2-pyrrolidone (NMP, 99.5%, anhydrous, Sigma-Aldrich) with a volume ratio of 1:1. The carbon gas-electrode was fabricated by casting the carbon paste on the carbon paper current collectors (TGP-H030, Toray, Japan) and dried overnight at 120°C to evaporate the solvent and residual water. The average loading mass of the Ketjen black electrodes in a 1/2-inch diameter was approximately 0.8 ± 0.1 mg. Electrolytes of 1 M lithium hexafluorophosphate ($LiPF_6$) dissolved in EC/DMC 1:1 vol% or TEGDME with water contents less than 20 ppm measured by Karl–Fisher titration were used. The lithium–sulfur dioxide cell was assembled using a Swagelok-type cell in a sequence of lithium metal (3/8-inch diameter), two sheets of Celgard 2400 separators (1/2-inch diameter), and the prepared carbon electrode (1/2-inch diameter) in an Ar-filled glove box (O_2 level < 1 ppm and H_2O level < 1 ppm). The amount of electrolyte was 200 μL. For the electrolytes employing the soluble catalyst, 50 mM concentration of DMPZ was added to the prepared electrolytes. The gas-electrode of individual cells was open to the sulfur dioxide gas after the cell assembly and stabilized during a relaxation time of 0.5 h before the cell tests.

2.2.2.3 Characterization of Li–SO_2 cells

All the electrochemical tests for the lithium–sulfur dioxide cells were performed using a potentio-galvanostat (WBCS 3000, WonA Tech, Korea) between 2.0 and 4.2 V at room temperature. For the lithium symmetric cell tests, a coin-type cell CR2032 was assembled with ½-inch diameter lithium foils as both the counter and working electrode and a slice of Celgard 2400 separator soaked with electrolytes. The electrolytes used for the lithium/lithium symmetric test were saturated with sulfur dioxide gas by bubbling in prepared electrolytes. Electrochemical impedance measurements were performed by using a potentio-galvanostat (VSP-300, Bio-Logic Science Instruments, France) at room temperature with a frequency range from 200 kHz to 50 mHz. A Bruker D2-Phaser with Cu-Kα radiation (λ=1.5406 Å) was used to obtain XRD spectra of the cathodes under an Ar atmosphere with an air-locking holder. The morphology of the products in the electrode was examined using FE-SEM (MERLIN Compact, ZEISS, Germany) after Pt coating. XPS (Thermo VG Scientific, Sigma Probe, UK) was used for the surface characterization of the cathodes in an Ar atmosphere without air exposure. For the *in situ* gas analyses, a DEMS instrument constructed with the combination of a mass spectrometer (MS; HPR-20, Hiden Analytical) and potentio-galvanostat was used, as described in our previous report.[37] *In situ* gas analyses were conducted using argon carrier gas at a constant flow rate of 10 cc/min during the charge process after the full relaxation of the DEMS cell. Dielectric constants of prepared solutions were measured at 20 °C

by using Liquid Dielectric Constant Meter (Model 871, Nihon Rufuto, Japan). UV-vis spectroscopy (Cary 5000, Agilent, United States) was used for sulfur dioxide solution characterizations.

2.2.3 Results and Discussions

2.2.3.1 Theoretical investigation of Li–SO_2 chemistry

The basic principle of lithium–sulfur dioxide battery operation is based on the simple electrochemical reaction between lithium and sulfur dioxide gas, whose general discharge reaction is[38,39]:

Anode: $Li\ (s) \rightarrow Li^+ + e^-$ (1)

Cathode: $2SO_2\ (g) + 2e^- \rightarrow S_2O_4^{2-}$ (2)

Total: $2Li\ (s) + 2SO_2\ (g) \rightarrow Li_2S_2O_4\ (s)$ (3)

$E^o = 3.0\ V\ (vs.\ Li/Li^+)$

In the cathode reaction, the sulfur dioxide collects the electron from the electrode and forms the intermediate dithionite ion ($S_2O_4^{2-}$) before precipitating as solid $Li_2S_2O_4$, the final discharge product. However, recent findings on O_2^- in the lithium–oxygen chemistry suggest that the intermediate $S_2O_4^{2-}$ may undergo chemical interactions with surrounding electrolyte molecules, which may lead to alternation in the discharge reaction path.[21,22] To investigate this early stage of the discharge reaction, we used DFT calculations coupled with the Poisson–Boltzmann (PB) solvation model to explore the reaction thermodynamics of lithium–sulfur dioxide batteries. Moreover, similar calculations were performed under different electrolyte conditions to probe the effect of the surrounding electrolyte molecules on this discharge reaction. We selected two types of electrolyte: a conventional carbonate-based electrolyte (EC/DMC, 1:1 volume mixture) and ether-based electrolyte

(tetraethylene glycol dimethyl ether, TEGDME), both of which have been widely used for lithium-ion and lithium–air rechargeable batteries.[40-43] Figure 2.9a shows the energy of the first electron transfer step starting from the sulfur dioxide molecule in a gas phase to SO_2^- in the respective electrolyte solution. A slightly different energy trajectory of the electron transfer was observed in the two electrolyte systems, where the SO_2^- in the EC/DMC is more stable by 0.30 eV than that in the TEGDME. The slightly different stabilization of the charged species is mainly attributed to the strong solvating ability of the carbonate-based electrolyte with the high dielectric constant ($\varepsilon \sim 35$).[20,44]

Under normal operation conditions, it is expected that the electrochemically reduced SO_2^- would react with lithium ions, leading to the formation of solid discharge products. However, the SO_2^- in lithium–sulfur dioxide cells may also undergo a chemical reaction with the carbonate-based electrolyte by nucleophilic attack, *i.e.,* electrolyte decomposition similar to the behavior of O_2^- in the electrolytes of lithium–oxygen batteries[13,26]. The plausibility of this chemical reaction can be determined by assessing the energetics of the initial complex formation (ICF) process involving the electrolyte molecule and SO_2^-.[20,26,27] Figure 2.9b presents the energy profile for the ICF processes involving EC molecules with the nucleophilic attack of SO_2^- compared with that of the previously known case of O_2^-. Consistent with earlier theoretical[20,26] and experimental studies[14], the ICF of EC–O_2 (blue dotted line) is a energetically downhill process with a moderate activation barrier, which indicates the instability of the carbonate electrolyte upon exposure to O_2^-. However, it is noted that the ICF of EC–SO_2 (red dotted line) is

energetically unfavorable by 0.24 eV. Moreover, the activation energy that needs to be overcome is as high as 1.08 eV, indicating that it is also kinetically hindered. This finding implies that the electrochemically driven SO_2^- molecule is likely to be stable in contact with the carbonate-based electrolyte without triggering severe degradation of the electrolyte.

The initial discharge process was investigated in further detail by evaluating the energies of each elementary reaction step from the SO_2^- molecule to the final $Li_2S_2O_4$ product; however, the detailed electrochemical mechanism of lithium–sulfur dioxide batteries remains poorly understood to date. Figure 2.9c illustrates the most favorable discharge paths with each step denoted with energies in TEGDME (blue line) and EC/DMC (red line) electrolytes using the PB solvation model, where only the dielectric constant of the specific solvent is considered. Note that the dielectric constant of organic electrolytes can slightly alter with the addition of sulfur dioxide into the solvents as shown in Figure 2.10 and the measured dielectric constant of organic solutions dissolving sulfur dioxide was used for theoretical calculations in this study. Moreover, it should be noted that the energy profiles of elementary cathode reactions in Figure 2.9c are described without consideration of the energetics of the anode reaction and the total reaction energetics including the anodic part are summarized in Table 2.2. For TEGDME, which has a low dielectric constant (weak electrostatic interaction), the initial process proceeds with SO_2^- combining with lithium ions, forming the neutral intermediate species of $LiSO_2$. The additional chemical association of SO_2^- and lithium ions to

$LiSO_2$ results in the formation of the final product of $Li_2S_2O_4$ during the continuous downhill energy process. In contrast, for EC/DMC with a relatively high dielectric environment (strong electrostatic interaction), SO_2^- is prone to undergo a dimerization reaction, forming $S_2O_4^{2-}$ rather than a neutral species with lithium ions, which is a well-known chemical equilibrium of $2SO_2^- \leftrightarrow S_2O_4^{2-}$ in organic chemistry and biochemistry.[45-47] In the subsequent reaction steps, two lithium ions are associated with $S_2O_4^{2-}$, forming $LiS_2O_4^-$ and $Li_2S_2O_4$, undergoing substantial uphill energy processes before the precipitation of the final product. The notably different initial discharge steps in the two electrolytes is attributed to their distinct solvating characters, where the high-dielectric solvent (EC/DMC) stabilizes the charged species such as $S_2O_4^{2-}$ more effectively, preserving the strong solvation shell, and the low-dielectric solvent (TEGDME) fails to stabilize them, thus preferring to form a neutral species ($LiSO_2$) in the reaction. This theoretical tendency is in accordance with the previous experimental findings that the chemical equilibrium constant of dimerization reaction to dithionite ion has a positive correlation with the dielectric constant of organic solvent media.[47] It is noteworthy that the previously proposed discharge mechanism of the primary lithium–sulfur dioxide battery was based on the formation of $S_2O_4^{2-}$ rather than SO_2^- or $LiSO_2$.[39,45] It is our speculation that this finding is most likely due to the use of an acetonitrile-based electrolyte in most primary lithium–sulfur dioxide batteries[8-10,39], which has a high dielectric constant ($\varepsilon \sim 35.9$)[48,49] comparable to that of EC/DMC. Although the overall processes to attain the final product of

$Li_2S_2O_4$ are thermodynamically favorable with identical energy change of overall reactions in both electrolytes as shown in Table 2.2, it should be noted that the energy profiles along the elementary reaction pathways for lithium–sulfur dioxide batteries were significantly different depending on the type of electrolyte. One energy profile consisted of a monotonous downhill process (TEGDME), and the other consisted of a mixed uphill and downhill process involving a significant energy barrier (EC/DMC). This difference in the reaction energetics is expected to affect the nature of the formation of solid discharge products for the lithium–sulfur dioxide battery depending on the type of electrolyte, which will be discussed more in the experimental section.

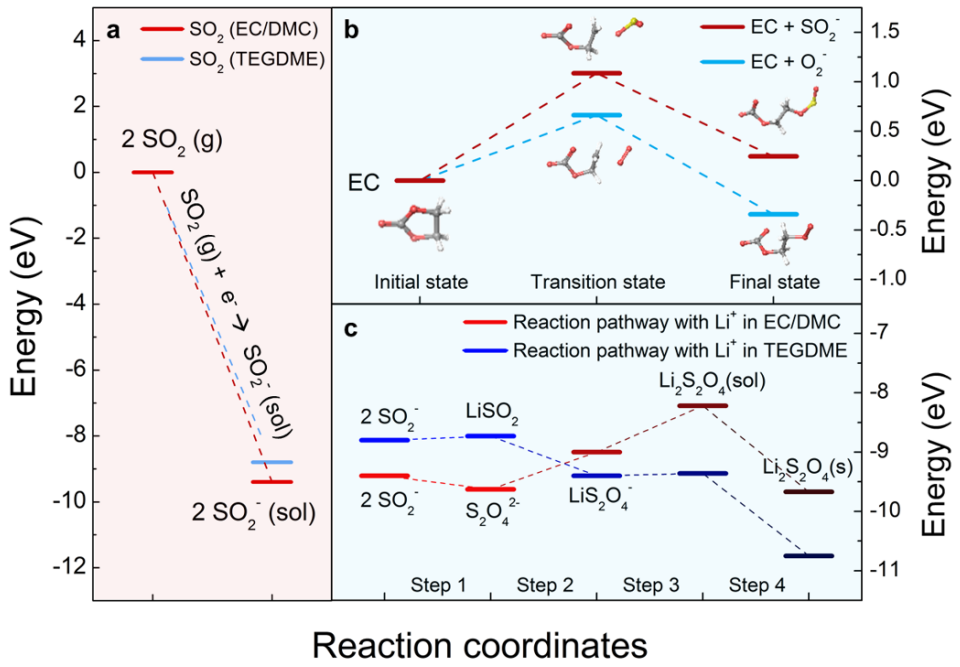

Figure 2.9. DFT calculation of the reaction chemistry of lithium–sulfur dioxide batteries. (a) Energy diagrams for electrochemical reduction reaction of sulfur dioxide gas under EC/DMC and TEGDME. (b) Energy profiles for ICF of chemical EC decomposition reaction by O_2^- (blue) and SO_2^- (red). (c) Reaction pathway between SO_2^- and lithium ions with corresponding energy profiles under EC/DMC (red) and TEGDME (blue).

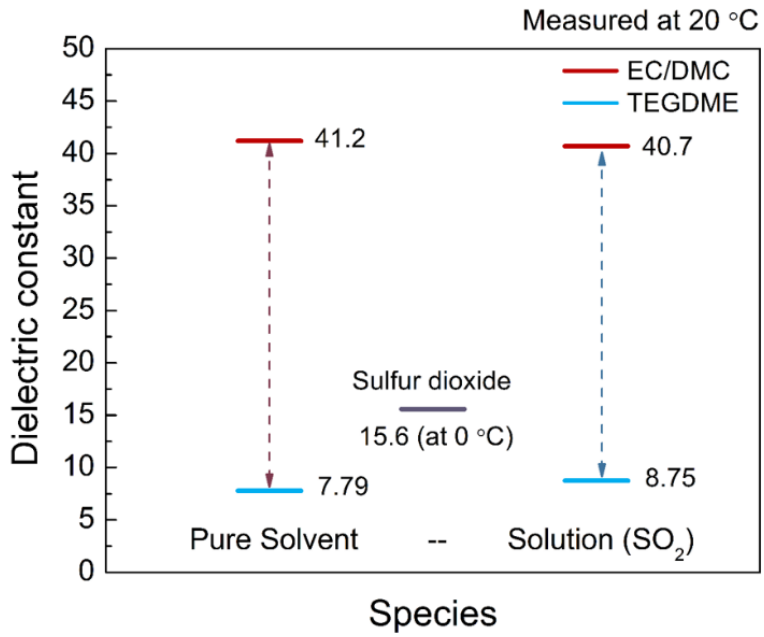

Figure 2.10. Measurements of the dielectric constants of organic solvents with saturation of sulfur dioxide. Organic solutions containing sulfur dioxide were prepared through a simple saturation of sulfur dioxide gas to the organic solvents in a confined chamber under the pressure of 1 bar.

Table 2.2. Elementary reaction steps with corresponding energy changes under carbonate and ether electrolyte.

EC/DMC	Reaction	ΔE (eV)
C-1	$2SO_2(g) + 2e^- \rightarrow 2SO_2^-(soln)$	-4.69 x 2
C-2	$2SO_2^-(soln) \rightarrow S_2O_4^{2-}(soln)$	-0.21
C-3	$S_2O_4^{2-}(soln) + Li^+(soln) \rightarrow LiS_2O_4^-(soln)$	+0.69
C-4	$LiS_2O_4^-(soln) + Li^+(soln) \rightarrow Li_2S_2O_4(soln)$	+0.60
C-5	$Li_2S_2O_4(soln) \rightarrow Li_2S_2O_4(s)$	-1.42
A-1	$2Li(s) \rightarrow 2Li^+(soln) + 2e^-$	+1.63 x 2
Total	**$2SO_2(g) + 2Li(s) \rightarrow Li_2S_2O_4(s)$**	**-3.23 x 2**

TEGDME	Reaction	ΔE (eV)
C-1	$2SO_2(g) + 2e^- \rightarrow 2SO_2^-(soln)$	-4.36 x 2
C-2	$SO_2^-(soln) + Li^+(soln) \rightarrow LiSO_2(soln)$	-0.01
C-3	$LiSO_2(soln) + SO_2^-(soln) \rightarrow LiS_2O_4^-(soln)$	-0.82
C-4	$LiS_2O_4^-(soln)\ Li^+(soln) \rightarrow Li_2S_2O_4(soln)$	-0.04
C-5	$Li_2S_2O_4(soln) \rightarrow Li_2S_2O_4(s)$	-1.33
A-1	$2Li(s) \rightarrow 2Li^+ + 2e^-$	+2.22 x 2
Total	**$2SO_2(g) + 2Li(s) \rightarrow Li_2S_2O_4(s)$**	**-3.24 x 2**

2.2.3.2 Feasibility of Li–SO_2 chemistry in carbonate electrolytes

Inspired by the theoretical findings, we constructed lithium–sulfur dioxide cells using the conventional carbonate electrolyte EC/DMC (1:1 volume ratio with 1 M $LiPF_6$) and examined the stability of the rechargeable lithium–sulfur dioxide chemistry. Figure 2.11a presents the galvanostatic voltage profile during the first cycle of the lithium–sulfur dioxide cell. The electrochemical profile at 0.2 mA/cm^2 resembles the typical profile of the lithium–sulfur dioxide cells using an ether-based electrolyte in a previous study.[37] To confirm the reversible electrochemical reactions, we performed several analyses of lithium–sulfur dioxide cells using the galvanostatic intermittent titration technique (GITT), differential electrochemical mass spectroscopy (DEMS), X-ray diffraction (XRD), and scanning electron microscopy (SEM). Figure 2.11b indicates that the equilibrium potentials measured by GITT are in an agreement with the thermodynamic potential of $Li_2S_2O_4$ (~3 V)[50], which supports the idea that the main reaction involves the formation and decomposition of $Li_2S_2O_4$. Furthermore, the DEMS results in Figure 2.11c indicate that the sulfur dioxide gas was solely detected without the evolution of other gases during the entire charge process, demonstrating the reversible and stable charge reaction occurring in the lithium–sulfur dioxide cell. Considering that the oxygen evolution during the charging of conventional lithium–oxygen cells is typically accompanied by the release of considerable amounts of carbon dioxide due to electrolyte decomposition[15,17] and carbon deterioration[51,52], the absence of carbon dioxide in this experiment supports the idea that the EC/DMC

electrolyte as well as the carbon electrode used for lithium–sulfur dioxide cells remain stable during the cell operation. In addition to the evidence on a gas phase evolution of sulfur dioxide through *in situ* gas analyses, the characterization of electrolytes after charge of the lithium–sulfur dioxide cells with UV-vis spectroscopy in Figure 2.12 clearly confirms the reversible evolution of sulfur dioxide from the electrolyte solution.[53,54]

To further verify the electrochemical reaction, we carefully performed *ex situ* analyses on the gas-electrodes of lithium–sulfur dioxide cells at different states of charge or discharge, as shown in Figure 2.11a. The *ex situ* XRD spectra in Figure 2.11d reveal that characteristic peaks of $Li_2S_2O_4$ appear and grow during discharge without any notable byproducts, followed by the reduction of these peaks during the charge and their complete disappearance after the end of the charge.[38,55] These results evidently confirm that the reversible formation and decomposition of $Li_2S_2O_4$ is the major electrochemical reaction occurring in the lithium–sulfur dioxide system using an EC/DMC electrolyte, which is consistent with the DFT calculations. In addition, the formation and decomposition of $Li_2S_2O_4$ can be directly probed by tracking the morphological evolution on the electrode in the *ex situ* SEM images in Figure 2.11e. It is apparent that two-dimensional plates begin to appear on the carbon gas-electrode upon discharge and grow up to approximately 5 μm in size, covering all the carbon surfaces at the end of discharge. Upon the charge process, $Li_2S_2O_4$ gradually disappears; at the end of charge to 4.2 V, no micron plate was observed in the electrode, and the porous structure of the

gas-electrode was well recovered to its pristine state, which is in a good agreement with the XRD results. Note that the morphological feature of the discharge product is slightly different from that of the $Li_2S_2O_4$ formed using the TEGDME electrolyte in our previous study.[37] As carefully compared in Figure 2.13, the $Li_2S_2O_4$ initially forms needle-like precipitates and grows into numerous nanoribbons for the TEGDME electrolyte, in contrast to the micron-sized $Li_2S_2O_4$ plate in the EC/DME electrolyte. Interestingly, the morphology of discharge products has recently been regarded as an important clue to understanding the discharge mechanism of metal–oxygen batteries.[21-23,56] In the lithium–oxygen battery system, for instance, highly solvating electrolytes with a high donor number or solvating additives promote the nucleation and growth of the crystalline toroidal Li_2O_2 with a typically large particle size by driving the solution-mediated process, whereas electrolytes with low donor numbers tend to form film-like discharge products on the surface of the electrode.[21,22,57] According to the reaction pathways examined by the DFT calculations in Figure 2.9c, it is believed that the intermediate energy uphill processes in the EC/DMC electrolyte would play an important role in governing the nucleation of solid precipitates because of the critical energy barrier, in contrast to the case of TEGDME, where there is no energy barrier for the discharge process. Because the number of nuclei is generally inversely proportional to the nucleation energy barriers, we presumed that a small number of nuclei generated under highly solvating EC/DMC electrolyte yield to form the relatively well-grown micron-sized discharge products of $Li_2S_2O_4$. Further study must be performed to

understand the relationship between the discharge mechanism and the feature of the discharge products in the lithium–sulfur dioxide system.

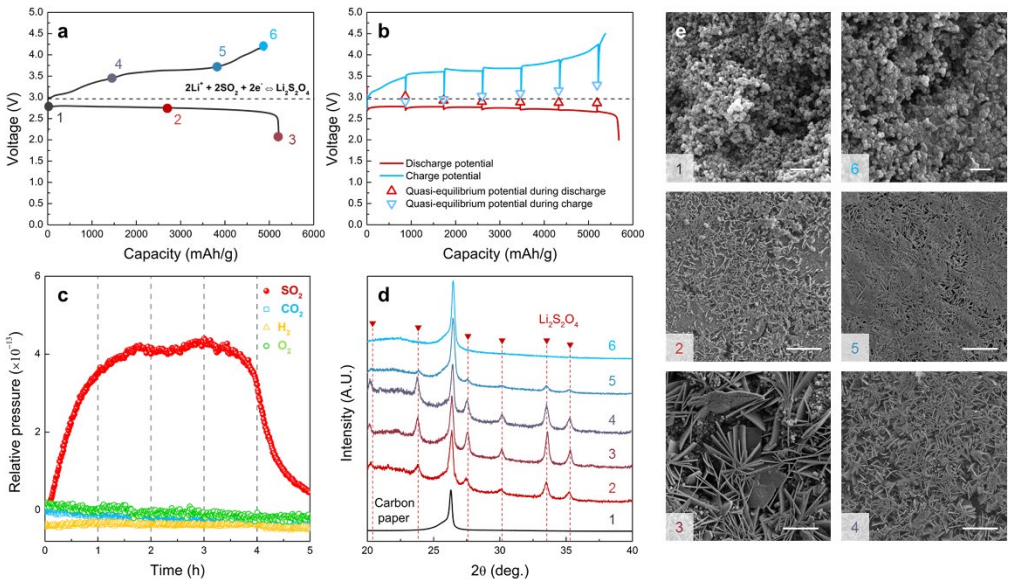

Figure 2.11. Reversible chemistry of lithium–sulfur dioxide batteries under carbonate-based electrolyte. (a) Galvanostatic discharge/charge profile of lithium–sulfur dioxide cell at a current density of 0.2 mA cm^{-2}. (b) GITT analysis result of lithium–sulfur dioxide cell. (c) *In situ* gas analysis during charge process of the lithium–sulfur dioxide cell by DEMS. (d) *Ex situ* XRD spectra of gas-electrodes for lithium–sulfur dioxide cells. (e) Corresponding *ex situ* SEM images of the gas-electrodes of lithium–sulfur dioxide cells. (scale bar 300 nm (1,6)) (scale bar 5 μm (2-5))

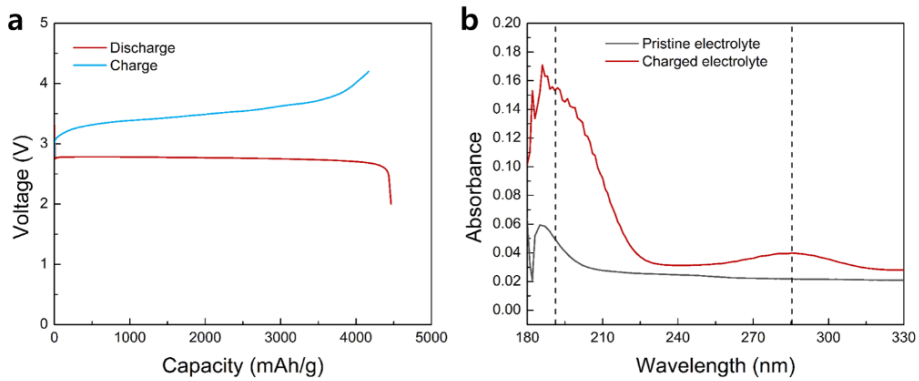

Figure 2.12. Reversible SO_2 evolution in the electrolyte solutions. (a) Discharge profile of closed-type lithium-sulfur dioxide cells by using SO_2 saturated EC/DMC electrolyte (Red) and charge profile of rebuilt cell with fresh electrolyte and pre-discharged gas electrode (Blue). (b) UV-vis spectra of the electrolyte solution after charging the pre-discharged gas-electrode.

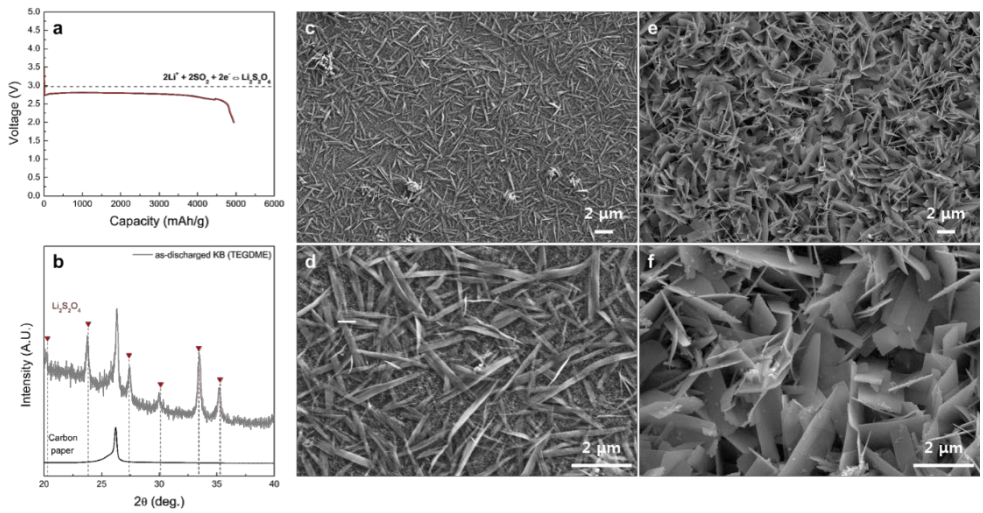

Figure 2.13. Comparison of morphological evolution of discharge products under carbonate and ether electrolytes. (a) Discharge profiles of lithium–sulfur dioxide cells with TEGDME electrolyte. (b) XRD pattern of discharged electrode of lithium–sulfur dioxide cells. (c–f) SEM images of discharge products on the carbon cathodes with (c,d) ether electrolyte and (e,f) carbonate electrolyte.

2.2.3.3 Performance of Li–SO_2 cells using carbonate electrolytes.

Having confirmed the reversible $Li_2S_2O_4$ formation in the carbonate-based electrolyte, the electrochemical properties of lithium–sulfur dioxide cells were comparatively investigated in EC/DMC and TEGDME electrolytes. Figure 2.14a and 2.14b compare the power capability of lithium–sulfur dioxide cells under current rates ranging from 0.2 to 5.0 mA cm^{-2} during discharge. Interestingly, a significantly higher rate capability is achievable with the cell employing the EC/DMC electrolyte for an identical cell configuration. Although similar discharge capacities are delivered at a low current rate of 0.2 mA cm^{-2} for the two cases, the cell with EC/DMC is capable of delivering more than 70% of the initial capacity even at 25 times higher current density; in contrast, the cell with TEGDME exhibits a negligible capacity at the same current rate. It is speculated that the facile ion transport in EC/DMC, which exhibits approximately 4 times higher ionic conductivity than TEGDME, as shown in Table 2.3, contributes to the high rate capability of the lithium–sulfur dioxide cell. To verify the reversible $Li_2S_2O_4$ formation/decomposition in such a high-rate operation, the *ex situ* analyses were performed again under the condition shown in Figure 2.15, which revealed identical results regardless of the applied current densities. In Figure 2.14c, the cycling properties of lithium–sulfur dioxide cells were comparatively investigated at a constant rate of 0.2 mA cm^{-2}. The lithium–sulfur dioxide cell with EC/DMC stably operated over 80 cycles, whereas that with the TEGDME electrolyte maintained approximately 20 cycles, which is consistent with the previous report.[37]

Moreover, better cycle stability of the cell with EC/DMC was again confirmed with the larger capacity utilization of 1,000 mAh/g, as shown in Figure 2.16. Note that no special treatment such as nanoscale gas-electrode design or the use of a catalyst was applied during the test, under which conventional lithium–oxygen or sodium–oxygen batteries would exhibit significantly less cycle stability.[58-61] Even at a higher current density of 1 mA cm^{-2}, the Li–SO_2 cell with EC/DMC could sustain a high cycle stability of approximately 50 cycles, as observed in Figure 2.17, supporting the idea that simply replacing the electrolyte could markedly enhance the cycling properties of lithium–sulfur dioxide cells. The superior cycling performance of the lithium–sulfur dioxide cell with EC/DMC is attributed to the stability of the carbonate-based electrolyte in the presence of the strongly solvated intermediate SO_2^- product and the better chemical compatibility with the lithium anode, which will be discussed later.

To examine the practical viability of the lithium–sulfur dioxide cells, it was attempted to further enhance the energy efficiency using an appropriate catalyst to promote the charging reaction. A soluble catalyst of 5,10-dimethylphenazine (DMPZ) was introduced into the electrolyte to decrease the charge polarization, which was recently reported as an efficient soluble catalyst for lithium–oxygen batteries.[62] Figure 2.14d presents the characteristic discharge/charge profiles with the DMPZ catalysts for the two lithium–sulfur dioxide cells, which reveals substantial reduction in the charge overpotential. The charging voltage, *i.e.,* the oxidation potential of DMPZ, in the TEGDME electrolyte was analogous to that

in our previous study in lithium–oxygen batteries.[62] However, surprisingly, the cell with the DMPZ catalyst in the EC/DMC electrolyte could be recharged at a voltage plateau of approximately 3.0 V, which is almost identical to the thermodynamic potential of $Li_2S_2O_4$. Thus, the overall polarization of the cells was only 0.2 V, resulting in an energy efficiency of ~93.3%, one of the highest values accomplished with lithium–gas-type batteries. This finding indicates that DMPZ is not only capable of chemically decomposing $Li_2S_2O_4$, similar to the case of Li_2O_2 in lithium–oxygen batteries, but also enables much a higher charging efficiency in the carbonate-based electrolyte. To confirm this unexpected dependency of the redox potential of DMPZ on the electrolyte species, the cyclic voltammetry test and galvanostatic charging in the inert atmosphere were performed again for the DMPZ dissolved in each electrolyte with the three-electrode configuration, as shown in Figure 2.18. DMPZ consistently exhibited a lower oxidation potential in EC/DMC than in TEGDME by approximately 0.2 V. The lower oxidation potential of DMPZ under the carbonate electrolyte might be attributed to the strong stabilization effect on the charged species of $DMPZ^+$ due to the highly solvating environment offered by the carbonate electrolytes. The alternation in the redox potential of soluble catalysts depending on the electrolyte media was also observed in a recent study, where the redox potential of a LiI catalyst was notably different in dimethoxyethane (DME) than in TEGDME.[63] *Ex situ* XRD analysis confirmed that the catalytic activity of DMPZ in decomposing $Li_2S_2O_4$ could be maintained even with the lower redox potential of DMPZ in EC/DMC. Figure 2.14e shows

that characteristic diffraction patterns of $Li_2S_2O_4$ were observed in the discharged electrode but disappeared after the charging, indicating the effective decomposition of the discharge product. Figure 2.19 further confirms the charging reaction based on the decomposition of $Li_2S_2O_4$ by the DMPZ catalyst through X-ray photoelectron spectroscopy (XPS) and *in situ* gas analysis. Upon charging of the cell, the XPS signature of $Li_2S_2O_4$ gradually fades away, which is accompanied by the evolution of sulfur dioxide without any other detectable gases, implying the efficient catalytic behavior of DMPZ for lithium–sulfur dioxide cells.

We further investigated the electrochemical performance of the lithium–sulfur dioxide cell employing the carbonate electrolyte with the DMPZ catalyst. Figure 2.14f shows the power capability of the cell for current densities ranging from 0.2 to 5.0 mA cm^{-2} under a controlled capacity of 0.5 mAh. Although the overall polarization systematically increased as the applied current increased, the charge processes of all the cells could be performed below 4 V without exceeding the voltage limit, demonstrating the fast kinetics of the $Li_2S_2O_4$ formation and decomposition aided by DMPZ. It was observed that the efficient catalytic activity of the DMPZ could also lead to a remarkable enhancement in the cycling performance of lithium–sulfur dioxide cells. Figure 2.14g shows that the lithium–sulfur dioxide cells employing EC/DMC with the DMPZ catalyst exhibit superior cycle stability of more than 450 cycles of 0.5 mAh, which has rarely been recorded for lithium–oxygen batteries with such a large absolute capacity. During 450 cycles of the lithium–sulfur dioxide cells, the charging overpotential was only

slightly increased, maintaining the high energy efficiency of the cell, as observed in the inset of Figure 2.14g. This finding indicates that the catalytic activity of DMPZ is stably maintained and not consumed during the cell operations. All the electrochemical results support the idea that a battery with superior power, efficiency, and reversibility is achievable using the lithium–sulfur dioxide chemistry by employing a carbonate-based electrolyte and soluble catalyst.

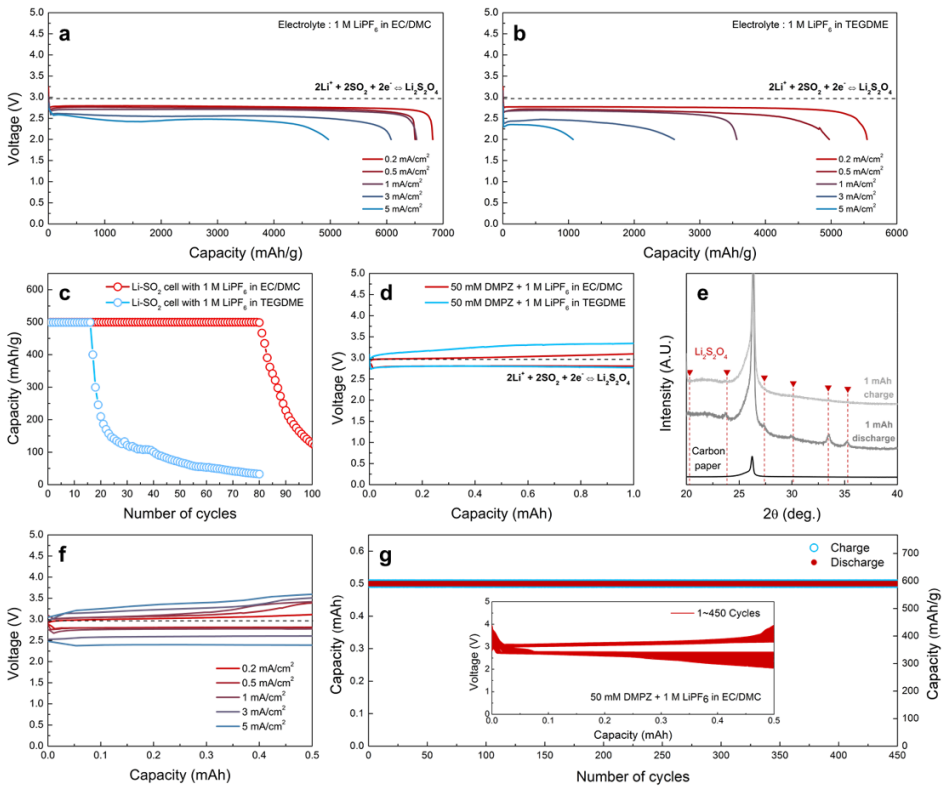

Figure 2.14. Electrochemical performance of lithium–sulfur dioxide batteries. (a,b) Discharge rate capability of lithium–sulfur dioxide cell: (a) with carbonate electrolyte, (b) with ether electrolyte, (c) Cycle properties of lithium–sulfur dioxide cells at 0.2 mA cm^{-2}. (d) Electrochemical profiles of lithium–sulfur dioxide cells with a soluble catalyst. (e) XRD spectra of discharged and recharged gas-electrode of lithium–sulfur dioxide cell with soluble catalyst. (f,g) Electrochemical performance of lithium–sulfur dioxide cells with soluble catalyst containing carbonate-based electrolyte: (f) Power capability of the cells under limited capacity of 0.5 mAh. (g) Cyclability of the cell at 1 mA cm^{-2}. (inset: electrochemical profiles during 450 cycles.)

Table 2.3. Measured ionic conductivities of carbonate and ether electrolytes with and without saturated SO_2 gas.

σ_{ion} [mS cm^{-1}]	Without SO_2	SO_2 bubbled	Reference
1 M $LiPF_6$ in EC/DMC	11.35 ± 0.37	11.84 ± 0.26	11.7 [30]
1 M LiTFSi in TEGDME	2.91 ± 0.04	3.35 ± 0.01	2.72 [64]
1 M $LiPF_6$ in TEGDME	2.33 ± 0.01	2.70 ± 0.05	1.86 [65]

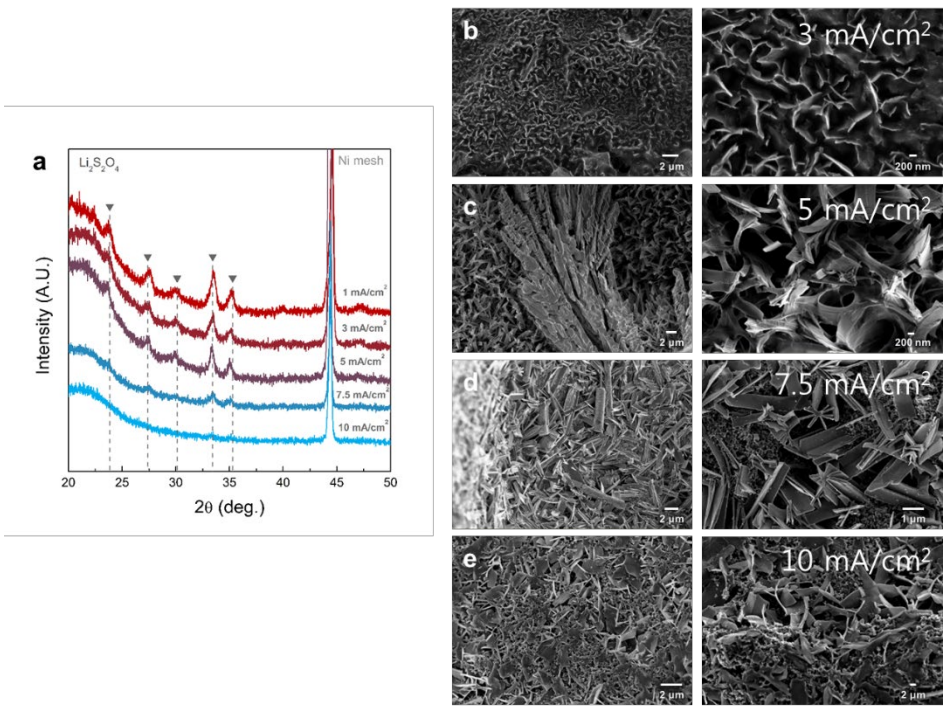

Figure 2.15. Identification of discharge products and corresponding morphological observations. (a) XRD patterns of discharged cathode of lithium–sulfur dioxide cells with different current densities. (b–e), Corresponding SEM images of discharged cathodes at (b) 3 mA/cm^2, (c) 5 mA/cm^2, (d) 7.5 mA/cm^2, and (e) 10 mA/cm^2. The high-intensity peaks at 44° correspond to the Ni mesh current collector. Ni mesh was used particularly for the rate capability tests to achieve a high electric conductivity for the current collecting substrate when applying a high current density.

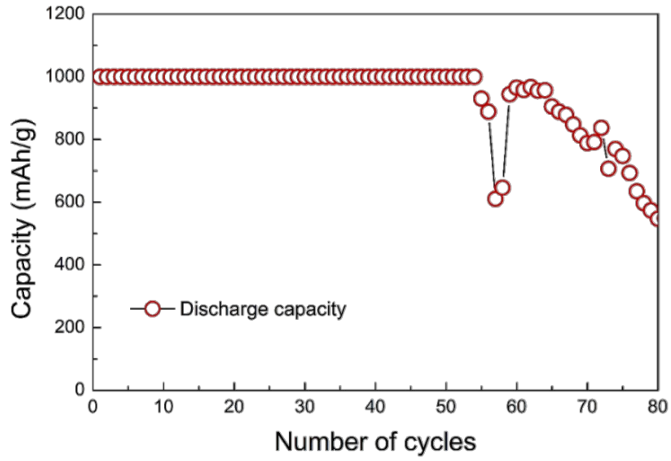

Figure 2.16. Cycle properties under a capacity of 1,000 mAh/g of lithium-sulfur dioxide batteries with carbonate-based electrolytes.

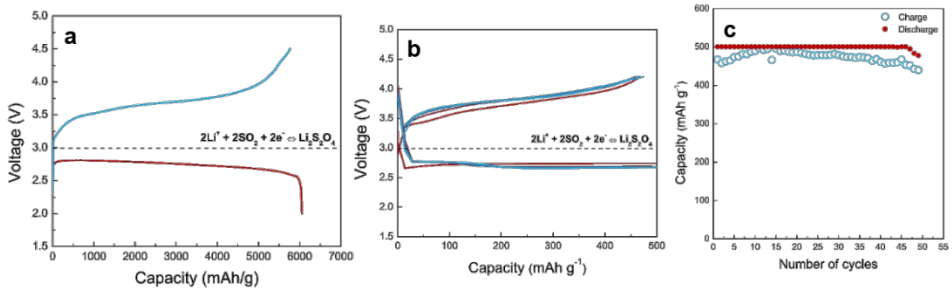

Figure 2.17. Electrochemical properties of lithium–sulfur dioxide cells with carbonate electrolyte at high current density of 1 mA/cm^2. (a) Galvanostatic discharge/charge profiles of lithium–sulfur dioxide cells at 1 mA/cm^2 with voltage cut-offs of 2 and 4.5 V. (b) Electrochemical profiles of lithium–sulfur dioxide cells at 1 mA/cm^2 with capacity cut-off of 500 mAh/g for 5 cycles. (c) Corresponding cyclability of lithium–sulfur dioxide cells.

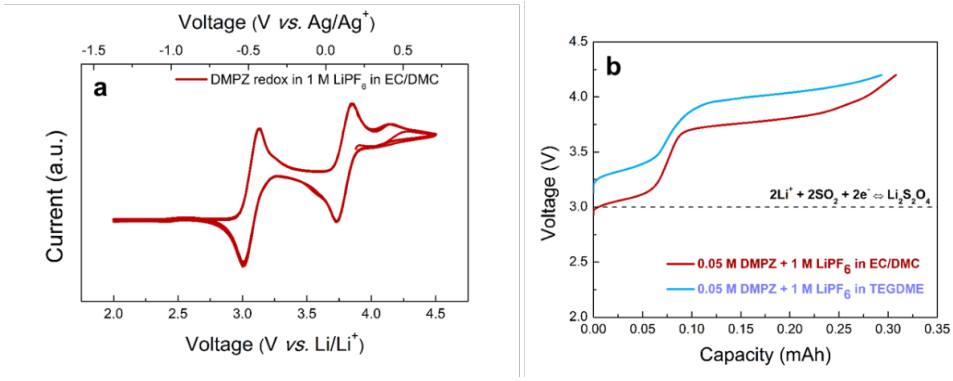

Figure 2.18. Redox potentials of DMPZ soluble catalyst under different electrolytes. (a) Cycle voltammogram of 50 mM DMPZ dissolved in 1 M $LiPF_6$ in EC/DMC at a scan rate of 100 mV/s with 3-electrode cell configuration. (working electrode: gold; counter electrode: platinum; reference electrode: 0.05 M $Ag/AgNO_3$ in acetonitrile) (b) Galvanostatic charge profiles of 50 mM DMPZ dissolved in 1 M $LiPF_6$ in EC/DMC and TEGDME at 0.2 mA/cm^2 under Ar atmosphere with 2-electrode cell configuration.

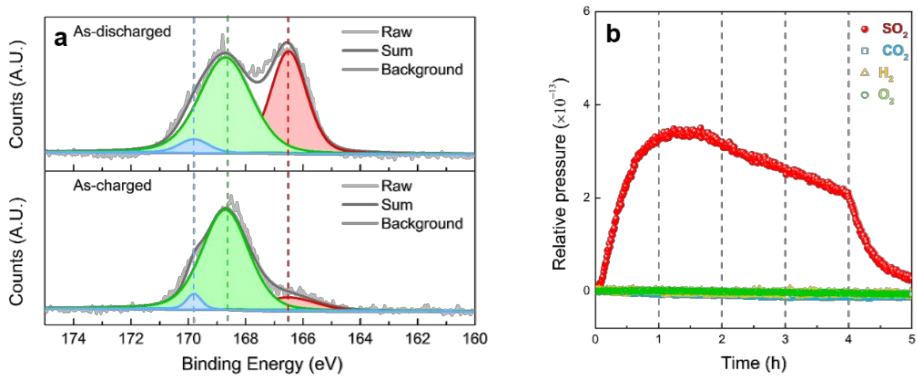

Figure 2.19. Electrochemical activity of DMPZ soluble catalyst in lithium–sulfur dioxide cells with carbonate electrolyte. (a) *Ex situ* XPS results of discharged and charged cathodes for lithium–sulfur dioxide cells with DMPZ catalyst. (b) *In situ* gas analysis results of lithium–sulfur dioxide cells with DMPZ catalyst during charge through DEMS.

2.2.3.4 Discussion

Despite the impressive cycle properties achieved with the catalyst, the origin of the cycle degradation should be understood for further development of lithium–sulfur dioxide batteries. Given the improved cycle stability of the cell using the EC/DMC electrolyte, we attempted to comparatively elucidate how the different electrolytes affect the cycling performance by probing the respective degradation of the carbon gas-electrode and lithium metal anode in addition to the electrolyte stability itself.[17,66] After the cell degradation in Figure 2.14c, the cells were disassembled and each electrode was collected; the cells were then rebuilt with a fresh counter electrode and new electrolyte. Figure 2.20a compares the cycling properties of two rebuilt cells based on EC/DMC: one with the cycled lithium anode (red) and the other with the cycled gas-electrode (blue). Interestingly, the lithium–sulfur dioxide cell with the cycled lithium metal anode could reproduce the original cyclability of approximately 80 cycles, which suggests that the lithium metal cycled in the EC/DMC electrolyte was not significantly degraded. Note that the experiment was performed without DMPZ catalysts; thus, the original cycle life was approximately 80 cycles in Figure 2.14c. However, the rebuilt cell with the cycled gas-electrode could not cycle stably. This finding clearly indicates that the degradation of the gas-electrode is the main cause of the overall cycle deterioration in lithium–sulfur dioxide cells using the EC/DMC electrolyte. In contrast, the opposite result was observed for the same experiments conducted for the cells employing the TEGDME electrolyte, as shown in Figure 2.20b. The

rebuilt cell with the cycled gas-electrode exhibited similar cycle properties of approximately 20 reversible cycles as the original cell in Figure 2.14c. However, the cell with the cycled lithium metal anode could not stably function, as observed in Figure 2.20b, indicating that the degraded lithium metal anode was the main cause of the rapid cycle deterioration of the lithium–sulfur dioxide cells using the TEGDME electrolyte. The severe degradation of lithium metal was again supported by an experiment in which the lithium metal anode was replaced multiple times, which led to a comparable cycling property as that of the rebuilt cell using the cycled gas-electrode, as shown in Figure 2.21. To confirm the higher stability of the lithium metal anode in EC/DMC, a lithium metal symmetric cell was constructed, as shown in Figure 2.20c. The usage of the carbonate electrolyte led to a much smaller polarization and longer operating time than those using the ether electrolyte, which is in a good agreement with previous studies.[67,68] This finding supports the idea that the better cycling properties of the lithium–sulfur dioxide cells employing EC/DMC are partly attributable to the highly stable lithium metal interfaces because of better lithium metal compatibility with the carbonate electrolyte.

For a more comprehensive understanding of the cycle degradation of lithium–sulfur dioxide cells employing the carbonate electrolyte, we examined the carbon gas-electrode after the cycling. The XRD patterns in Figure 2.20d reveal that after charging, the $Li_2S_2O_4$ discharge product was hardly detectable; however, the characteristic peak of Li_2SO_4 began to appear appreciably even after 40 cycles,

and a substantial amount of Li_2SO_4 byproducts are detected at the end of the cycles. Although the expected discharge product, $Li_2S_2O_4$, was clearly decomposed in the cycled cathodes, it is speculated that the gradual deposition of the insulating byproducts on the carbon gas-electrode would have a negative effect on the cycling behavior of lithium–sulfur dioxide cells. Moreover, examination of the morphology of the cycled gas-electrodes clearly revealed that all the active pores of the gas-electrodes were mostly blocked, as observed in Figure 2.20e. Energy-dispersive X-ray spectroscopy (EDS) analysis revealed that the densely clogged pores of the cycled gas-electrode were mainly composed of sulfur and oxygen. The gradual deposition of insulating byproducts results in the significant increase of total impedances of lithium–sulfur dioxide cells, which is confirmed through the electrochemical impedance spectroscopy analyses with cycling the cells as shown in Figure 2.22. Consequently, the accumulation of inactive and insulating byproducts on the pores of the gas-electrode would restrict the active reaction sites and the transport of reactants, including lithium ions and sulfur dioxide gas, finally resulting in the cell failures. In previous studies on primary lithium–sulfur dioxide batteries, the formation of such byproducts has generally been attributed to the self-decomposition of $Li_2S_2O_4$ due to its thermodynamic instability.[11,55,69] According to the XPS analysis of the surface of the cycled cathodes in Figure 2.20f, four different oxidation states of S were detected, including the residual discharge product, $Li_2S_2O_4$, at 166.5 eV. The two major peaks at 168.7 and 169.8 eV are assigned to the sulfur from Li_2SO_3 and Li_2SO_4, respectively, which is consistent with our

previous study[37]. The presence of the Li_2SO_4 byproduct corresponds well to the XRD result in Figure 2.20d. Note that a trace amount of elemental sulfur (164.1 eV) was detected in the XPS spectra, which hints at the formation mechanism of Li_2SO_4. According to the self-decomposition of $Li_2S_2O_4$, which can occur spontaneously, as indicated by the DFT calculations in Table 2.4, it should accompany the generation of elemental sulfur, *i.e.,* $Li_2S_2O_4$ (s) → Li_2SO_4 (s) + S (s). The presence of both elemental sulfur and Li_2SO_4 in the cycled gas-electrode strongly suggests that the self-decomposition of the discharge product can cause deterioration of the cycle performance. Conclusively, a strategy for improving the stability of discharge products and suppressing the formation of byproducts should be further explored to develop a better-performing lithium–sulfur dioxide battery.

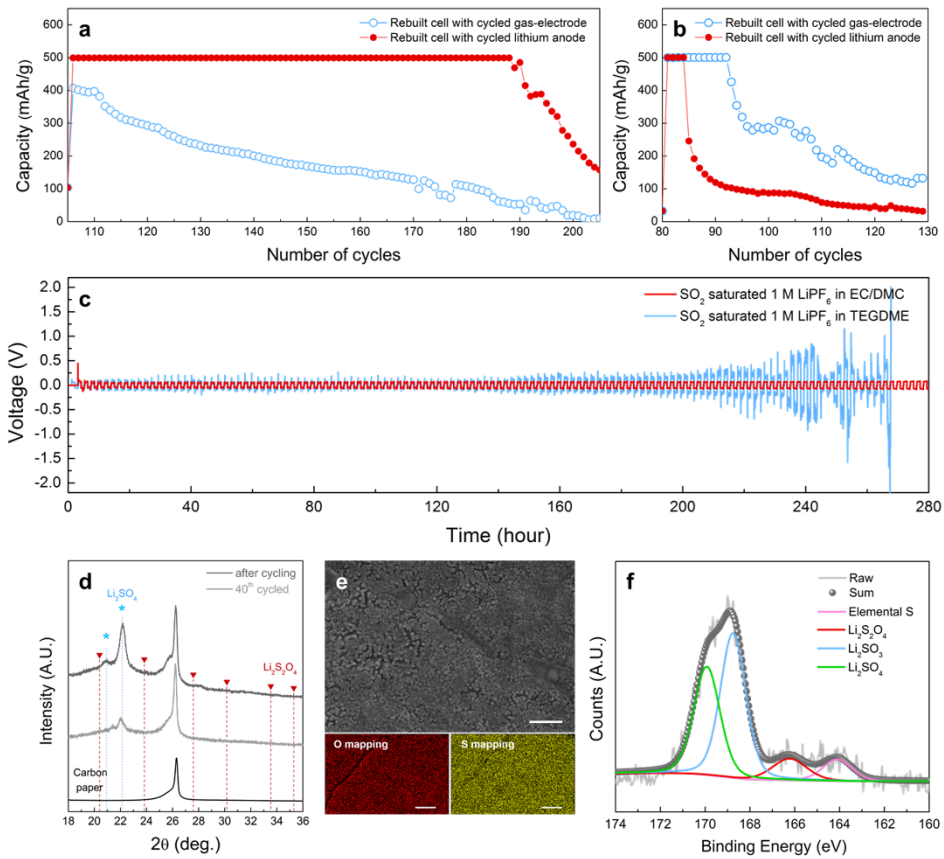

Figure 2.20. Investigation of cycle degradation of lithium–sulfur dioxide batteries. (a,b) Cycle properties of rebuilt cells with cycled gas-electrode or cycled lithium anode: (a) under carbonate electrolyte. (b) under ether electrolyte. (c) Lithium symmetric cell test at a current density of 1 mA cm^{-2} with SO_2-saturated EC/DMC (red) and TEGDME (blue). (d) XRD spectra of gas-electrode of lithium–sulfur dioxide cells at the middle and end of cycles. (e) SEM images (scale bar 500 nm) of gas-electrode at the end of cycle and elemental mapping by EDS (scale bar 50 μm). (f) XPS S 2p spectra for gas-electrode after cycling of lithium–sulfur dioxide cell.

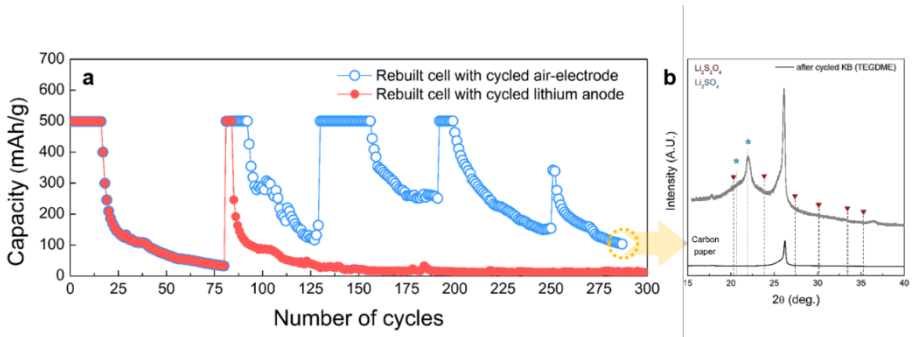

	Initial	1st rebuilt	2nd rebuilt	3rd rebuilt	4th rebuilt	Summation
Cyclability	16	12	27	8	0	63

Figure 2.21. Cycle capability of carbon cathodes for lithium–sulfur dioxide cell with ether electrolyte. (a) Cycle properties of continuously rebuilt lithium–sulfur dioxide cells with fresh Li anode after cycling: (b) XRD pattern of cathodes after cycling of lithium–sulfur dioxide cell.

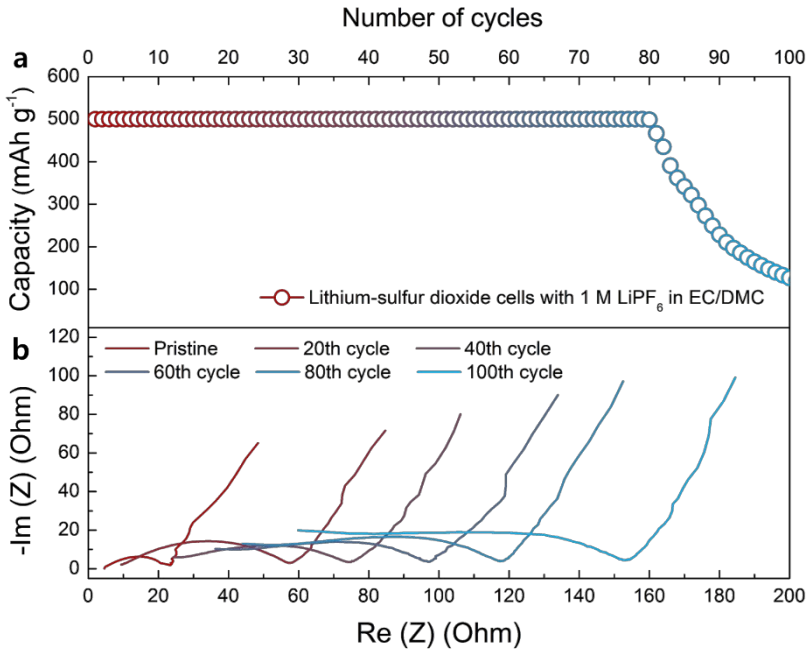

Figure 2.22. Electrochemical impedance spectroscopy results of lithium-sulfur dioxide cells with cycling. (a) Cyclability of lithium-sulfur dioxide cells under a limited capacity of 500 mAh/g. (b) Nyquist plots for the impedances of the cell with cycling.

Table 2.4. Theoretical reaction energy changes for possible formation pathways of byproduct Li_2SO_4 in lithium–sulfur dioxide cell atmosphere.

Li_2SO_4	Reaction	ΔE
(1)	$2Li^+ + SO_4^{2-} \rightarrow Li_2SO_4$ (s)	+0.08 eV
(2)	$Li_2S_2O_4$ (s) $\rightarrow Li_2SO_4$ (s) + 1/8 S_8	-1.18 eV

2.2.4 Concluding Remarks

We successfully employed a conventional carbonate-based electrolyte in rechargeable lithium–sulfur dioxide batteries and validated the feasibility of the system through combined theoretical and experimental verifications. The chemical stability of the carbonate electrolyte against the reduced form of SO_2 allowed lithium–sulfur dioxide cells to be reversibly operated, unlike the conventional lithium–oxygen systems. The high ionic conductivity and chemical compatibility with the lithium metal anode led to a remarkable improvement of the lithium–sulfur dioxide cell performances, including the power capability and cycle stability. Furthermore, the application of a DMPZ catalyst yielded one of the highest efficiencies (~93.3%) and reversibilities (450 cycles) reported for metal–gas systems to date. Toward the realization of a practical rechargeable lithium–sulfur dioxide battery system, several issues still need to be addressed, including the lack of fundamental understanding and safety issues regarding the use of a toxic gas. In this regards, more quantifiable characterization techniques inclusive of pressure monitoring[70,71] and chemical titration methodology[22,72], currently introduced in the research of metal-air batteries, should be considered for the elucidation of precise gas efficiency or side-reaction mechanism of the lithium–sulfur dioxide chemistry in following studies. In addition, taking advantage of the commercialized primary lithium–sulfur dioxide battery technology, closed-type pressurized systems could be one of the practically

approachable models for the safe lithium–sulfur dioxide secondary battery with potential merits of the enhanced operation voltage and the reversibility obtained in our preliminary experiments as described in Figure 2.23 and Supplementary Note 2.1. Nevertheless, this study offers insights to the metal–air battery community regarding the importance of the electrolyte and its compatibility with the lithium or sodium metal electrode considering that the exceptionally high theoretical capacity of lithium/sodium–oxygen batteries is partly attributed to the use of a metallic lithium or sodium electrode. Thus, more studies should focus on how to rationally control the interaction between the electrolyte and metal anodes in metal–oxygen batteries. We hope that this report will pave the way for a new field of lithium–sulfur dioxide batteries as a promising next-generation battery system and spur vigorous discussions in the search for a robust electrolyte in the metal–air battery community.

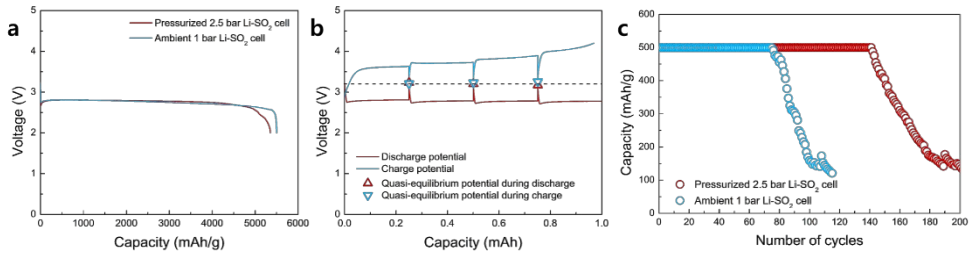

Figure 2.23. Electrochemical properties of pressurized lithium-sulfur dioxide cells. (a) Discharge profiles for the 1st cycle of the ambient pressure cell and pressurized cell. (b) GITT analysis result of pressurized cells. (c) Cyclability of the ambient pressure cells and pressurized cells.

Supplementary Note 2.1

We constructed the lithium–sulfur dioxide cells confined with high-pressure sulfur dioxide gas and examined the electrochemical performances of the cell by means of full discharge, GITT, and cycle tests. The cell with the pressure of 2.5 bar was investigated, which is the maximum pressure achievable in our lab-scale pressurized cell setup. Excessive pressurization with sulfur dioxide was avoided due to the safety concerns in this study. Figure 2.2.15a presents the discharge profile for the 1st cycle of the pressurized cell, showing that almost identical discharge capacity and voltage were obtained to those of the ambient pressure cell. The invariance of the discharge capacity regardless of the gas pressure is attributed to fact that the deliverable capacities of the current lithium–sulfur dioxide cells are limited by the gas-electrode surface area where the full accommodation of discharge products induces the rapid increase in the overpotential. In order to more closely examine the reaction voltage of the pressurized cells, GITT analysis was carried out to measure the quasi-equilibrium potentials of the cells. As shown in Figure 2.2.15b, a slightly increased open circuit potential of 3.2 V (vs. Li/Li$^+$) was obtained in the pressurized cell compared with the value of 3.0 V (vs. Li/Li$^+$) for ambient pressure cell. It is quite reasonable in thermodynamic aspects that the high activity of the gas from the increased pressure might result in a more negative value of the Gibbs free energy change of the total reaction, leading to an increase in the open-circuit potential of the pressurized cells. However, the simple estimation by using Nernst equation ($\Delta E =$

$\frac{RT}{nF} ln\, a_{SO_2} = 0.0235$ V, where n equals to the number of electron transferred, F equals to Faraday constant, R equals to gas constant, T equals to the temperature, and a equals to the activity) shows only 0.02V increase and cannot fully explain the increase of about 0.2 V, which has to be further studied with the careful consideration of total energies of other reactants and products involved in the reactions.

Additionally, we examined the cyclability of the pressurized lithium–sulfur dioxide cells under a limited capacity mode in Figure 2.2.15c. Interestingly, the pressurized cell could exhibit better cycling behavior about 140 times compared to the number of cycles achievable in the ambient-pressure cell. Considering that the thermodynamic stability of $Li_2S_2O_4$ discharge products have a vital role in the formation and accumulation of inactive byproducts including Li_2SO_4 as discussed in the manuscript, it is our speculation that the high pressure atmosphere might have a positive impact on the thermodynamic stability of $Li_2S_2O_4$, probably leading to the enhancement of cycle stability by suppressing the self-decomposition of $Li_2S_2O_4$. Even though the precise origin of the improved electrochemical properties is not fully addressed at the current stage, it has to be further investigated in the following study, and the pressure control of the cell might be one of the possible strategies toward the highly reversible lithium–sulfur dioxide batteries.

2.2.5 References

1 Tarascon, J. M. & Armand, M. Issues and challenges facing rechargeable lithium batteries. *Nature* **414**, 359-367 (2001).

2 Armand, M. & Tarascon, J. M. Building better batteries. *Nature* **451**, 652-657 (2008).

3 Kang, K., Meng, Y. S., Bréger, J., Grey, C. P. & Ceder, G. Electrodes with High Power and High Capacity for Rechargeable Lithium Batteries. *Science* **311**, 977-980 (2006).

4 Abraham, K. M. & Jiang, Z. A Polymer Electrolyte-Based Rechargeable Lithium/Oxygen Battery. *Journal of The Electrochemical Society* **143**, 1-5 (1996).

5 Arico, A. S., Bruce, P., Scrosati, B., Tarascon, J.-M. & van Schalkwijk, W. Nanostructured materials for advanced energy conversion and storage devices. *Nature Materials* **4**, 366-377 (2005).

6 Bruce, P. G., Freunberger, S. A., Hardwick, L. J. & Tarascon, J.-M. Li-O_2 and Li-S batteries with high energy storage. *Nature Materials* **11**, 19-29 (2012).

7 Meyers, B. B. a. J. W. S. W. F. *U.S. Patent* **3**, 242 (1969).

8 Kilroy, W. P. & Dallek, S. Differential scanning calorimetry studies of

possible explosion-causing mixtures in Li/SO_2 cells. *Journal of Power Sources* **3**, 291-295 (1978).

9 Dey, A. & Holmes, R. Safety Studies on Li/SO_2 Cells I. Differential Thermal Analysis (DTA) of Cell Constituents. *Journal of the Electrochemical Society* **126**, 1637-1644 (1979).

10 Linden, D. & McDonald, B. The lithium—sulfur dioxide primary battery—its characteristics, performance and applications. *Journal of Power Sources* **5**, 35-55 (1980).

11 Xing, H. *et al.* Ambient lithium–SO_2 batteries with ionic liquids as electrolytes. *Angewandte Chemie International Edition* **53**, 2099-2103 (2014).

12 Lim, H. D. *et al.* A New Perspective on Li–SO_2 Batteries for Rechargeable Systems. *Angewandte Chemie International Edition* **54**, 9663-9667 (2015).

13 Freunberger, S. A. *et al.* The Lithium–Oxygen Battery with Ether-Based Electrolytes. *Angewandte Chemie International Edition* **50**, 8609-8613 (2011).

14 Freunberger, S. A. *et al.* Reactions in the rechargeable lithium–O_2 battery with alkyl carbonate electrolytes. *Journal of the American Chemical Society* **133**, 8040-8047 (2011).

15 McCloskey, B. D., Bethune, D. S., Shelby, R. M., Girishkumar, G. & Luntz, A. C. Solvents' Critical Role in Nonaqueous Lithium–Oxygen Battery Electrochemistry. *The Journal of Physical Chemistry Letters* **2**, 1161-1166 (2011).

16 Chen, Y., Freunberger, S. A., Peng, Z., Bardé, F. & Bruce, P. G. Li–O_2 battery with a dimethylformamide electrolyte. *Journal of the American Chemical Society* **134**, 7952-7957 (2012).

17 McCloskey, B. *et al.* Twin problems of interfacial carbonate formation in nonaqueous Li–O_2 batteries. *The Journal of Physical Chemistry Letters* **3**, 997-1001 (2012).

18 Walker, W. *et al.* A rechargeable Li–O_2 battery using a lithium nitrate/N, N-dimethylacetamide electrolyte. *Journal of the American Chemical Society* **135**, 2076-2079 (2013).

19 Kim, J., Lim, H.-D., Gwon, H. & Kang, K. Sodium–oxygen batteries with alkyl-carbonate and ether based electrolytes. *Physical Chemistry Chemical Physics* **15**, 3623-3629 (2013).

20 Lim, H.-K. *et al.* Toward a Lithium–"Air" Battery: The Effect of CO_2 on the Chemistry of a Lithium–Oxygen Cell. *Journal of the American Chemical Society* **135**, 9733-9742 (2013).

21 Johnson, L. *et al.* The role of LiO_2 solubility in O_2 reduction in aprotic solvents and its consequences for Li–O_2 batteries. *Nature Chemistry* **6**, 1091-1099 (2014).

22 Aetukuri, N. B. *et al.* Solvating additives drive solution-mediated electrochemistry and enhance toroid growth in non-aqueous Li–O_2 batteries. *Nature Chemistry* **7**, 50-56 (2015).

23 Burke, C. M., Pande, V., Khetan, A., Viswanathan, V. & McCloskey, B. D. Enhancing electrochemical intermediate solvation through electrolyte anion selection to increase nonaqueous Li–O_2 battery capacity. *Proceedings of the National Academy of Sciences* **112**, 9293-9298 (2015).

24 Kwabi, D. G. *et al.* Chemical instability of dimethyl sulfoxide in lithium–air batteries. *The Journal of Physical Chemistry Letters* **5**, 2850-2856 (2014).

25 Kim, J. *et al.* Dissolution and ionization of sodium superoxide in sodium-oxygen batteries. *Nature Communications* **7**, 10670-10677 (2016).

26 Bryantsev, V. S. *et al.* Predicting solvent stability in aprotic electrolyte Li–air batteries: nucleophilic substitution by the superoxide anion radical (O_2^-). *The Journal of Physical Chemistry A* **115**, 12399-12409 (2011).

27 Bryantsev, V. S. & Faglioni, F. Predicting autoxidation stability of ether-

and amide-based electrolyte solvents for Li–air batteries. *The Journal of Physical Chemistry A* **116**, 7128-7138 (2012).

28 Bryantsev, V. S. & Blanco, M. Computational study of the mechanisms of superoxide-induced decomposition of organic carbonate-based electrolytes. *The Journal of Physical Chemistry Letters* **2**, 379-383 (2011).

29 Xu, K. Nonaqueous Liquid Electrolytes for Lithium-Based Rechargeable Batteries. *Chemical Reviews* **104**, 4303-4418 (2004).

30 Xu, K. Electrolytes and Interphases in Li-Ion Batteries and Beyond. *Chemical Reviews* **114**, 11503-11618 (2014).

31 Bochevarov, A. D. *et al.* Jaguar: A high-performance quantum chemistry software program with strengths in life and materials sciences. *International Journal of Quantum Chemistry* **113**, 2110-2142 (2013).

32 Lee, C., Yang, W. & Parr, R. G. Development of the Colle-Salvetti correlation-energy formula into a functional of the electron density. *Physical Review B* **37**, 785-789 (1988).

33 Becke, A. D. Density-functional thermochemistry. III. The role of exact exchange. *The Journal of Chemical Physics* **98**, 5648-5652 (1993).

34 Hariharan, P. & Pople, J. A. The effect of d-functions on molecular orbital energies for hydrocarbons. *Chemical Physics Letters* **16**, 217-219 (1972).

35 Kresse, G. & Furthmüller, J. Efficiency of ab-initio total energy calculations for metals and semiconductors using a plane-wave basis set. *Computational Materials Science* **6**, 15-50 (1996).

36 Perdew, J. P., Burke, K. & Ernzerhof, M. Generalized Gradient Approximation Made Simple. *Physical Review Letters* **77**, 3865-3868 (1996).

37 Lim, H. D. *et al.* A New Perspective on Li–SO_2 Batteries for Rechargeable Systems. *Angewandte Chemie* **127**, 9799-9803 (2015).

38 Rupich, M., Pitts, L. & Abraham, K. Characterization of Reactions and Products of the Discharge and Forced Overdischarge of Li/SO_2 Cells. *Journal of the Electrochemical Society* **129**, 1857-1861 (1982).

39 Bowden, W. L., Chow, L., Demuth, D. L. & Holmes, R. W. Chemical Reactions in Lithium Sulfur Dioxide Cells Discharged at High Rates and Temperatures. *Journal of the Electrochemical Society* **131**, 229-234 (1984).

40 Armand, M. *et al.* Conjugated dicarboxylate anodes for Li-ion batteries. *Nature Materials* **8**, 120-125 (2009).

41 Hu, Y.-S. *et al.* Electrochemical lithiation synthesis of nanoporous materials with superior catalytic and capacitive activity. *Nature Materials*

5, 713-717 (2006).

42 Hong, J. *et al.* Biologically inspired pteridine redox centres for rechargeable batteries. *Nature Communications* **5** (2014).

43 Black, R. *et al.* Screening for superoxide reactivity in Li-O_2 batteries: effect on Li_2O_2/LiOH crystallization. *Journal of the American Chemical Society* **134**, 2902-2905 (2012).

44 Hall, D. S., Self, J. & Dahn, J. R. Dielectric constants for quantum chemistry and Li-ion batteries: solvent blends of ethylene carbonate and ethyl methyl carbonate. *The Journal of Physical Chemistry C* **119**, 22322-22330 (2015).

45 Martin, R. P. & Sawyer, D. T. Electrochemical reduction of sulfur dioxide in dimethylformamide. *Inorganic Chemistry* **11**, 2644-2647 (1972).

46 Lambeth, D. O. & Palmer, G. The kinetics and mechanism of reduction of electron transfer proteins and other compounds of biological interest by dithionite. *Journal of Biological Chemistry* **248**, 6095-6103 (1973).

47 Lough, S. M. & McDonald, J. W. Synthesis of tetraethylammonium dithionite and its dissociation to the sulfur dioxide radical anion in organic solvents. *Inorganic Chemistry* **26**, 2024-2027 (1987).

48 Jellema, R., Bulthuis, J. & Van der Zwan, G. Dielectric relaxation of

acetonitrile-water mixtures. *Journal of Molecular Liquids* **73**, 179-193 (1997).

49 Gagliardi, L. G., Castells, C. B., Rafols, C., Rosés, M. & Bosch, E. Static dielectric constants of acetonitrile/water mixtures at different temperatures and Debye-Hückel A and a_0B parameters for activity coefficients. *Journal of Chemical & Engineering Data* **52**, 1103-1107 (2007).

50 Huggins, R. A. *Advanced Batteries: Materials Science Aspects* (Springer, 2008).

51 Ottakam Thotiyl, M. M., Freunberger, S. A., Peng, Z. & Bruce, P. G. The carbon electrode in nonaqueous Li–O_2 cells. *Journal of the American Chemical Society* **135**, 494-500 (2012).

52 Itkis, D. M. *et al.* Reactivity of carbon in lithium–oxygen battery positive electrodes. *Nano Letters* **13**, 4697-4701 (2013).

53 Syty, A. Determination of sulfur dioxide by ultraviolet absorption spectrometry. *Analytical Chemistry* **45**, 1744-1747 (1973).

54 Sun, S., Niu, Y., Sun, Z., Xu, Q. & Wei, X. Solubility properties and spectral characterization of sulfur dioxide in ethylene glycol derivatives. *RSC Advances* **5**, 8706-8712 (2015).

55 Ake, R. L., Oglesby, D. M. & Kilroy, W. P. A Spectroscopic Investigation

of Lithium Dithionite and the Discharge Products of a Li/SO_2 Cell. *Journal of the Electrochemical Society* **131**, 968-974 (1984).

56 Xia, C., Black, R., Fernandes, R., Adams, B. & Nazar, L. F. The critical role of phase-transfer catalysis in aprotic sodium oxygen batteries. *Nature Chemistry* **7**, 496-501 (2015).

57 Gao, X., Chen, Y., Johnson, L. & Bruce, P. G. Promoting solution phase discharge in Li-O_2 batteries containing weakly solvating electrolyte solutions. *Nature Materials* **15**, 882-888 (2016).

58 Lim, H.-D. *et al.* The potential for long-term operation of a lithium–oxygen battery using a non-carbonate-based electrolyte. *Chemical Communications* **48**, 8374-8376 (2012).

59 Lim, H. D. *et al.* Enhanced Power and Rechargeability of a Li−O_2 Battery Based on a Hierarchical-Fibril CNT Electrode. *Advanced Materials* **25**, 1348-1352 (2013).

60 Hartmann, P. *et al.* A rechargeable room-temperature sodium superoxide (NaO_2) battery. *Nature Materials* **12**, 228-232 (2013).

61 Bender, C. L., Jache, B., Adelhelm, P. & Janek, J. Sodiated carbon: a reversible anode for sodium–oxygen batteries and route for the chemical synthesis of sodium superoxide (NaO_2). *Journal of Materials Chemistry A*

3, 20633-20641 (2015).

62 Lim, H.-D. *et al.* Rational design of redox mediators for advanced Li–O_2 batteries. *Nature Energy* **1**, 16066 (2016).

63 Liu, T. *et al.* Cycling Li-O_2 batteries via LiOH formation and decomposition. *Science* **350**, 530-533 (2015).

64 Park, M. S. *et al.* A highly reversible lithium metal anode. *Scientific Reports* **4**, 3815 (2014).

65 Choi, J. W. *et al.* Effect of various lithium salts in TEGDME based electrolyte for Li/pyrite battery. *Solid State Phenomena* **124-126**, 971-974 (2007).

66 Shui, J.-L. *et al.* Reversibility of anodic lithium in rechargeable lithium–oxygen batteries. *Nature Communications* **4**, 2255-2261 (2013).

67 Jang, I. C., Ida, S. & Ishihara, T. Lithium depletion and the rechargeability of Li–O_2 batteries in ether and carbonate electrolytes. *ChemElectroChem* **2**, 1380-1384 (2015).

68 Bieker, G., Winter, M. & Bieker, P. Electrochemical in situ investigations of SEI and dendrite formation on the lithium metal anode. *Physical Chemistry Chemical Physics* **17**, 8670-8679 (2015).

69 Abraham, K. & Chaudhri, S. The lithium surface film in the Li/SO_2 cell.

Journal of the Electrochemical Society **133**, 1307-1311 (1986).

70 Hartmann, P. *et al.* Pressure dynamics in metal–oxygen (metal–air) batteries: a case study on sodium superoxide cells. *The Journal of Physical Chemistry C* **118**, 1461-1471 (2014).

71 Burke, C. M. *et al.* Implications of 4e⁻ Oxygen Reduction via Iodide Redox Mediation in Li–O_2 Batteries. *ACS Energy Letters* **1**, 747-756 (2016).

72 Hartmann, P. *et al.* A comprehensive study on the cell chemistry of the sodium superoxide (NaO_2) battery. *Physical Chemistry Chemical Physics* **15**, 11661-11672 (2013).

Chapter 3. Developing highly durable Na-O_2 battery

3.1 Chemical and electrochemical behaviors of NaO_2 in Na–O_2 batteries

(The essence of this chapter has been published in *Nature Communications*. Reproduced with permission from [Kim, J.† and Park, H.† et al., *Nat. Commun*. **7**, 10670 (2016)] Copyright (2016) Nature Publishing Group)

3.1.1 Research Background

To address the increasing use of renewable energy and launch of electric vehicles, the need for rechargeable batteries with high energy densities has been growing more rapidly than ever before[1,2]. Among the available battery chemistries, metal–oxygen systems offer the highest energy density with the largest theoretical capacities. Unlike conventional lithium-ion batteries (LIBs), the direct reaction between oxygen and light metals such as lithium and sodium in metal–oxygen systems circumvents the need for a heavy transition metal redox couple in their operation, thereby making a high gravimetric energy density achievable[3-7]. The most intensively studied metal–oxygen system to date is the lithium–oxygen (Li–O_2) battery, which shares a similar lithium chemistry with LIBs. However, this system suffers from poor cycle stability and efficiency, which has retarded the feasibility of its use in practical systems[8,9]. In particular, the large charge overpotential over 1 V,

the main reason for the low efficiency, also accelerates the degradation of the electrode and electrolyte[9]. As an alternative, Na has been introduced to replace Li in Li–O_2 batteries with a few important merits[10]. Despite the reduction of the energy density resulting from the lower redox potential of Na/Na^+, Na resources are readily available, less expensive than Li, and can easily replace Li in the battery chemistry. It has been reported that the redox reactions in the Na–O_2 battery result in an extremely low charge overpotential (~0.2 V) despite involving the formation of micrometer-sized sodium superoxide (NaO_2) cubic crystallites[11-14]. This unique phenomenon supports the idea that this system is a promising alternative not only in terms of the cost of materials but also regarding the potential practical performance advantages.

Notably, however, the reactions of Na–O_2 cells appear to be more diverse than those of Li–O_2 cells. Contrary to the initial report of NaO_2 discharge products, some recent works could not reproduce either the formation of the discharge product NaO_2 or the low charge overpotential[15-17]. It was reported that sodium peroxide (Na_2O_2)[15-17] or sodium peroxide dihydrate ($Na_2O_2 \cdot 2H_2O$)[18,19] were formed instead. In addition, these cells exhibited high overpotential during charge, similar to that observed in the Li–O_2 system. Many groups have attempted to determine the reasons for these discrepancies; however, to date, the main cause of the divergence of reactions has not been identified. Janek *et al*. investigated the effect of different carbon electrodes; Guo *et al*. and Shao-Horn *et al*. addressed this issue but observed no critical differences among the cases[12,20,21].

In this work, we demonstrate the interplay of the diverse reactions in Na–O_2 batteries involving a series of electrochemical and chemical reactions as a function of time. Under systematic control of the operating conditions, we observe that the galvanostatic charge/discharge profiles are sensitively affected by the conditions and durations of the electrochemical operations. It is also revealed that the electrochemically formed NaO_2 is unstable and degrades into $Na_2O_2 \cdot 2H_2O$ in the absence of an applied current. The spontaneous dissolution and ionization of NaO_2 liberates the free O_2^- in the electrolyte and promotes side reactions involving the formation of $Na_2O_2 \cdot 2H_2O$. Based on these observations, we propose reaction mechanisms of Na–O_2 batteries under various operating conditions. This report is the first to reveal the relationships among the different discharge products observed in Na–O_2 batteries, which broadens our understanding of the electrochemical and chemical reactions in Na–O_2 batteries. Furthermore, these discussions may offer insight and guidance to the metal–air battery community in terms of regulating the kinetics of the intertwined reactions.

3.1.2 Experimental Method

3.1.2.1 Cell assembly and galvanostatic cycling of Na–O_2 cells

The carbon cathode was prepared by casting Ketjen Black carbon paste and polytetrafluoroethylene (PTFE) (60 wt% emersion in water, Sigma-Aldrich) with a mass ratio of 9:1 in a solution of isopropanol (IPA: >99.7%, Sigma-Aldrich) and N-methyl-2-pyrrolidone (NMP: 99.5%, anhydrous, Sigma-Aldrich) with a volume ratio of 1:1 on Ni mesh current collectors. The carbon-coated Ni mesh was dried at 120 °C and heated at 400 °C for 4 h in Ar to completely remove any residual H_2O impurities.

All the procedures described below were performed in an Ar-filled glove box (O_2 level < 0.5 ppm, H_2O level < 0.5 ppm). The Na–O_2 cells were assembled as a Swagelok-type cell with stacking of the Na metal anode, electrolyte-soaked separators, and carbon cathode, which was punched with a ½-inch diameter. The Na metal anode was carefully prepared by milling dry Na metal chunks (ACS Reagent, Sigma-Aldrich) after removing the contaminated surfaces. The electrolyte was prepared with diethylene glycol dimethyl ether (DEGDME, anhydrous, 99.5%, Sigma-Aldrich), which contains 0.5 M $NaCF_3SO_3$ (98%, Sigma-Aldrich). The solvent was dried using 3-Å molecular sieves for over one week, and the salt was also kept in a vacuum oven at 180 °C for the same time before use. The final water content in the electrolyte was less than 10 ppm according to a Karl-Fisher titration measurement. The amount of electrolyte used for the cell was 200 μL. Two sheets of Celgard 2400 were used as separators. Electrochemical battery tests of the Na–O_2

cells were conducted using a potentio-galvanostat (WonA Tech, WBCS 3000, Korea). All the cells were relaxed under 770 torr of O_2 pressure for 10 min before the tests. After being saturated with O_2 gas, the cells were operated in the closed state with a limited capacity of 1 mAh, lower voltage cutoff of 1.6 V, and upper voltage cutoff of 4.2 V. Special protocol based on a pulsed current was applied during the charge to avoid dendritic failure of the Na metal anode. The on/off time ratio of the pulse charge was 1:4 (applying current for 0.5 s and relaxing for 2 s). More details about our charge protocol are provided in Figure 3.1 and following discussions in Supplementary Note 3.1.

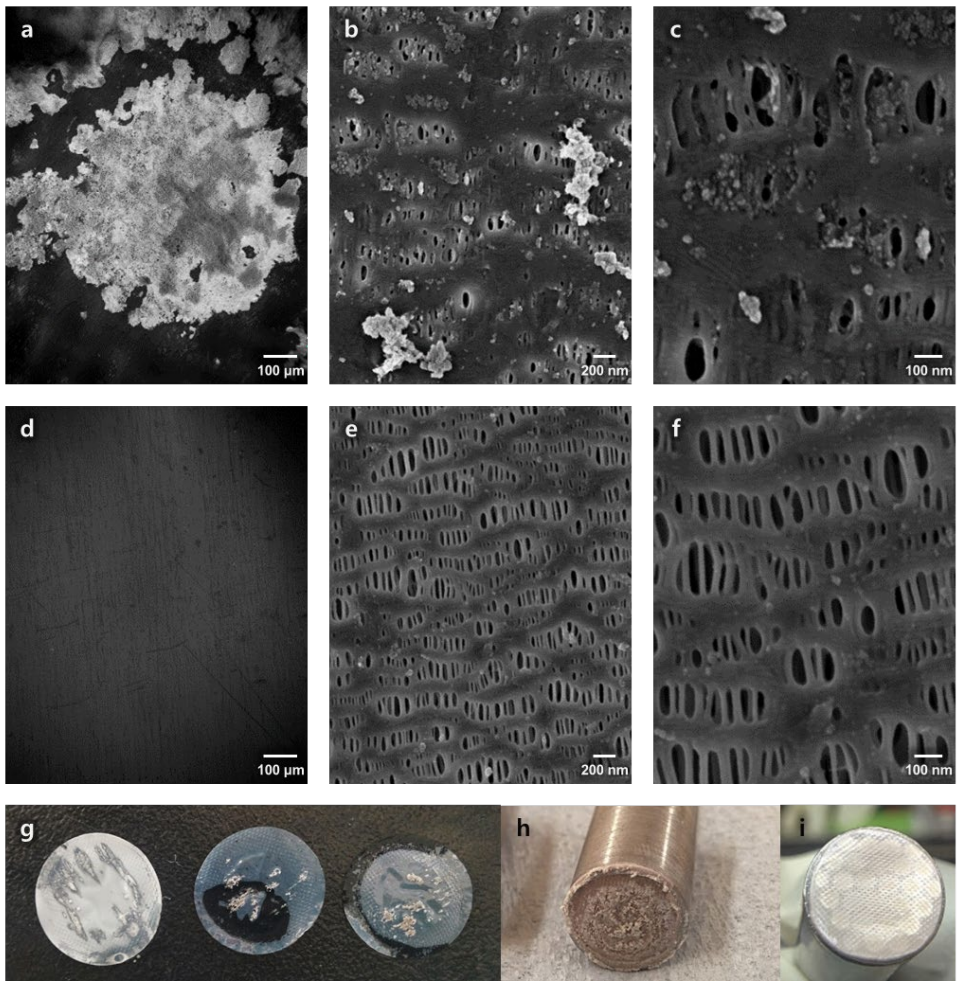

Figure 3.1. SEM images and photographs of Na dendrites after the cycling of Na–O_2 cells. (a–c) SEM images of Na dendrites after the cycling of Na–O_2 cells using direct currents; (d–f) pulse currents during the charge process. (g) Photographs of Na dendrites on the separators after cycling; (h) Na anode with the direct current. (i) surface of Na anode for the pulsed current.

Supplementary Note 3.1

In our galvanostatic cycling experiments of Na–O_2 cells, the dendritic failure of the Na metal anode was frequently observed during the charge process. The SEM images of the separators collected after cycling with the direct currents are presented in Figure. 3.1a–c, which reveal that the Na metal clogged and penetrated the pores of the separators, resulting in the dendritic growth of the Na metal and failure of the cells. The Na dendrites were visually inspected, as shown in the photographs of the separators and anodes in Figure. 3.1g. These dendrites were critically damaged during the cycling process, resulting in short circuits and potential failures. To suppress and avoid the dendritic growth of Na metal, we applied special operating protocols based on pulse-charging, which is a common methodology in electroplating and deposition. Under these conditions, the stable electrochemical cycling of Na–O_2 cells without any voltage fluctuations or sudden drops was possible. The SEM images in Figure. 3.1d–f also demonstrate the absence of dendritic Na metal penetrating or clogging the pores of the separators. In addition, the upper surface of the pulse-charged Na metal in Figure. 3.1i is seemingly much cleaner than that of the direct-current-charged Na metal.

3.1.2.2 Characterization of Na–O_2 cells

The discharged cathodes after the different rest times were collected from disassembled Na–O_2 cells and washed with acetonitrile (anhydrous, 99.8%, Sigma-Aldrich) in a glove box to remove any residual electrolyte. X-ray diffraction (XRD) spectra of the cathodes were obtained using a Bruker D2-Phaser (Cu Kα λ=1.5406 Å) with the aid of a specially designed air-tight holder to prevent outer atmospheric contamination. Raman spectra were obtained using a Horiba Jobin-Yvon LabRam Aramis spectrometer (the 514 nm line of an Ar-ion laser was used as the excitation source). The scattered light of the Raman signal was collected in a backscattering geometry using the x50 microscope objective lens. Field-emission scanning electron microscopy (FE-SEM, MERLIN Compact, ZEISS, Germany) was used for the morphological observations after Pt coating. For electron spin resonance (ESR) characterization, the collected powder from the discharged cathodes after rinsing to remove the residual used electrolytes was soaked in fresh electrolyte. After immersing the powdery discharged cathodes, the ESR signal of the electrolytes was measured at room temperature using a JEOL JES-TE200 ESR spectrometer every 10 min for 12 h using a liquid quartz-cell. The microwave X-band frequency was 9.42 GHz at 1-mW power.

3.1.2.3 Theoretical calculations of solvation energy

First-principles calculations were performed using the spin-polarized generalized gradient approximation (GGA). A continuum solvation model (VASPsol[22,23] code) was used to evaluate the solvation energy of the alkali-metal superoxide/peroxide (M_xO_2, M: Li, Na, x = 1 or 2). The following equations were used considering both the (1) molecular and (2) ionized solvated states:

$$\Delta E_{\text{sol, mol}} = E_{\text{solvated}}(M_xO_2) - E_{\text{bulk}}(M_xO_2) \quad (1)$$

$$\Delta E_{\text{sol, ion}} = x \cdot E_{\text{solvated}}\left(M^{+}\right) + E_{\text{solvated}}(O_2^{x-}) - E_{\text{bulk}}(M_xO_2), \quad (2)$$

where $E_{\text{solvated}}(M_xO_2)$ and $E_{\text{bulk}}(M_xO_2)$ are the total energies of the solvated and bulk M_xO_2 per formula unit, respectively. The solvated species (ions or molecules) were placed in a 13 Å × 13 Å × 13 Å cell as an isolated species. We used the plane-wave basis with an energy cut-off of 550 eV and a Monkhorst–Pack 2×2×2 *k*-point mesh. Based on previous reports[24,25] that stated that the solvation entropy term (TS) of polar molecules and ions in the standard state is less than 5% of the enthalpy term (H), we neglected the entropy effect of the solvation in these calculations.

3.1.3 Results and Discussions

3.1.3.1 Electrochemical profile of Na–O_2 batteries

To address the previous conflicting results on the discharge products and overpotentials of Na–O_2 cells, we carefully assessed the effects of operating parameters on the resulting electrochemical profiles. We observed that the charge/discharge profiles were most sensitively affected by the applied current and rest time between the discharge and charge, which was analogous to the report by Yadegari *et al*. as a function of discharge current or limited capacities[19]. Figure 3.2 presents and compares the electrochemical profiles obtained under various conditions. Although the discharge profiles are similar, with a single plateau at ~2.1 V, there are roughly three different charging plateaus observed at (i) ~2.5 V, (ii) ~3.0 V, and (iii) 3.8 V, which agree with recent reports under certain settings[19,20]. However, the relative lengths of each plateau markedly vary under differing operating conditions. For the cases of controlled discharge currents followed by a constant current charging in Figure 3.2a, it was observed that the length of the lower plateau (~2.5 V) in the charge profiles was reduced as the applied discharge current decreased from 0.5 to 0.02 mA. However, the lengths of the plateaus at higher voltages, *i.e.,* ~3.0 and 3.8 V, were substantially increased, resulting in an overall larger overpotential. Similar behaviors were observed in Figure 3.2b when varying the charge currents after a constant current discharge. With the lower applied charge currents, the cell exhibited a higher charging overpotential with shortened plateau

length at 2.5 V. This result contrasts with the general observation that slow charging/discharging of electrochemical cells results in a voltage close to the equilibrium potential, thereby resulting in smaller overpotentials. In addition, this result strongly indicates that the different discharge products might undergo the charging process at each case. Notably, the shapes of the electrochemical charge profiles provide important clues to determine the discharge products of Na–O_2 reactions[19,26]. Even though the discharge products should be identical for the cases of the same protocol of discharge, each charge profile was distinct with different charge currents. This finding implies that the initial discharge products are gradually transformed into other phases during the charge process *via* time-dependent reactions. To verify whether this transformation occurs *via* an electrochemical or chemical reaction, we also controlled the rest time between the discharge and charge processes. As observed in Figure 3.2c, the lowest voltage region in the charge profiles systematically decreases upon increasing the rest time from 0 to 12 h. The change in the electrochemical profile in the absence of the applied current clearly indicates that the time-dependent chemical reactions occurred during the rest period, affecting the subsequent charging. This behavior was also confirmed in similar tests for the higher charging currents with the resting time after the discharge, which revealed the growth of the charge polarizations upon increasing the rest time (Figure 3.3).

The time-dependent chemical reactions can be more clearly visualized by plotting all the voltage profiles as a function of the time. Fig. 3.2d–j illustrate the

voltage evolution of each cell after the completion of the discharge at different operating conditions. The first inflection points of the voltage profiles at charge (indicated with arrows) occur at approximately 10 h regardless of the rest or charge protocols. This result indicates that a specific time of ~10 h is required before observing a change of the profile, which hints at the kinetics of the chemical reactions.

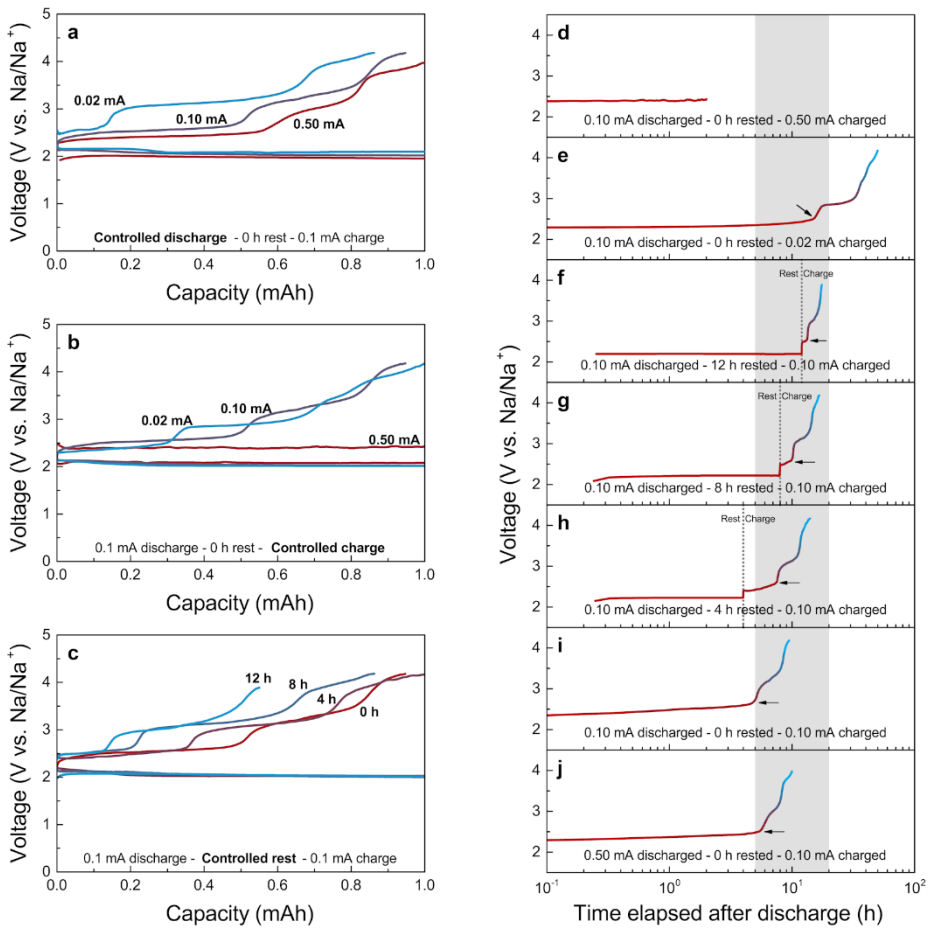

Figure 3.2. Electrochemical charge/discharge profiles of Na–O_2 cells under various operating conditions. (a) Discharge currents of 0.02, 0.1, and 0.5 mA; (b) rest times of 0, 4, 8, and 12 h; and (c) charge currents of 0.02, 0.1, and 0.5 mA. All the cells utilized a limited capacity of 1.0 mAh. (d–j) Representations of voltage profiles as a function of time corresponding to (a–c). The shaded area indicates that range of the first points of the polarized charge potentials.

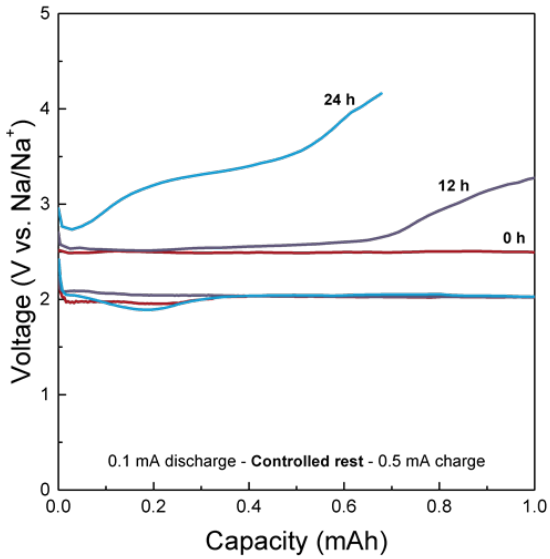

Figure 3.3. Electrochemical characteristics of Na–O_2 cells under high charge currents combined with rest time.

3.1.3.2 Time-resolved characterization of discharge products

To confirm the time-dependent phase transformation of the discharge products *via* chemical reaction in Na–O_2 cells, we characterized the discharge products in air electrodes as a function of the rest time. The highly crystalline NaO_2 was observed directly after the discharge with no other phases, as demonstrated in the X-ray diffraction (XRD) spectra (Figure 3.4a–b)[11]. However, after being aged for several hours, the NaO_2 peak slowly diminished, whereas the characteristic peak of $Na_2O_2 \cdot 2H_2O$ began to appear and grew. After 12 h of resting, the initial discharge product was completely transformed into $Na_2O_2 \cdot 2H_2O$. It should be noted that $Na_2O_2 \cdot 2H_2O$ has often been regarded as a main discharge product in previous reports of Na–O_2 batteries[18-20]. Recently, Ortiz-Vitoriano *et al*. reported that NaO_2 could convert to $Na_2O_2 \cdot 2H_2O$ upon exposure to the ambient air during the characterization at room temperature[21]. However, our data show that such transformation occurs in the electrochemical cells by the intrinsic dissolving characteristics of NaO_2 in the electrolyte even without the exposure to the ambient atmosphere. Remarkably, the time taken for the discharge product to completely transform into $Na_2O_2 \cdot 2H_2O$ coincides with the timeline of Figure 3.2d–j, which shows the inflection of the voltage rising after approximately 10 h. When we analyzed the phases of the discharge products as a function of the applied discharge currents (Figure 3.5), it was also observed that the NaO_2/$Na_2O_2 \cdot 2H_2O$ ratio decreased with the lower operating

current, which is consistent with the time-dependent transformation of the discharge products.

Raman spectroscopy results confirmed that the initial NaO_2 discharge products gradually transformed into $Na_2O_2{\cdot}2H_2O$ with resting. In Figure 3.4c, the two distinct peaks of NaO_2 and $Na_2O_2{\cdot}2H_2O$ are detected along with the characteristic bands (D/G) of the carbon electrode. The Raman signals at 1156 and 1136 cm^{-1} are attributed to the O–O stretch bonding in NaO_2 and $Na_2O_2{\cdot}2H_2O$, respectively[21]. The systematic change in the relative ratios of NaO_2 and $Na_2O_2{\cdot}2H_2O$ with time is clearly illustrated in Figure 3.4d, which agrees well with the results in Figure 3.4b. The phase transition of NaO_2 to proton-containing $Na_2O_2{\cdot}2H_2O$ indicates a source of protons in the electrochemical cell. Considering the low water content in the electrolyte used for the cell (< ~5 ppm), which is insufficient to form the phase[21,27,28], the protons are likely delivered from other sources such as the electrolyte solvent. As we could expect, the rechargeability of Na-O_2 cell was better for the highly biased electrochemical conditions coupled with the low polarized charge profile (Figure 3.6), which is attributed to the electrochemical formation and decomposition of NaO_2 as shown in Figure 3.7. However, the electrochemical reversibility with the 3-steped charge profile shown from $Na_2O_2{\cdot}2H_2O$ was relatively worse compared to the former conditions. The proposed transformation mechanism will be discussed in detail later.

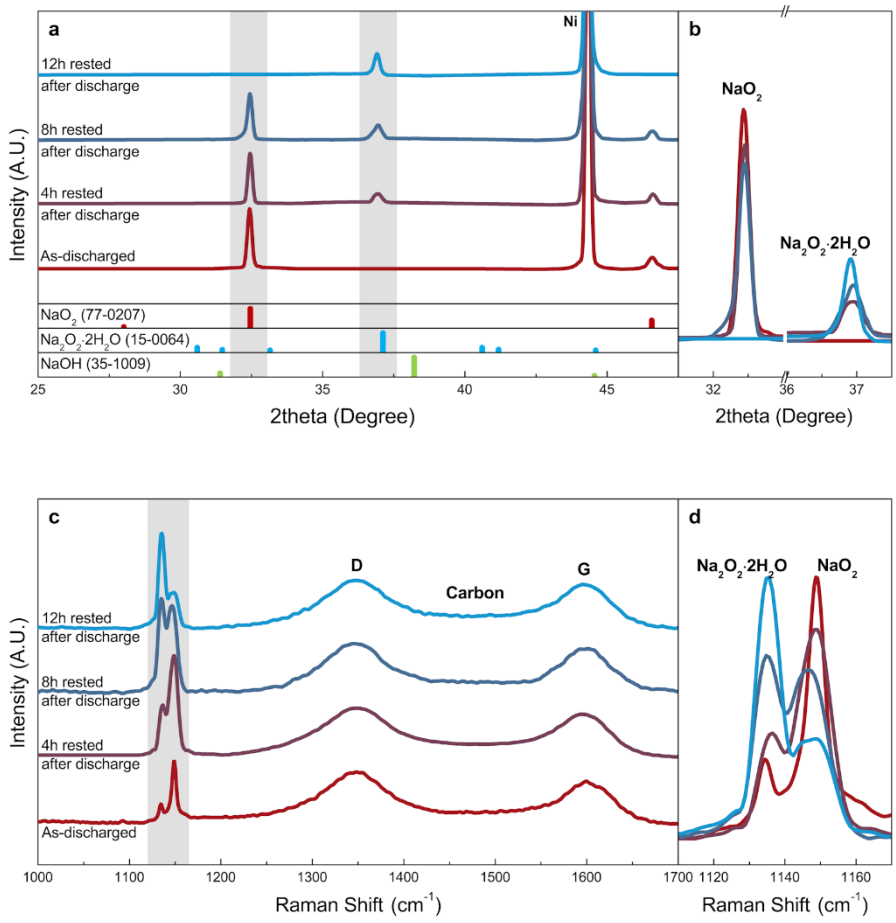

Figure 3.4. Time-resolved characterization showing the phase transitions of the discharge products of the Na–O_2 cells. (a,b) XRD spectra of the discharged cathodes of Na–O_2 batteries with rest times of 0, 4, 8, and 12 h. (c,d) Raman spectra of the discharged cathodes of Na–O_2 batteries with rest times of 0, 4, 8, and 12 h.

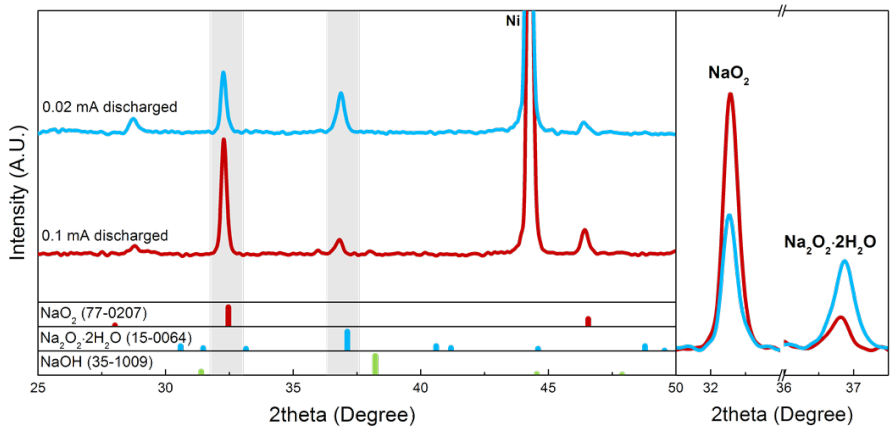

Figure 3.5. XRD spectra of the discharged cathodes of Na–O_2 cells for different discharge currents with the full discharge capacity of 4 mAh. XRD analysis clearly demonstrates that a larger amount of NaO_2 transformed into $Na_2O_2{\cdot}2H_2O$ during the discharge at the relatively smaller current of 0.02 mA because of the longer time exposure to the electrolyte.

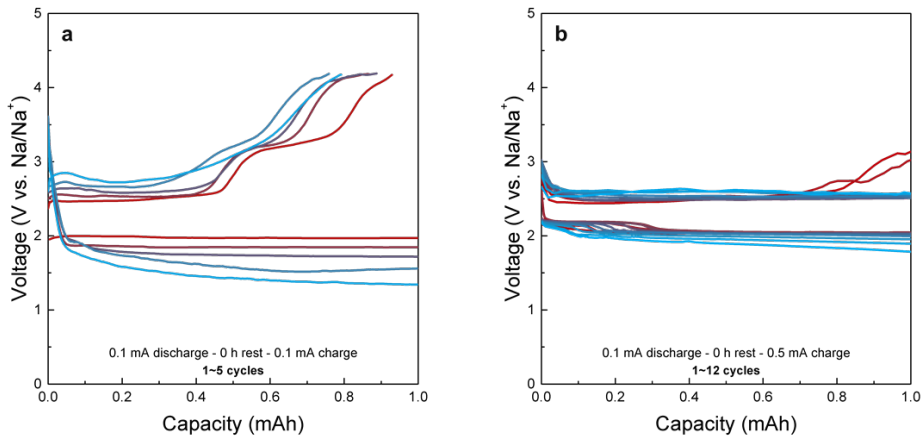

Figure 3.6. Electrochemical characteristics of Na–O_2 cells with the different voltage profiles over several cycles. (a) Cycling up to 5 cycles with a charge current of 0.1 mA involving clear 3-step charge profiles. (b) Cycling up to 12 cycles with the charge current of 0.5 mA involving the lower flat charge profiles.

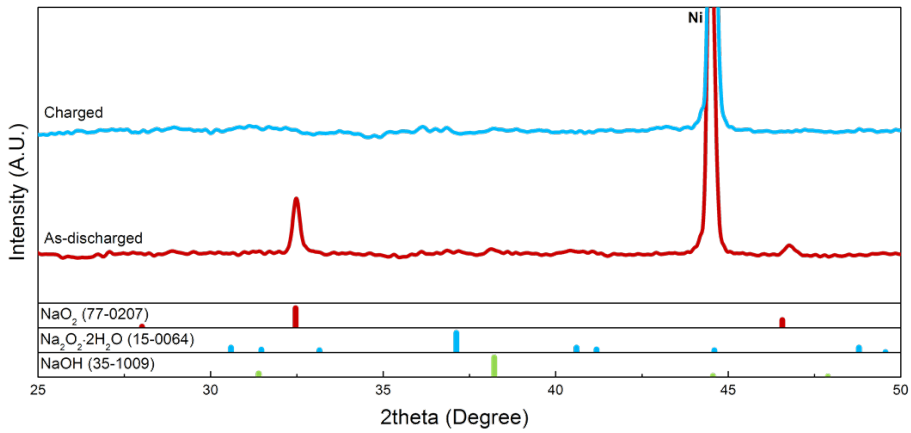

Figure 3.7. XRD analysis of the formation and decomposition of NaO_2 after the discharge and charge.

3.1.3.3 Morphological change of discharge products over time

To visualize the transition process, we examined the morphologies of the discharge products at different rest times within 12 h. In Figure 3.8a, well-defined micron-sized cubic NaO_2 was observed immediately after the discharge, which agrees with the observation of Hartmann *et al.*[11] However, the edges of the cubes became significantly dull, and the overall shapes of the cubes obtained were smudged during the rest period (Figure 3.8b–c). At the end of the rest period, the cubic crystallites completely disappeared, and rod-shaped microparticles began to appear, which resemble the $Na_2O_2{\cdot}2H_2O$ in a previous report[19]. This morphological change suggests the disappearance of NaO_2 and the subsequent appearance of $Na_2O_2{\cdot}2H_2O$ in the cell during the rest period. Moreover, this finding implies that the transformation does not occur *via* a conventional solid-state or interfacial reaction between NaO_2 and the electrolyte to form $Na_2O_2{\cdot}2H_2O$, which would not involve significant morphological change. Rather, it is likely to be a solution-mediated process through dissolution and nucleation[29-31].

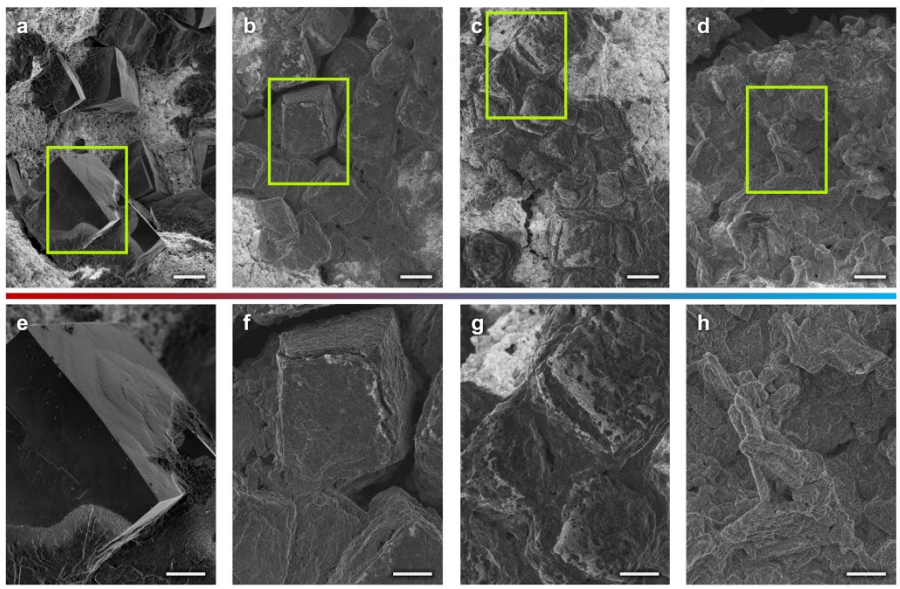

Figure 3.8. Time-resolved examinations of the morphology of discharge products on the cathodes of Na–O_2 cells. (a-d) Morphology of the discharge products of Na–O_2 cells (scale bar = 10 μm). (e-h) Corresponding magnified SEM micrographs (scale bar, 5 μm); (a,e) as-discharged, (b,f) 4-h rest after discharge, (c,g) 8-h rest after discharge, and (d,h) 12-h rest after discharge.

3.1.3.4 Dissolution and ionization of NaO_2

We investigated the possibility of the dissolution of the solid NaO_2 phase in the electrolyte using electron spin resonance (ESR) spectroscopy, which is useful for detecting the magnetic responses of the unpaired electrons in radicals such as O_2^-[32]. Surprisingly, as observed in Figure 3.9a, with the simple immersion of the pre-discharged cathodes, the ESR signal evolved within 10 min from the fresh electrolyte, indicating the presence of O_2^-. To avoid any effect of the remaining oxygen from the disassembled Na–O_2 cells, the pre-discharged cathodes were washed with fresh electrolyte before the measurement, which led to an identical result. The calculated *g*-value of 2.0023 for the observed ESR signal corresponds well with the theoretical value of the unpaired electron in free O_2^-[33]. The solubility of NaO_2 in the electrolyte was roughly estimated about 187 mM, which is in the similar order with the report by Schechter *et al*.[34], but has a relatively large discrepancy to the report by Hartmann *et al*[35]. This discrepancy might be mainly due to the additional chemical reactions involving the precipitation of solid $Na_2O_2 \cdot 2H_2O$. The detection of O_2^- indicates that the NaO_2 is soluble in the ether-based electrolytes, which was also expected from the literatures with the electrochemical determinations[21,28,35]. Furthermore, this behavior is analogous to highly soluble LiO_2 in the solvatable conditions of Li–O_2 batteries[27,36]. More importantly, the dissolution can immediately lead to the ionization of NaO_2, liberating O_2^-, the consequences of which will be discussed later.

Figure 3.9b shows that the peak-widths of the ESR signals increased slightly with time. The broadening indicates the energy exchange of the spin with the local environments *via* spin–spin relaxation or spin–lattice relaxation[32]. This interaction supports the time-dependent chemical reactions associated with the dissolved O_2^- with its neighboring electrolyte solvent. The intensity of the O_2^- signal is the highest approximately 20 min after the immersion and exponentially decreases over time, indicating the instability of O_2^- in the electrolyte[37]. From this behavior, we could derive that it was a pseudo-first order reaction which mainly relates with the concentration of O_2^-. Based on the exponential fitting of the relative intensity of ESR signals, the pseudo-first order rate constant of H^+-abstraction was obtained as about $k' \approx 0.560$, and its corresponding half-life was estimated as about $t_{1/2} = \ln(2) / k' \approx 1.24$ h, the detailed derivation is in Supplementary Note 3.2. Figure 3.9c reveals, however, that the time-dependent decay of the intensity is relatively sluggish compared with the intrinsic lifetime of normal O_2^-. Typically, the half-life of O_2^- is approximately 1–15 min because of its high reactivity and instability[38]. The abnormally long half-life in the electrolyte (~1.24 h) in our case is believed to occur because O_2^- is continuously generated with the dissolution of NaO_2. The ESR signal completely vanished after approximately 8 h, which is slightly faster than the time required for the formation of $Na_2O_2 \cdot 2H_2O$ in Figure 3.4. Despite the evolution of O_2^-, the overall signal decay might be induced from the relatively dominant H^+-abstraction due to the reactivity of O_2^-. This gap in the kinetics might originate from the time required to form the $Na_2O_2 \cdot 2H_2O$ phase from the O_2^-.

To understand the dissolution and ionization behavior of NaO_2, the solvation energies of various alkali metal superoxides and peroxides were calculated for comparison using first-principle calculations with the series of dielectric constant from 7~30. Figure 3.9d reveals that generally, the superoxide exhibits a lower solvation energy than the peroxide for both lithium and sodium compounds. This result is consistent with our result of NaO_2 dissolution and the recent experimental findings for Li–O_2 batteries, which indicated that LiO_2 is found mostly as soluble intermediates in the electrolyte in contrast to the solid phase of Li_2O_2[27,36]. In addition, it is notable that the solvation energy of the sodium phases was significantly lower than that of the lithium phases, which is attributed to the weaker Lewis acidity of the Na cation compared with that of the Li cation in the polar solvent[39,40]. However, for the solvents with substantially lower dielectric constant (ε = ~ 7), the dissolution is unfavorable even in NaO_2. Molecular dissolution energies of NaO_2 in model solvents are ~0.6 eV, which roughly corresponds to 1 molecule dissolution among 10^{10} formula units of NaO_2. On the other hand, it markedly diminishes to 0.17 eV (1 molecule among 10^3 formula units of NaO_2) in ε = 30. Note that for the low dielectric constant solvents, dielectric constant of the solution sensitively increases with containing higher salt concentration, which can result in higher solution dielectric constant than that of the pure solvent[41]. Therefore, it is expected that the dissolution of NaO_2 can occur when salts are present in the electrolyte, which is consistent with the observation of O_2^- in the ESR analysis. It is noted that even with the dissolving characteristics of NaO_2, the crystallization of NaO_2 is possible in the normal

discharging conditions with the supersaturation of localized reactants such as Na^+ and O_2^- [21,35,42,43]. In the other case where the supply of the reactants such as Na^+ are limited, for example, in the absence of the applied voltage, the dissolution and ionization might dominate giving rise to the formation of $Na_2O_2 \cdot 2H_2O$ as a discharge product.

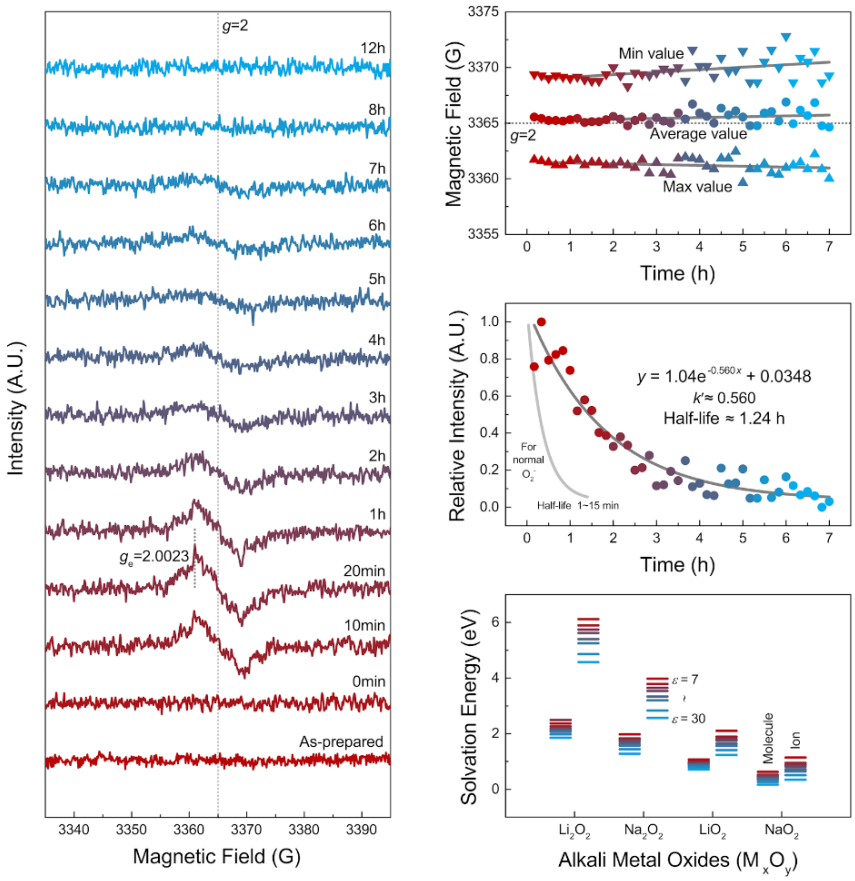

Figure 3.9. ESR analysis and theoretical calculations of the dissolution and ionization of NaO_2 into the electrolyte. (a) Time-dependent ESR measurements for the fresh electrolytes (0.5 M $NaCF_3SO_3$ in DEGDME) with soaking of the pre-discharged cathode without any aging. (b) Maximum, minimum, and average values of ESR signals as a function of time. (c) Exponential decay of ESR signals and the common trend line of O_2^-. (d) Calculations of the solvation energy for several alkali-metal superoxides and peroxides with the various dielectric constants (ε = 7~30).

Supplementary Note 3.2

In principle, the ESR reaction in Figure 3.9a–c was a second-order reaction which is determined by the concentrations of two reactants such as O_2^- and the electrolyte solvent. As we investigated, the electrolyte solvent might be decomposed by nucleophilic attack of O_2^-. However, the concentrations of both reactants differentiated simultaneously, so it is rather challenging to exactly determine the reaction rate of the second-order. Nevertheless, the concentration of electrolyte solvent molecule was relatively excessive enough compared to that of O_2^-, so we could approximately ignore the concentration difference of solvent. Then, we can estimate this reaction as a pseudo-first order reaction. The reaction rate of H^+-abstraction can be expressed as

$$r = -\mathrm{d}[HO_2]/\mathrm{d}t = k[H_{(HA)^+}][O_2^-] = k'[O_2^-],\ k' = k[H_{(HA)^+}]$$

Based on the exponential fitting of the relative intensity of ESR signals, the pseudo-first order rate constant of H^+-abstraction was obtained as about $k' \approx 0.560$, and its corresponding half-life was estimated as about $t_{1/2} = \ln(2) / k' \approx 1.24$ h.

3.1.3.5 Proposed mechanism of Na–O_2 batteries

Based on the previous reports and our new findings, we propose a mechanism that describes the electrochemical and chemical reactions in Na–O_2 systems in Figure 3.10. The well-established discharge process[11] can be illustrated with the reduction of an O_2 molecule into O_2^-, which reacts with Na^+ to form NaO_2 (Reaction 1), and the charge process is the reverse reaction (Reaction 2). After or during the discharge, the NaO_2 is prone to dissolution and ionization into the electrolyte based on the solvating energy (ΔG_{sol}) in the solvent (Reaction 3)[36]. The dissolution of NaO_2 generates O_2^-, which can degrade the surrounding molecules because of its chemical instability. Typically, the liberated O_2^- is a strong reagent for the abstraction of H^+ from the electrolyte solvents (Reaction 4)[9], and the degree of H^+ abstraction[44,45] is determined by the acid-dissociation constant (pK_a) of the solvent. Some hydroperoxyl radicals (HO_2) might be formed during this process, resulting in the nucleophilic attack of the H^+-lost solvent (Reaction 5)[46]. However, the evolution of HO_2 can be helpful to promote the solution-mediated discharge/charge process as recently reported by Xia *et al.*[28]. Nevertheless, in a circumstance where the dissolution/ionization of NaO_2 is dominant, the liberation of O_2^- is overwhelmingly larger than a possible HO_2 formation inducing the H^+-abstraction from the neighboring electrolyte solvent. Meanwhile, the solvent undergoes oxidative decompositions to produce byproducts such as carbon dioxide (CO_2), water (H_2O), and hydroxyl anions (OH^-) (Reaction 6)[9]. It is also possible that

the coupling of HO_2 leads to disproportionation into hydrogen peroxide (H_2O_2) and O_2 (Reaction 7)[47]. In the presence of both Na^+ and OH^-, which is effectively the dissolution state of sodium hydroxide (NaOH), a solid crystallite of NaOH can precipitate with a higher concentration of OH^- produced. Further reaction between NaOH and H_2O_2 from Reaction 7 leads to the formation of $Na_2O_2 \cdot 2H_2O$ *via* peroxo-hydroxylation, whose reverse reaction is well known (Reaction 8)[48]. In order to support our proposed reaction mechanism, we chose several intermediate reactions which should be verified according to the reaction model. Figure 3.11 and Figure 3.12 demonstrate that O_2^- plays an important role after the dissolution of NaO_2 in converting the discharge product to $Na_2O_2 \cdot 2H_2O$ *via* degradation of the electrolyte involving OH^- and H_2O_2. These identifications strongly support the proposed mechanism of competing electrochemical and following chemical reactions in Na–O_2 batteries. The detailed discussions are provided in Supplementary Note 3.3. The reaction equations are summarized below:

Discharge/Charge:	$Na^+ + O_2 + e^- \leftrightarrow NaO_2$	(1)
Dissolution/Ionization:	$NaO_2 \rightarrow Na^+ + O_2^-$	(2)
Proton abstraction:	$HA + O_2^- \rightarrow A^- + HO_2$	(3)
Disproportionation:	$2\ HO_2 \rightarrow H_2O_2 + O_2$	(4)
Oxidative decomposition:	$A^- + HO_2 \rightarrow CO_2, H_2O, OH^-$	(5)
Peroxo-hydroxylation:	$2\ Na^+ + 2\ OH^- + H_2O_2 \rightarrow Na_2O_2 \cdot 2H_2O$	(6)

It is noteworthy that a similar behavior has been recently reported for reactions in Li–O_2 batteries. The solvating environment was demonstrated to alter the stability of the intermediates, such as a lithium superoxide (LiO_2), thus affecting the overall reaction paths[27,36]. LiO_2 is a precedent phase with the direct reaction of a Li cation and superoxide anion (O_2^-), which readily decomposes into lithium peroxide (Li_2O_2) *via* either an electrochemical surface reaction or disproportionation[27,36]. Although LiO_2 is known to be unstable[49,50], it was recently demonstrated that LiO_2 might be dissolved into the electrolyte and aid in the formation of the toroidal Li_2O_2 *via* a solution reaction under highly solvating conditions[27]. NaO_2 shares this dissolving nature with LiO_2 even though the thermodynamic stability of NaO_2 warrants its formation as a discharge product. The significant dissolution of NaO_2 supports the conclusion that the dominant reaction in Na–O_2 batteries relies on the solution-mediated reactions of nucleation and growth of NaO_2[21,28,35] and implies that the capacities and morphology of the reaction products would be greatly affected by the energetics of NaO_2 under various conditions (such as different electrolytes and current rates). This is also supplemented with the recently reported observations[21,35] and operating mechanism[28] in terms of the various states of electrochemical and chemical reactions.

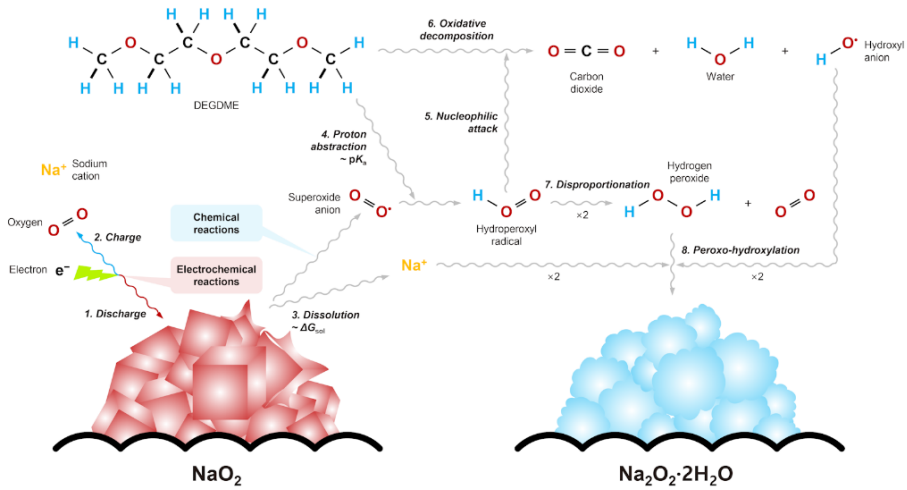

Figure 3.10. Schematic of the proposed mechanism illustrating the electrochemical and chemical reactions under various operating conditions. For the electrochemical reaction, NaO_2 is formed and decomposed during discharge/charge (Reaction 1, 2). For the chemical reaction, NaO_2 is dissolved and ionized into the electrolyte (Reaction 3), which promotes the undesired degradation of the electrolyte (Reaction 4–6). $Na_2O_2·2H_2O$ is formed during the subsequent chemical reactions (Reactions 7, 8).

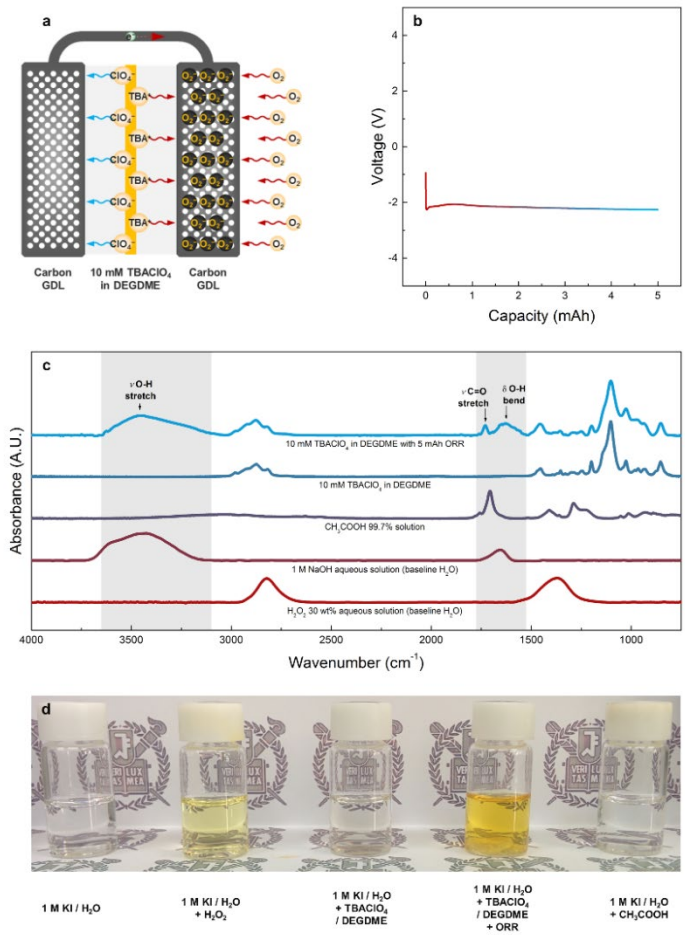

Figure 3.11. (a) Symmetric cell configuration to generate O_2^-. The electrolyte was used with 10 mM $TBAClO_4$ in DEGDME and the electrode was used with commercial carbon GDL. (b) The electrochemical profile of simulated ORR experiment with the symmetric cell. The applied current was 0.1 mA and the controlled capacity was 5 mAh. (c) FTIR spectra and (d) Iodometric determinations of the electrolyte with simulated ORR.

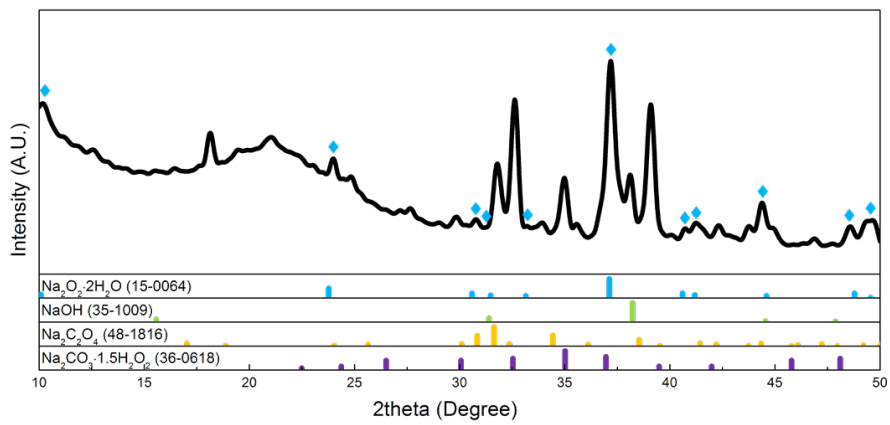

Figure 3.12. XRD pattern of the chemically synthesized $Na_2O_2 \cdot 2H_2O$ according to the proposed mechanism. All the synthesis and characterizations were carried out in the Ar-filled glovebox.

Supplementary Note 3.3

To experimentally simulate Reaction 4-6 in Figure 3.10, firstly, we generated O_2^- in the electrolyte composed with 10 mM $TBAClO_4$ in DEGDME in the symmetric cell as shown in Figure 3.11a and Figure 3.11b. The simulated coulomb was 5 mAh, which is 5-fold excess amount of electrochemically formed NaO_2 with the discharge. If we exclude the shuttle effect during the discharge, the concentration of O_2^- is approximately 0.93 M compared to the volume of injected electrolyte (200 μl).

After allowing the relaxation of O_2^- generated in the presence of the electrolyte, the electrolyte was examined by FTIR in Figure 3.11c to identify the chemical reactions triggered by O_2^-. As compared to the as-prepared electrolyte, it was observed that the broad peak at about 3400 cm^{-1} evolves, which corresponds to νO–H stretch. This indicates the formation of free OH^- with the chemical reaction of O_2^- with the electrolyte. Furthermore, it was found that a small δO–H band and νC=O stretch at around 1625 cm^{-1} and 1728 cm^{-1}, respectively. The former signal also corresponds to the formation of the free OH^-, and the latter could be attributed to the trace amount of carboxylic functional groups (–COOH) in the byproduct. The presence of H_2O_2 was difficult to confirm from the FTIR due to the overlaps of signatures with DEGDME. The identification of νO–H, δO–H, νC=O band in the electrolyte strongly support the Reaction 6.

We carried out the iodometric determinations to supplement the FTIR results above and verify the presence of H_2O_2 as shown in Figure 3.11d. When the electrolyte exposed to O_2^- was added to the basis of 1 M KI aqueous solutions, which were initially transparent, the color of the solution was immediately changed to yellow. It indicates the oxidation of iodide ion (I^-) to triiodide ion (I_3^-), which was induced by the presence of H_2O_2 *via* the reacttion ($2\ I^- + 2\ H^+ + H_2O_2 \rightarrow I_3^- + 2\ H_2O$). Rest of the chemical additives such as as-prepared electrolyte or CH_3COOH do not change the color of the iodide solution. This observation supports that H_2O_2 was formed after the chemical reactions coupled with ORR, and validates Reaction 7.

On the basis of byproducts from Reaction 6 and 7, we attempted to simulate the formation of $Na_2O_2{\cdot}2H_2O$ as proposed in Reaction 8 ($2\ NaOH + H_2O_2 \rightarrow Na_2O_2{\cdot}2H_2O$). 0.5 M H_2O_2 aqueous solution was added dropwise to the anhydrous ethanol solution of 1 M NaOH. Because NaOH is insoluble in ether-based solvents, the solvent was used with the anhydrous ethanol to reproduce the effectively dissolved state of NaOH. After the mixing, it was found that the white precipitates were immediately formed. The retrieved precipitates were examined by XRD after drying under vacuum for 30 min. Figure 3.12 identifies that the main phase of precipitates were $Na_2O_2{\cdot}2H_2O$ with a trace amount of other phases that might be formed during the process. The formation of $Na_2O_2{\cdot}2H_2O$ strongly supports the proposed Reaction 8.

3.1.4 Concluding Remarks

We successfully demonstrated the interplay of the diverse competing reactions in Na–O_2 batteries. The time-dependent chemical reactions were identified as being triggered from the dissolution and ionization of the electrochemically formed NaO_2 in the electrolyte. The liberated O_2^- reacts with the electrolyte solvent to form $Na_2O_2 \cdot 2H_2O$ following a series of intermediate steps. The $Na_2O_2 \cdot 2H_2O$ in the air electrode requires a higher energy for the decomposition, which leads to the increased charge overpotential and irreversibility of Na–O_2 cells. This report is the first to correlate the electrochemical and chemical reactions with the operating conditions in Na–O_2 batteries, and our findings concerning the relationships among different phases resolve the conflicting observations of different discharge products in previous Na–O_2 batteries. To prepare a better performing Na–O_2 battery, a strategy to prevent the transformation of NaO_2 into $Na_2O_2 \cdot 2H_2O$ while still allowing the solution-mediate discharge reaction is necessary. We hope that the findings of this study can provide a basis for researchers to navigate and direct the reactions in Na–O_2 batteries to achieve high efficiency and rechargeability.

3.1.5 References

1 Tarascon, J. M. & Armand, M. Issues and challenges facing rechargeable lithium batteries. *Nature* **414**, 359-367 (2001).

2 Kang, K., Meng, Y. S., Bréger, J., Grey, C. P. & Ceder, G. Electrodes with High Power and High Capacity for Rechargeable Lithium Batteries. *Science* **311**, 977-980 (2006).

3 Abraham, K. M. & Jiang, Z. A Polymer Electrolyte-Based Rechargeable Lithium/Oxygen Battery. *Journal of the Electrochemical Society* **143**, 1-5 (1996).

4 Bruce, P. G., Freunberger, S. A., Hardwick, L. J. & Tarascon, J.-M. Li-O_2 and Li-S batteries with high energy storage. *Nature Materials* **11**, 19-29 (2012).

5 Peng, Z., Freunberger, S. A., Chen, Y. & Bruce, P. G. A Reversible and Higher-Rate Li-O_2 Battery. *Science* **337**, 563-566 (2012).

6 Ottakam Thotiyl, M. M. *et al.* A stable cathode for the aprotic Li–O_2 battery. *Nature Materials* **12**, 1050-1056 (2013).

7 Lim, H.-D. *et al.* Superior Rechargeability and Efficiency of Lithium–Oxygen Batteries: Hierarchical Air Electrode Architecture Combined with a Soluble Catalyst. *Angewandte Chemie-International Edition* **126**, 4007-4012 (2014).

8 Débart, A., Paterson, A. J., Bao, J. & Bruce, P. G. α-MnO_2 Nanowires: A

Catalyst for the O_2 Electrode in Rechargeable Lithium Batteries. *Angewandte Chemie-International Edition* **47**, 4521-4524 (2008).

9 Freunberger, S. A. *et al.* The Lithium–Oxygen Battery with Ether-Based Electrolytes. *Angewandte Chemie-International Edition* **50**, 8609-8613 (2011).

10 Yabuuchi, N., Kubota, K., Dahbi, M. & Komaba, S. Research Development on Sodium-Ion Batteries. *Chemical Reviews* **114**, 11636-11682 (2014).

11 Hartmann, P. *et al.* A rechargeable room-temperature sodium superoxide (NaO_2) battery. *Nature Materials* **12**, 228-232 (2013).

12 Bender, C. L., Hartmann, P., Vračar, M., Adelhelm, P. & Janek, J. On the Thermodynamics, the Role of the Carbon Cathode, and the Cycle Life of the Sodium Superoxide (NaO_2) Battery. *Advanced Energy Materials* **4**, 1301863 (2014).

13 McCloskey, B. D., Garcia, J. M. & Luntz, A. C. Chemical and Electrochemical Differences in Nonaqueous Li–O_2 and Na–O_2 Batteries. *The Journal of Physical Chemistry Letters* **5**, 1230-1235 (2014).

14 Hartmann, P. *et al.* Pressure Dynamics in Metal–Oxygen (Metal–Air) Batteries: A Case Study on Sodium Superoxide Cells. *The Journal of Physical Chemistry C* **118**, 1461-1471 (2014).

15 Liu, W., Sun, Q., Yang, Y., Xie, J.-Y. & Fu, Z.-W. An enhanced electrochemical performance of a sodium-air battery with graphene nanosheets as air electrode catalysts. *Chemical Communications* **49**, 1951-

1953 (2013).

16 Li, Y. *et al.* Superior catalytic activity of nitrogen-doped graphene cathodes for high energy capacity sodium-air batteries. *Chemical Communications* **49**, 11731-11733 (2013).

17 Hu, Y. *et al.* Porous perovskite calcium-manganese oxide microspheres as an efficient catalyst for rechargeable sodium-oxygen batteries. *Journal of Materials Chemistry A* **3**, 3320-3324 (2015).

18 Kim, J., Lim, H.-D., Gwon, H. & Kang, K. Sodium-oxygen batteries with alkyl-carbonate and ether based electrolytes. *Physical Chemistry Chemical Physics* **15**, 3623-3629 (2013).

19 Yadegari, H. *et al.* On rechargeability and reaction kinetics of sodium-air batteries. *Energy & Environmental Science* **7**, 3747-3757 (2014).

20 Zhao, N., Li, C. & Guo, X. Long-life Na-O_2 batteries with high energy efficiency enabled by electrochemically splitting NaO_2 at a low overpotential. *Physical Chemistry Chemical Physics* **16**, 15646-15652 (2014).

21 Ortiz-Vitoriano, N. *et al.* Rate-Dependent Nucleation and Growth of NaO_2 in Na–O_2 Batteries. *The Journal of Physical Chemistry Letters* **6**, 2636-2643 (2015).

22 Fishman, M., Zhuang, H. L., Mathew, K., Dirschka, W. & Hennig, R. G. Accuracy of exchange-correlation functionals and effect of solvation on the surface energy of copper. *Physical Review B* **87**, 245402 (2013).

23 Mathew, K., Sundararaman, R., Letchworth-Weaver, K., Arias, T. A. & Hennig, R. G. Implicit solvation model for density-functional study of nanocrystal surfaces and reaction pathways. *The Journal of Chemical Physics* **140**, 084106 (2014).

24 Burgess, J. Metal ions in Solution. *Chichester: Horwood Ellis: New York* (1978).

25 Ben-Amotz, D., Raineri, F. O. & Stell, G. Solvation Thermodynamics: Theory and Applications. *Journal of Physical Chemistry B* **109**, 6866-6878 (2005).

26 Yadegari, H. *et al.* Three-Dimensional Nanostructured Air Electrode for Sodium–Oxygen Batteries: A Mechanism Study toward the Cyclability of the Cell. *Chemistry of Materials* **27**, 3040-3047 (2015).

27 Aetukuri, N. B. *et al.* Solvating additives drive solution-mediated electrochemistry and enhance toroid growth in non-aqueous Li–O_2 batteries. *Nature Chemistry* **7**, 50-56 (2015).

28 Xia, C., Black, R., Fernandes, R., Adams, B. & Nazar, L. F. The critical role of phase-transfer catalysis in aprotic sodium-oxygen batteries. *Nature Chemistry* **7**, 496-501 (2015).

29 Schroeder, M. A. *et al.* DMSO–Li_2O_2 Interface in the Rechargeable Li–O_2 Battery Cathode: Theoretical and Experimental Perspectives on Stability. *ACS Applied Materials & Interfaces* **7**, 11402-11411 (2015).

30 Kumar, N., Radin, M. D., Wood, B. C., Ogitsu, T. & Siegel, D. J. Surface-

Mediated Solvent Decomposition in Li–Air Batteries: Impact of Peroxide and Superoxide Surface Terminations. *The Journal of Physical Chemistry C* **119**, 9050-9060 (2015).

31 Kwabi, D. G. *et al.* Chemical Instability of Dimethyl Sulfoxide in Lithium–Air Batteries. *The Journal of Physical Chemistry Letters* **5**, 2850-2856 (2014).

32 Wang, Q., Yang, X.-Q. & Qu, D. In situ ESR spectro-electrochemical investigation of the superoxide anion radical during the electrochemical O_2 reduction reaction in aprotic electrolyte. *Carbon* **61**, 336-341 (2013).

33 Eastland, G. W. & Symons, M. C. Electron spin resonance studies of superoxide ions produced by radiolysis in alcoholic media. *The Journal of Physical Chemistry* **81**, 1502-1504 (1977).

34 Schechter, D. L. & Kleinberg, J. Reactions of Some Metal Salts with Alkali Superoxides in Liquid Ammonia. *Journal of the American Chemical Society* **76**, 3297-3300 (1954).

35 Hartmann, P. *et al.* Discharge and Charge Reaction Paths in Sodium–Oxygen Batteries: Does NaO_2 Form by Direct Electrochemical Growth or by Precipitation from Solution? *The Journal of Physical Chemistry C* **119**, 22778-22786 (2015).

36 Johnson, L. *et al.* The role of LiO_2 solubility in O_2 reduction in aprotic solvents and its consequences for Li–O_2 batteries. *Nature Chemistry* **6**, 1091-1099 (2014).

37 Hall, P. & Selinger, B. Better estimates of exponential decay parameters. *The Journal of Physical Chemistry* **85**, 2941-2946 (1981).

38 Maricle, D. L. & Hodgson, W. G. Reducion of Oxygen to Superoxide Anion in Aprotic Solvents. *Analytical Chemistry* **37**, 1562-1565 (1965).

39 Okoshi, M., Yamada, Y., Yamada, A. & Nakai, H. Theoretical Analysis on De-Solvation of Lithium, Sodium, and Magnesium Cations to Organic Electrolyte Solvents. *Journal of the Electrochemical Society* **160**, A2160-A2165 (2013).

40 Ziegler, M. & Madura, J. Solvation of Metal Cations in Non-aqueous Liquids. *Journal of Solution Chemistry* **40**, 1383-1398 (2011).

41 Petrowsky, M. A. *Ion transport in liquid electrolytes* Ph. D thesis, University of Oklahoma, (2008).

42 Kashchiev, D. & Van Rosmalen, G. Review: nucleation in solutions revisited. *Crystal Research and Technology* **38**, 555-574 (2003).

43 Takiyama, H. Supersaturation operation for quality control of crystalline particles in solution crystallization. *Advanced Powder Technology* **23**, 273-278 (2012).

44 Khetan, A., Pitsch, H. & Viswanathan, V. Solvent Degradation in Nonaqueous Li-O_2 Batteries: Oxidative Stability versus H-Abstraction. *The Journal of Physical Chemistry Letters* **5**, 2419-2424 (2014).

45 Khetan, A., Luntz, A. & Viswanathan, V. Trade-Offs in Capacity and Rechargeability in Nonaqueous Li–O_2 Batteries: Solution-Driven Growth

versus Nucleophilic Stability. *The Journal of Physical Chemistry Letters* **6**, 1254-1259 (2015).

46 Sawyer, D. T. & Valentine, J. S. How super is superoxide? *Accounts of Chemical Research* **14**, 393-400 (1981).

47 Chin, D. H., Chiericato, G., Nanni, E. J. & Sawyer, D. T. Proton-induced disproportionation of superoxide ion in aprotic media. *Journal of the American Chemical Society* **104**, 1296-1299 (1982).

48 Hill, G. S. *et al.* The X-ray structure of a sodium peroxide hydrate, $Na_2O_2 \cdot 8H_2O$, and its reactions with carbon dioxide: relevance to the brightening of mechanical pulps. *Canadian Journal of Chemistry* **75**, 46-51 (1997).

49 Zhai, D. *et al.* Raman Evidence for Late Stage Disproportionation in a Li–O_2 Battery. *The Journal of Physical Chemistry Letters* **5**, 2705-2710 (2014).

50 Zhai, D. *et al.* Interfacial Effects on Lithium Superoxide Disproportionation in Li-O_2 Batteries. *Nano Letters* **15**, 1041-1046 (2015).

3.2 Highly durable and stable NaO_2 in concentrated electrolytes for Na–O_2 batteries

(The essence of this chapter has been published in Advanced Energy Materia ls. Reproduced with permission from [Park, H. *et al., Adv. Energy Mater*. **2 018**, 8, 1801760] Copyright (2018) WILEY-VCH)

3.2.1 Research Background

Since the first report of rechargeable sodium–oxygen batteries by Hartmann *et al.* in 2012, these systems have attracted great attention because they exhibit the highest theoretical energy density (~1100 Wh kg^{-1} based on NaO_2 as a discharge product) among available sodium rechargeable battery chemistries while also offering the advantages of elemental earth abundance and potential cost efficiency.[1] In particular, their intrinsically high energy efficiency and reversibility make sodium–oxygen batteries strong candidates for next-generation rechargeable batteries.[1,2] Unlike lithium–oxygen batteries, for which a peroxide phase is commonly formed as the main discharge product rather than a superoxide phase[3], the thermodynamic stability of sodium superoxide and its facile dissociation enable its reversible formation as a main product in sodium–oxygen batteries.[1,2,4-7] The promising electrochemical properties of sodium–oxygen batteries have been attributed to the formation of sodium superoxide, which exhibits substantial solubility in electrolytes and thus drives solution-based

reactions as a dominant pathway. The finding of a proton as a phase-transfer catalyst[8] and the critical role of electrolyte solvation in the discharge process[9] also strongly support the dominant solution reaction mechanisms in sodium–oxygen batteries, which have been confirmed by experimental evidence of soluble superoxide species[7,10,11] and the low solvation energy of the sodium superoxide estimated in a previous computational study.[12] These intrinsic solution chemistries enable the achievement of high capacity and low polarization for sodium–oxygen batteries without the need for redox mediators or soluble catalysts, which are believed to be necessary for the development of highly reversible lithium–oxygen[13-19] or lithium–gas (SO_2, CO_2…)[20-22] batteries.

Despite the thermodynamic stability of sodium superoxide in sodium–oxygen batteries, recent studies have reported the chemical instability of sodium superoxide in ether-based electrolytes, in which undesirable self-decomposition occurs. In our previous study, time-resolved characterizations revealed that sodium superoxide transforms into byproducts, mainly sodium peroxide dihydrate ($Na_2O_2 \cdot 2H_2O$), within 12 h of exposure to diethylene glycol dimethyl ether (DEGDME) electrolytes; we proposed the idea that the side reactions were triggered by spontaneous dissolution of sodium superoxide and subsequent proton abstraction of the electrolytes by the superoxide anion.[7] Shao-horn *et al.* also observed an identical phase transition from sodium superoxide to sodium peroxide dihydrate within a few days in DME electrolytes.[23,24] In addition, recent work by Sun *et al.* showed the consistent change of the discharge product within a similar

time scale (~13 h) based on in-line X-ray diffraction measurements.[25] Slightly different reaction pathways have also been suggested, including the formation of sodium peroxide octahydrate ($Na_2O_2 \cdot 8H_2O$) reported by Nazar *et al.*[26] and superoxide (O_2^-) migration reported by Janek *et al*.[27] There are minor discrepancies in the details of the observations and proposed reactions in previous studies, partly due to the variations in the cell configurations and experimental conditions, which are summarized in Table 3.1. However, all the aforementioned studies consistently raised the issue of the chemical stability of sodium superoxide in sodium–oxygen batteries. Byproducts other than sodium superoxide require higher polarization to be recharged, and their decomposition reactions have not been shown to involve reversible oxygen evolution, which subsequently leads to serious degradation of the efficiency and reversibility of the batteries.[27] These phenomena should be closely linked to the storage properties or shelf-life of the batteries, as the remarkable shelf-life of potassium–oxygen batteries resulting from the high stability of potassium superoxide in ethereal electrolytes was recently reported.[28] Despite sharing similar electrochemistry between sodium– and potassium–oxygen batteries, the potassium superoxide is robust against the spontaneous disproportionation to peroxide unlike sodium superoxide, enabling markedly long shelf-life of potassium–oxygen battery as 30 days. The detrimental effects of storage after discharge in sodium–oxygen batteries may be amplified for the batteries used in electric vehicles (EVs) as EVs may not always be immediately recharged. Therefore, appropriate strategies to overcome the sodium

superoxide stability issue are indispensable for the future development of sodium–oxygen batteries.

We previously reported that the parasitic reactions are triggered by the dissolution of sodium superoxide, followed by subsequent proton abstraction of electrolytes by the superoxide anion.[7] Dissolution of a solid material in a liquid medium involves a solvating process and is mainly governed by the solvating capability of the free solvent molecules to break the internal bonding of the solid material.[29-32] In this respect, the elimination of free solvents in electrolytes can effectively stabilize the solid materials by decreasing the probability for interactions with free solvents.[33-35] Recently, it was successfully demonstrated that super-concentrated electrolytes without free solvents can effectively suppress the dissolution of polysulfides in lithium–sulfur batteries.[35-37] Additionally, it was observed that the full pairing of solvents with solutes can also remarkably improve the chemical and electrochemical stabilities of the solvents.[38-42] This finding resulted in the realization of a new class of electrolytes that can even use an aqueous solvent in a high-voltage battery or lithium/sodium metal battery systems, which are now categorized as "water-in-salt" or "solvent-in-salt" electrolytes.[35,38,39,43-46]. We decided, herein, to explore the use of these high-concentration electrolytes to suppress the parasitic reactions promoted by the dissolution of sodium superoxide in sodium–oxygen batteries. The solvation structures of the electrolytes are systematically examined with controlled salt concentrations using Raman

spectroscopy, infrared spectroscopy, and nuclear magnetic resonance spectroscopy. We find that the physicochemical properties of the electrolytes are drastically altered, and consequently, sodium superoxide is stably maintained with five-times-longer lifetime in concentrated electrolytes than in conventional electrolytes. Finally, we apply the high-concentration electrolytes in sodium–oxygen batteries and demonstrate that the energy efficiency and cell reversibility are well conserved even with a resting period of 1 day every cycle. This study is the first to successfully improve the chemical stability and lifetime of sodium superoxide by simple tuning of the electrolyte in sodium–oxygen batteries. This discovery is complementary to the previous understanding of the solution chemistry of sodium–oxygen batteries, highlighting the importance of the role of electrolytes in the metal–oxygen chemistry.

Table 3.1. Summary of experimental details, proposed reaction pathway, and characterization methods used in previous studies on the instability of sodium superoxide.

Research Group	Paper	Cell configuration		Resting time scale	Proposed reaction pathway	Characterization
		Cathode	Electrolyte			
K. Kang	*Nat. Commun.* (2016.02)	Ketjen black	0.5 M $NaCF_3SO_3$ in DEGDME (200 µL)	0 -12 hours	NaO_2 → $Na_2O_2{\cdot}2H_2O$	Voltage profiles, XRD, Raman, SEM…
L. F. Nazar	*ChemSusChem* (2016.06)	^{13}C carbon	0.5 M $NaCF_3SO_3$ in DEGDME (240 µL)	100 hours	NaO_2 → $Na_2O_2{\cdot}8H_2O$ + NaC_xO_y…	Iodometry titration, XRD, SEM, ^1H NMR
Y. Shao-Horn	*Chem. Commun.* (2016.07)	CNTs	0.1 M $NaClO_4$ in DEGDME (200 µL)	0 - 20 days	NaO_2 → $Na_2O_2{\cdot}2H_2O$	Voltage profiles, XRD, SEM…
J. Janek & T. Rojo	*ACS Appl. Mater. Interfaces* (2016.07)	GDL paper	0.5 M $NaCF_3SO_3$ in DEGDME (100 µL)	0 - 48 hours	NaO_2 → O_2^- & Superoxide migration	Voltage profiles, SEM, Raman, FTIR, Pressure monitoring…
C. P. Grey	*J. Phys. Chem. Lett.* (2016.11)	rGO	0.25 M $NaClO_4$ in DME (0.7 mL)	15 days	NaO_2 → Na_2O_2-like phase + NaC_xO_y	Solid-state ^{23}Na NMR
X. Sun	*J. Phys. Chem. Lett.* (2017.09)	Hydrophobic carbon cloth (Heat treat at Ar/H_2)	0.5 M $NaCF_3SO_3$ in DEGDME (200 µL)	0 -13 hours	NaO_2 → $Na_2O_2{\cdot}2H_2O$	XRD

3.2.2 Experimental Method

3.2.2.1 Materials and cell assembly

Sodium perchlorate ($NaClO_4$, anhydrous, 98.0%–102.0%) was purchased from Alfa Aesar, and diethylene glycol dimethyl ether (DEGDME, anhydrous, 99.5%) was purchased from Sigma Aldrich. The salt was used as received, and the solvent was dried using activated molecular sieves (3 Å) for 1 week before use. The final water content of all the electrolytes was approximately 30 ppm based on Karl Fisher titration measurements. The sodium metal electrode was prepared by rolling a sodium cube (Na, contains mineral oil, 99.9%) into a sheet after removing the contaminated surface. Avcarb P50 carbon paper was obtained from Fuel Cell Earth and dried at 120 °C for 24 h before use. Both the sodium metal electrode and P50 carbon electrode were punched in a 1/2-inch diameter. The sodium–oxygen cell was assembled in the sequence of a sodium metal electrode, separators soaked with electrolytes, and a P50 carbon electrode using a Swagelok-type cell in an Ar-filled glove box (O_2 level <0.1 ppm and H_2O level <0.1 ppm). The amount of electrolyte for the cell was 200 μL. Two sheets of QM-A grade glass fiber were used as a separator for the cell. All the assembled sodium–oxygen cells were stored under flowing O_2 atmosphere at 1.5 bar pressure for 5 min. Before the cell tests, all the cells were stabilized with relaxation of 30 min and operated in the closed state. Deep discharge property of the cells using P50 carbon electrodes with such dimension is presented in Figure 3.13 for a precise and fair comparison of electrochemical

properties. A coin-type CR2032 cell was assembled in the same sequence, particularly for DEMS with pressure monitoring tests. The amount of electrolyte usef for a coin-type CR2032 cell was 100 μL. For the sodium symmetric cell tests, a coin-type cell CR2032 was assembled with ½-inch diameter sodium foils as both the counter and working electrode and two slices of QM-A grade glass fiber separator soaked with the electrolytes.

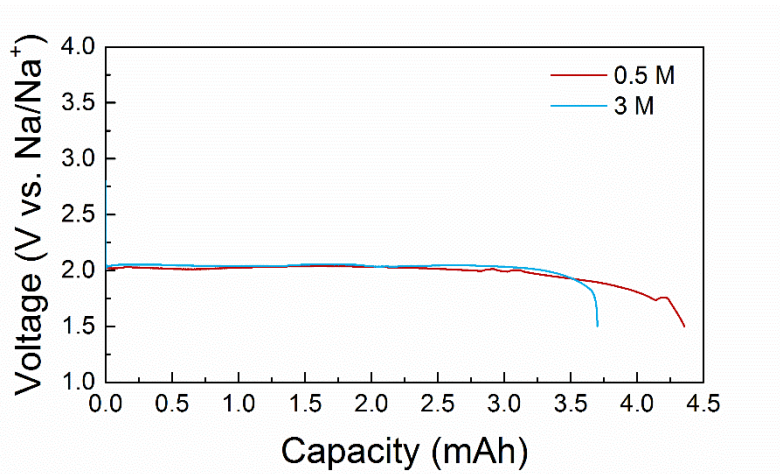

Figure 3.13. Deep discharge profiles of sodium–oxygen battery using electrolytes with different concentration. The cell with 0.5 M electrolyte (red line) could deliver approximately 4.4 mAh discharge capacity at absolute current of 0.1 mA, which corresponds to the areal capacity of 3.47 mAh/cm^2, whereas slightly lower capacity of 3.7 mAh (2.93 mAh/cm^2) was obtained for that with 3 M electrolyte (blue line).

3.2.2.2 Characterization of Na–O_2 cells

All the electrochemical tests for the sodium–oxygen cells were performed using a potentio-galvanostat (WonA Tech, WBCS 3000, Korea) between 1.5 and 3.0 V at room temperature. A DEMS instrument combined with a BioLogic SP-300 potentio-galvanostat (Knoxville, TN), a pressure transducer (Omega Engineering Inc., PX419, Stamford, CT), and a mass spectrometer (Stanford Research System, RGA200, Sunnyvale, CA) were used for the gas analyses and pressure monitoring.[47-49] During discharge, the DEMS cell was operated in a closed state filled with O_2 gas while connected to the pressure transducer. During charge, the DEMS cell was open to the mass spectrometer chamber and swept by Ar carrier gas. Electrochemical impedance measurements were performed using a potentio-galvanostat (VSP-300, Bio-Logic Science Instruments, France) at room temperature with a frequency range from 200 kHz to 50 mHz. An X-ray diffractometer (Bruker D2 Phaser) with Cu-Kα radiation (λ=1.5406 Å), field-emission scanning electron microscope (MERLIN Compact, ZEISS, Germany), and Raman spectrometer (LabRAM HV Evolution, HORIBA, Japan) were used for discharge product characterizations. To simulate the storage circumstances within the cell environments, we used the same amount (~200 μL) of electrolytes for every storage experiment. Residual electrolytes on the electrodes were washed by distilled 1,2-dimethoxyethane (DME, anhydrous, 99.5%., Sigma Aldrich) before characterizations. XRD and Raman spectra of the electrodes were recorded

under an Ar atmosphere with the aid of air-blocking holders. For structural characterization of the electrolytes, Raman spectra were obtained using a capillary tube. A Fourier-transform infrared spectrometer (FT-IR-4200, JASCO, Japan) equipped with an attenuated total reflectance (ATR) accessory was used to investigate the chemical bonding nature of the electrolytes. ^{23}Na NMR spectra were recorded using an NMR spectrometer (Avance 600, Bruker, Germany) at room temperature using a liquid NMR tube. NMR spectra were measured at a ^{23}Na frequency of 158.7 MHz with an accumulation of 256 transients, and the repetition time of each sample was set to 1.45 s (acquisition time of 0.45 s and relaxation delay of 1 s) for complete relaxation. All the chemical shifts of ^{23}Na NMR spectra were referenced to a standard solution of 1 M NaCl aqueous solution. The electrolyte properties were measured using a viscometer (SV-10, A&D Company Ltd. Japan) and a waterproof portable conductivity meter (Model CON 610, Oakton, Singapore) at 20 °C.

3.2.3 Results and Discussions

3.2.3.1 Chemical instability of NaO_2 on electrochemistry

We scrutinized the electrochemical charging responses of sodium–oxygen batteries with systematic variations of storage times after discharge to confirm the chemical stability of sodium superoxide in electrolytes for sodium–oxygen batteries. The applied current and discharge capacity in the present study were set to 0.1 mA and 0.25 mAh, respectively, with a cut-off voltage of 3.0 V (*vs.* Na/Na^+).[50,51] The storage time was controlled from 6 to 24 h after discharge. Figure 3.14a presents subsequent charge profiles of sodium–oxygen cells after the respective storage times. Typical voltage profiles were obtained for charging the cell without any pauses, in agreement with reports in the literature[1,4,7,8], showing a single plateau at 2.4 V, which corresponds to the electrochemical decomposition of sodium superoxide followed by a rapid voltage increase at the end of charge (top panel in Figure 3.14a). Approximately 80% of the capacity was reversibly charged with a small polarization (~ 200 mV) within the voltage window. With increasing storage time, however, the reversible charge capacity gradually decreased to 50% (6 h), 40% (12 h), 20% (18 h), and 15% (24 h), which is consistent with the observations in previous reports.[7,24,27] This finding strongly suggests that certain chemical events occur within the cells during storage and that these events affect the nature of the discharged product, sodium superoxide. A higher voltage limit for the charge process (~4 V) produced similar results, indicating that the deliverable charge capacity is systematically reduced with a larger polarization as the resting time

increases, as shown in Figure 3.15. This finding confirms the detrimental effect of aging/storage of a sodium–oxygen cell on its efficiency and reversibility.

Differential electrochemical mass spectroscopy (DEMS) with pressure monitoring was used to assess the oxygen efficiency during charging of cells with different storage periods to examine the reversibility of the sodium–oxygen reaction in each case. The shortest storage time was 3 h after discharge because there was a minimum required processing time for gas exchange from oxygen to argon in our DEMS system. Figure 3.14b–e show the pressure variations of oxygen gas during discharge (3.14b and 3.14d) and present gas evolution profiles during charge (3.14c and 3.14e) for two representative cases of cells stored for 3 and 24 h, respectively. Figure 3.14b shows that the oxygen consumption rate for the entire discharge process nearly coincides to the ideal e/O_2 ratio of 1.00, which means that the one-electron reaction of sodium superoxide formation occurred in the cell. During the charge process of the 3-h-storage cell in Figure 3.14c, the oxygen efficiency was also close to 1.00 e/O_2, particularly at the 2.4-V plateau; however, it significantly deviated from the ideal value during the charge process at a voltage above 3 V, with carbon dioxide and hydrogen being detected.[8,27] The overall oxygen evolution/consumption efficiency (OER/ORR) was 66% for the 3-h-rested cell; the details are summarized in Table 3.2. It is worth mentioning that the charge capacity obtained above 3 V is mainly attributed to the irreversible reaction, and, correspondingly, the reduction of the length of the 2.4-V plateau accompanies the decrease in the oxygen efficiency. Figure 3.14e shows that the evolution of oxygen gas markedly decreased for the 24-h-rested cell and that a

significantly reduced charge capacity was delivered below 3 V, even though a similar oxygen consumption rate was observed for the discharge process in Figure 3.14d. The oxygen efficiency for the cell stored for 24 h was measured to be only 25%. The strong correlation between the reversible charge capacity and measured oxygen efficiency indicates that the charging reaction beyond 3 V likely results from the electrochemical decomposition of byproducts rather than of sodium superoxide. In addition, this correlation also suggests that the detrimental effect of resting on the cell reversibility originates from the instability of sodium superoxide, the evidence of which will be provided in detail later.

The electrochemical impedance spectroscopy (EIS) spectra in Figure 3.14f illustrate that the cell impedance gradually increased during storage after discharge, which is consistent with the larger charging overpotentials for cells with longer rest periods observed in Figure 3.14a. The initial impedance of the sodium–oxygen cell was 2,500 Ω; however, it simply increased to 3,200 and 4,500 Ω with 12-h and 24-h resting, respectively. Based on our previous work, we believe that this increase can be attributed to the formation of sodium peroxide dihydrate and corresponding byproducts from electrolyte degradation; the insulating nature of this product increases the cell impedance.[7] The detrimental effects of aging on the cell impedance also affected the cycle stabilities. Figure 3.14g shows that without any pause between discharge and charge, consecutive cycling of the cells for up to approximately 80 times could be performed under a limited capacity of 0.25 mAh; however, by inserting a 12-h storage time after every discharge, the cell reversibility notably deteriorated. The inferior cycle

performance of only approximately 30% compared with that the reference cell highlights the seriously reduced cell reversibility and poor shelf-life of sodium–oxygen cells.

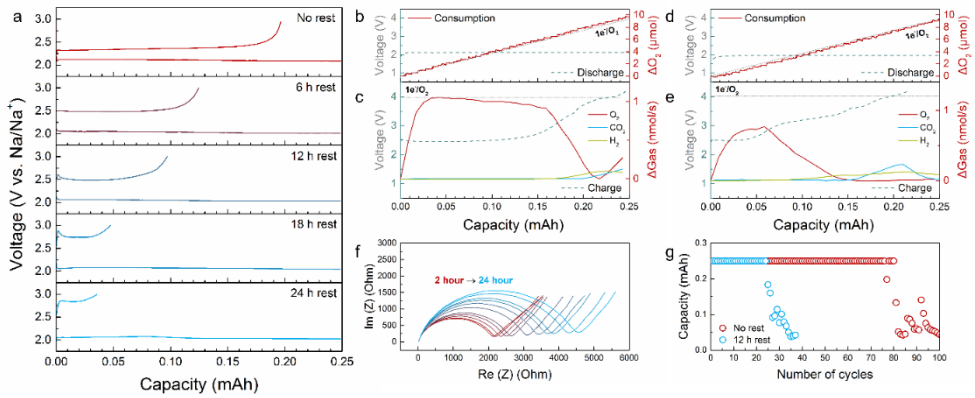

Figure 3.14. Detrimental effect of resting periods on the electrochemical properties of sodium–oxygen cells with conventional electrolytes. (a) Charge/discharge profiles of sodium–oxygen cells with various resting times from 6 to 24 h after discharge. (b) Pressure monitoring during discharge and (c) real-time gas profiles during charge of sodium–oxygen cells stored for 3 h. (d) Pressure monitoring during discharge and (e) real-time gas profiles during charge of sodium–oxygen cells stored for 24 h. The dotted lines are voltage profiles. (f) Electrochemical impedance spectra of discharged sodium–oxygen cells during storage for 24 h. (g) Capacity retention of sodium–oxygen cells with and without resting periods.

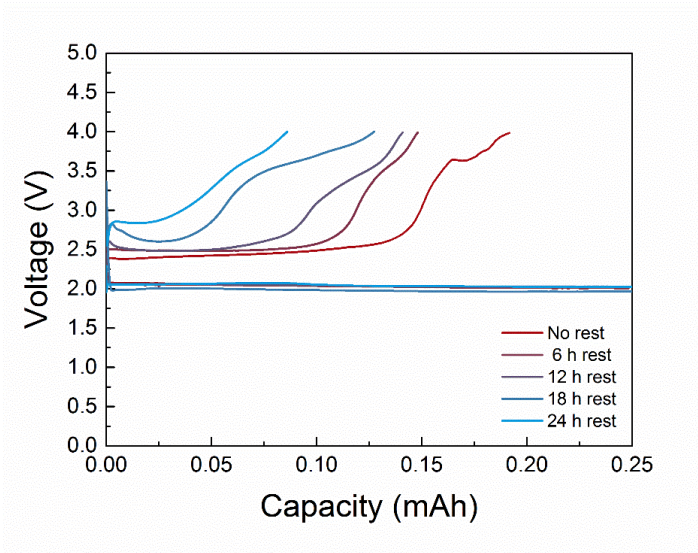

Figure 3.15. Electrochemical profiles of sodium–oxygen batteries containing 0.5 M electrolytes as a function of storage time up to 48 h with an upper voltage cut-off of 4 V.

Table 3.2. Detailed values used for calculating the oxygen efficiency from pressure monitoring and DEMS results.

Electrolyte	Storage time	$O_{2\,(th)}$ [µmol]	O_2 Consumption [µmol]	ORR	O_2 Evolution [µmol]	OER	OER/ORR (%)
0.5 mol dm^{-3}	3 hours	9.32	9.72	1.04	6.36	0.681	65.5
	24 hours	9.32	9.30	0.998	2.30	0.246	24.7
3 mol dm-^{3}	3 hours	9.32	9.13	0.980	6.49	0.697	71.1
	24 hours	9.32	9.52	1.02	6.06	0.651	63.7

3.2.3.2 Physicochemical properties of concentrated electrolytes

In our attempt to enhance the stability of sodium superoxide by exploiting high-concentration electrolytes, the nature of concentrated electrolytes was first examined to obtain information on the solvation structures and presence of free solvents in electrolytes as a function of concentration. Sodium perchlorate ($NaClO_4$) was selected as a model Na^+ conducting salt because of its sufficiently high solubility (>3 M) in conventional DEGDME-based electrolytes (Figure 3.16). The concentration of salts varied from 0 to 3 M, and corresponding Raman spectra are presented in Figure 3.17a and Figure 3.18a. The strong linearity between the salt concentration and characteristic peak intensity of the Cl–O bond from the ClO_4^- anion at approximately 945 cm^{-1} in Figure 3.18b indicates that the electrolytes were well prepared for each targeted composition. The variation in C–O–C stretching vibration, a main functional bond of DEGDME solvents, with increasing salt concentration is shown in Figure 3.17a along with the deconvolutions of the corresponding peaks. As reported in previous Raman studies and as shown in Figure 3.18c–d, the two major bonding modes at 807 and 849 cm^{-1} along with an additional minor peak at 824 cm^{-1} are assigned to DEGDME free solvent (blue line), and those at 837 and 866 cm^{-1} correspond to the coordinated C–O–C vibrational modes with alkali metal ions, which are denoted by a red line.[52-54] Figure 3.17a shows that with increasing electrolyte concentration from 0.1 to 1 M, the peaks of the coordinated bonding modes grew remarkably at the expense of those from the free solvent. The coordinated bonding modes started to become

dominant in the overall spectra for the electrolytes for concentrations of 2 M or greater, which indicates that the majority of the solvents are Na^+-coordinated in these electrolyte systems. The solvation structure of the 3 M electrolytes was mostly composed of coordinated solvents with a only negligible amount of free solvents.[34,35,40,46,53] An infrared spectroscopy study provided consistent evidence of the evolution of the coordinated structures in high-concentration electrolytes, as shown in Figure 3.17b and Figure 3.19. The spectra of the DEGDME free solvent in the figure are typically composed of three vibrational modes, including major C–O–C bonding at 853 cm^{-1}.[55,56] However, similar to the Raman spectra, a drastic change was observed in the spectra of the >2 M electrolytes with two new characteristic peaks emerging at 837 and 862 cm^{-1} and those from the freesolvents disappearing, supporting the dominant formation of a Na^+–DEGDME solvated complex with negligible free solvents. Additionally, ^{23}Na nuclear magnetic resonance (NMR) spectra were recorded to probe the change in local environments around Na^+ ions in the $NaClO_4$/DEGDME electrolytes and to visualize the solvating structures.[9,57-61] Figure 3.17c shows the chemical shifts of ^{23}Na in the electrolytes as a function of concentration, which reflects the interactions of Na^+ cations with either solvated molecules or counter anions in solutions of specific concentrations. The ^{23}Na chemical shift for 0.1 M was measured to be −8.12 based on the standard ^{23}Na resonance in 1 M NaCl aqueous solution. A positive shift to −7.65 was observed for the ^{23}Na NMR peak for the 0.5 M electrolytes, and larger shifts were recorded upon increasing the concentrations to 1 M, 2 M, and 3 M (−7.55, −7.35 and −7.28,

respectively). Such variation of the ^{23}Na chemical shift is indicative of systematic changes in the coordination nature around the Na^+ cations with increasing concentration.[62] It has been suggested that the replacement of solvent molecules by counter anions leads to notable changes in the ^{23}Na NMR resonance, and, if the counter anion is a weak electron donor and thus possesses a poor solvating capability to the cations, the ^{23}Na cation is prone to de-shielding, which results in downfield ^{23}Na resonance with a higher chemical shift value.[57,60] Considering the lower donor number (DN) of the ClO_4^- anion (DN = 8.44)[63] compared with that of DEGDME (DN = 18)[9,64], a positive ^{23}Na shift can be attributed to the incorporation of weakly solvating ClO_4^- (lower DN) in the solvation shell via the formation of a contact-ion-pair (CIP) in concentrated electrolytes, which is in accordance with previous ^{23}Na NMR observations for $NaClO_4$ solutions.[57-60] The combined Raman, infrared, and ^{23}Na NMR spectra verify the evolution of unique solvation structures as well as the elimination of uncoordinated free solvents in the concentrated electrolytes.

To quantitatively understand the solvation characteristics in concentrated electrolytes, the molar ratio between the DEGDME solvent and Na^+ was estimated as a function of the concentration, as shown in Figure 3.17d. The solvent-to-salt ratio exponentially decreased with increasing concentration: 69.8 (0.1 M), 13.96 (0.5 M), 6.98 (1 M), 3.49 (2 M), and 2.33 (3 M). It is worth noting that the O coordination number of Na^+ with ether functional groups has been suggested to be in the range of 4 to 6, and considering the three C–O–C bonds in a single DEGDME

molecule, the molar ratio between DEGDME and Na^+ for fully coordinated solutions is believed to be approximately 2.[9,65] Thus, in 3 M solution, it is speculated that most of the solvents (2/2.33 ~85.8%) are coordinated with Na^+ assuming the maximum Na^+ coordination, whereas approximately 14.2% would remain as free solvents, which might be related to the detectable amount of free solvents in Figure 3.17a and b. The ratios between free and solvated solvents can also be experimentally estimated from Raman spectra, as shown in Figure 3.17e. Based on the intensity comparison, the number of solvating solvents in a 3 M electrolyte is likely to be 2.5 times larger than that of a free solvent, which translates to 71.4% of solvating solvents in the electrolyte. We observed that this finding is also consistent with our hypothetical solvation structures of high-concentration electrolytes shown in Figure 3.20, which suggests that the concentrated electrolytes are composed of agglomerates of five-oxygen-coordinated Na^+, involving a DEGDME molecule and perchlorate anion, and a small amount of uncoordinated DEGDME solvents.

We also analyzed the physical properties of the concentrated electrolytes related to ionic conductivity, as the high viscosity of concentrated electrolytes has generally been perceived as one of their main demerits in terms of ionic transport properties.[33,66] Figure 3.17f displays the viscosity change of electrolytes with different concentrations of Na salts. The viscosity of the pure DEGDME was measured to be 0.9 cP; however, it gradually increased upon increasing the concentration to 2 M (8.52 cP) and drastically surged to 25.4 cP at a concentration of 3 M. It is clear that strong Na^+ ion–dipole interactions in high-concentration

systems induce higher friction against movement, leading to an increase in the viscosity of the solutions. Figure 3.17g shows the ionic conductivities of $NaClO_4$/DEGDME electrolytes as a function of concentration. Although a higher concentration resulted in an increase in ionic conductivity up to a concentration of 2 M (8.06 mS cm^{-1}), most likely because of the increase in the number of charge carriers, the unusually high viscosity in the 3 M electrolyte resulted in a considerable decrease in the ionic conductivity to 4.65 mS cm^{-1}. Nevertheless, it is worthwhile to note that the ionic conductivities of the concentrated electrolytes (~3 M) were comparable to those of the 0.5 M electrolytes (3.09 mS cm^{-1}), which is the most commonly used electrolyte system in sodium–oxygen batteries.[1,2,6,7,23,26,67]

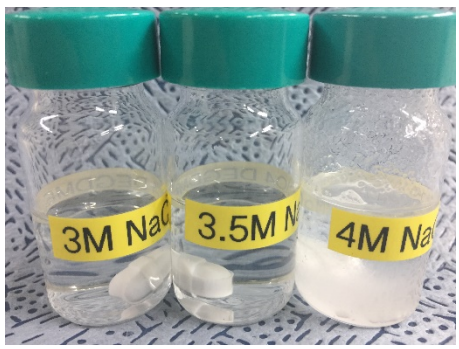

Figure 3.16. Photograph of electrolyte solutions with target concentration of 3 M, 3.5 M, and 4 M $NaClO_4$ dissolved in DEGDME. While electrolytes of 3 M and 3.5 M concentration exhibit clear and transparent solutions, the visual inspection of 4 M stale solution indirectly indicates that it is beyond the solubility limit.

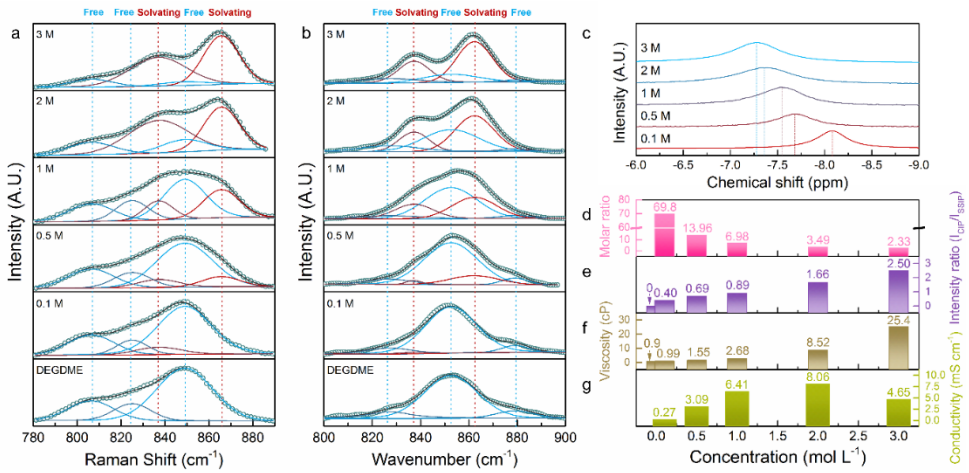

Figure 3.17. Solvation structures and physicochemical properties of concentrated electrolytes. (a) Raman spectra, (b) infrared spectra, and (c) NMR spectra of electrolytes ($NaClO_4$ in DEGDME) for different concentrations (0 to 3 M). (d) Estimated molar ratio of DEGDME molecules to sodium ions for different concentrations. (e) Intensity ratio of Raman peak between solvated solvent (866 cm^{-1}) to free solvent (850 cm^{-1}). (f) Viscosity and (g) ionic conductivity of electrolytes as a function of concentration.

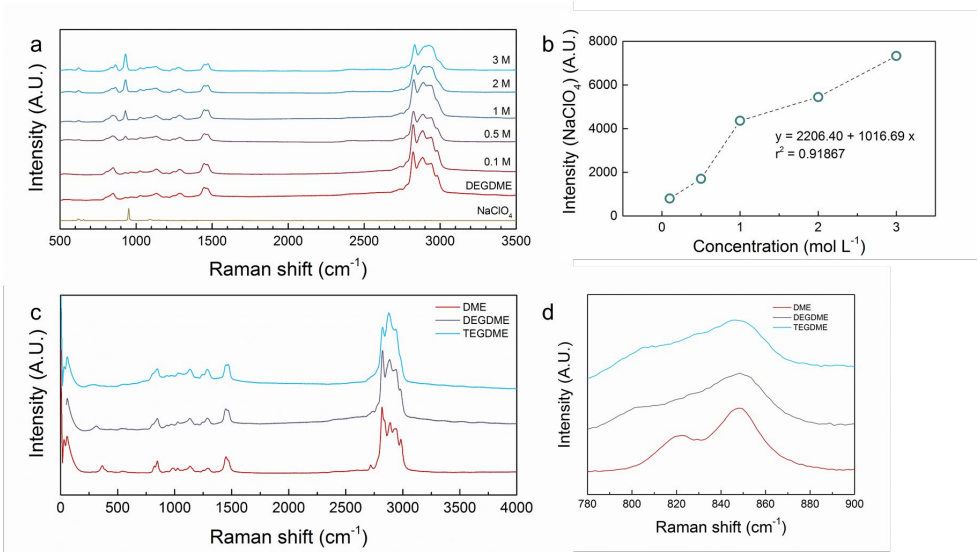

Figure 3.18. Raman spectra for concentrated electrolytes. (a) Full Raman spectra of $NaClO_4$ in DEGDME electrolytes within Raman shift from 500 to 4000 cm^{-1} as a function of concentration. (b) Linearity relation between salt concentration and Cl–O bond intensity at ~945 cm^{-1}. (c) Raman spectra of linear ether family (DME, DEGDME, and TEGDME). (d) Magnified Raman spectra for the Raman shift within the range of 780–900 cm^{-1}.

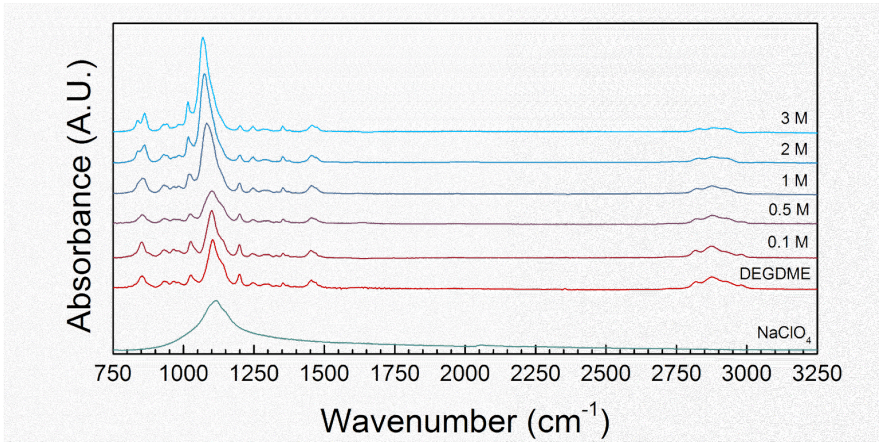

Figure 3.19. Full infrared spectra of $NaClO_4$ in DEGDME electrolytes for wavenumbers from 750 to 3250 cm^{-1} as a function of concentration.

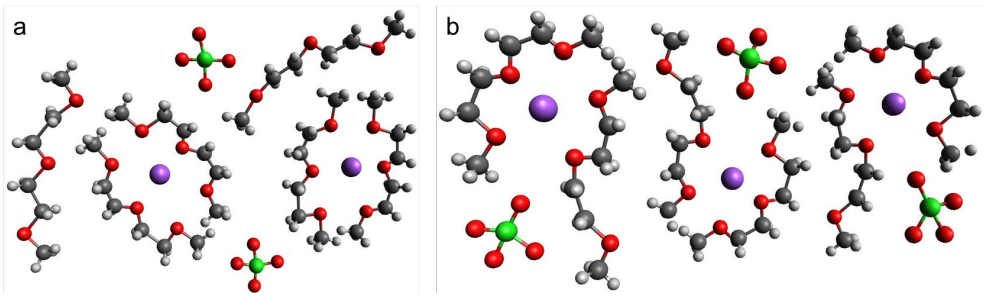

Figure 3.20. Schematic illustration of hypothetical solvation structures of $NaClO_4$ in DEGDME electrolytes. (a) SSIP structure in dilute (0.5 mol dm^{-3}) electrolytes. (b) CIP structure in concentrated (3 mol dm^{-3}) electrolytes. (Dark gray – C, Gray – H, Red – O, Purple – Na, Green – Cl) Figure 3.20 presents solvated Na^+ structures in two representative electrolyte systems (0.5 and 3 M), which show that Na^+ ions are in six O coordination of solvent-separate ion pair (SSIP) in a dilute solution and have five C–O–C bonds by contact ion pair (CIP) in a high-concentration system. Notably, the ratio of coordinating solvents in the high-concentration systems is approximately 72% for the 3 M system, which coincides with the value estimated from the Raman spectra in the Figure 3.17a.

3.2.3.3 Prolonged lifetimes of sodium superoxide in concentrated electrolytes

Having revealed the substantial elimination of free solvents in concentrated electrolytes, we examined the effect of this change on the chemical durability of sodium superoxide in sodium–oxygen batteries through time-dependent characterizations. We discharged the sodium–oxygen cells with a capacity of 1 mAh to produce sodium superoxide on the electrodes and retrieved the discharge product from disassembled cells. After washing away the residual electrolytes, we stored the electrodes in electrolytes of different concentrations in Ar atmosphere at room temperature and monitored the phase evolution for several days. As shown in the X-ray diffraction (XRD) patterns of the as-discharged electrodes in conventional 0.5 M electrolytes (Figure 3.21a), the primary discharge product was identified to be solely sodium superoxide. However, the characteristic diffraction patterns of sodium superoxide diminished within 1 day of storage, whereas new peaks indicating the presence of sodium peroxide dihydrate dominantly evolved.[7,23-25] Within 2 days of storage in the conventional electrolyte, all the characteristic peaks of sodium superoxide disappeared. This phase transition was also supported by the scanning electron microscope (SEM) observations. The well-grown cubic morphologies of sodium superoxide were observed on the carbon electrode directly after discharge (Figure 3.21b), whereas almost all the products transformed into nano-rod particles, which is the typical morphology of sodium peroxide dihydrate,

after 1 day of storage in the conventional electrolyte, as shown in Figure 3.21c.

Similar characterizations were also performed for the concentrated electrolytes. Figure 3.21d demonstrates that the stability of the sodium superoxide phase was significantly improved in the concentrated electrolytes. Contrary to the rapid degradation in conventional electrolytes, the characteristic pattern of sodium superoxide was detectable even after prolonged aging for 5 days in the concentrated electrolytes. Although the signature of sodium peroxide dihydrate was simultaneously detected, its evolution rate was markedly retarded compared with that for the storage experiments in the conventional electrolytes. The delayed phase transition in the concentrated electrolyte was confirmed by the Raman spectra, as shown in Figure 3.21e and Figure 3.22. The characteristic Raman shift of sodium superoxide at 1156 cm^{-1} was stably maintained even after 5 days, and a new peak at 1136 cm^{-1} attributable to sodium peroxide dihydrate began to appear after 2 days.[27,68] The prolonged lifetime of sodium superoxide was further verified by analyzing the morphology evolution of the discharged products. The SEM images in Figure 3.21f–j clearly demonstrate that the initial cubic-shaped sodium superoxide was relatively well preserved even after 2-day and 3-day storage. Consistent with the XRD patterns and Raman spectra, the cubic-shaped sodium superoxide can also be observed in the 5-day-stored carbon electrodes in Figure 3.21j; however, the surface of the product mostly transformed into rod-shaped sodium peroxide dihydrate.

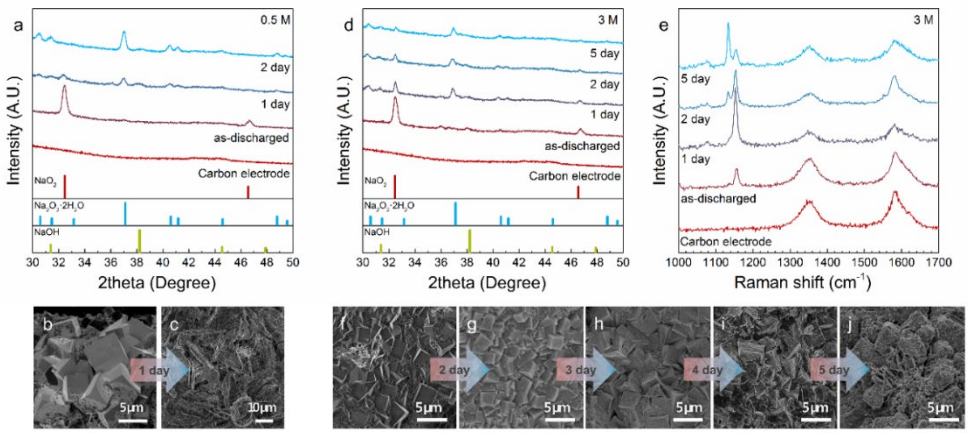

Figure 3.21. Time-resolved characterizations of discharged electrode immersed in different electrolytes. (a) *Ex situ* XRD patterns of discharged electrodes retrieved from sodium–oxygen cells with aging in conventional electrolytes. (b) SEM images of as-discharged electrodes and (c) discharged electrodes stored for 1 day in conventional electrolytes. (d) *Ex situ* XRD patterns and (e) Raman spectra of discharged electrodes retrieved from sodium–oxygen cells with aging in concentrated electrolytes. (f) SEM images of as-discharged electrodes and (g–j) discharged electrodes stored for (g) 2 days, (h) 3 days, (i) 4 days, and (j) 5 days in concentrated electrolytes.

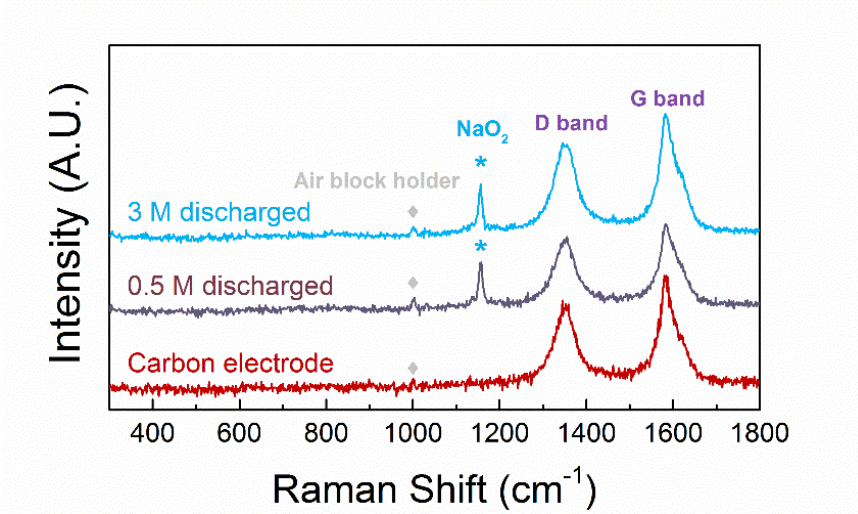

Figure 3.22. Full Raman spectra of discharged carbon electrodes.

3.2.3.4 Reversibility of Na–O_2 batteries

Inspired by the enhanced durability of sodium superoxide, we employed concentrated electrolytes in sodium–oxygen cells and investigated the electrochemical properties as a function of storage period using electrochemical protocols analogous to those used in Figure 3.14a. Figure 3.23a presents the electrochemical profiles of sodium–oxygen cells with concentrated electrolytes (solid line) as a function of storage time compared with those using conventional electrolytes (dotted line). In contrast to the rapid fade of the charging capacities with longer storage time for the cells containing conventional electrolytes, the charging capacities were remarkably well preserved for the cells containing concentrated electrolytes (Figure 3.23a). Even for the storage time of 24 h, almost 80% of the charging capacity compared with the case without the rest could be deliverable, which contrasts with the less than 20% capacity for the conventional electrolytes for the same storage time. These findings support the belief that the introduction of concentrated electrolytes enhances the reversibility of sodium–oxygen chemistry by effectively obstructing side reactions involving sodium superoxide during storage. Additional storage experiments performed for different electrolyte concentrations are provided in Figure 3.24 of Supporting information.

DEMS analyses more clearly demonstrated that the use of concentrated electrolytes successfully conserves the oxygen efficiency and reversibility of sodium–oxygen batteries even after a long storage time. Figure 3.23b–e display oxygen consumption and evolution profiles of 3-h and 24-h stored sodium–oxygen

cells using concentrated electrolytes. The pressure variations during discharge in Figure 3.23b and 3.23d indicate that the ideal electron-to-oxygen ratio and one-electron sodium superoxide formation reaction are followed. For the charge process in Figure 3.23c (3-h stored cell), it was also observed that the oxygen gas solely evolved during the charge process below 3 V, keeping the oxygen evolution rate close to the theoretical value of the electron-to-oxygen ratio. More importantly, the oxygen gas profile for charging of 24-h stored cells is nearly identical to those of cells without aging in Figure 3.23e. This result clearly contrasts with that for the sodium–oxygen cell using conventional electrolytes, which show a substantial reduction in the oxygen evolution after the same storage period in Figure 3.14c. This finding validates the idea that the enhanced stability of sodium superoxide in the electrolyte is the key to the higher efficiency and reversibility of sodium–oxygen cells with resting periods. There was a slight reduction of the oxygen efficiency from 71% to 64% with 1 day of storage for concentrated electrolytes (Table S2), which is attributable to the small fraction of the phase transition even in the concentrated electrolytes. Nevertheless, the value remains high and comparable to that of non-aged sodium–oxygen cells using conventional electrolytes.

Additionally, we examined the effect of concentrated electrolytes on the cell impedance of sodium–oxygen cells during the storage period. Nyquist plots recorded every 2 h during the storage are presented in Figure 3.23f. The initial cell impedance immediately after the discharge was approximately 1,500 Ω, and the

total impedance only slightly increased to 2,000 Ω after 24 h, which contrasts with the significant rise in the impedance for the cells using conventional electrolytes, as shown in Figure 3.14f. This observation is also consistent with the smaller charging overpotential increases observed in Figure 3.23a. Whereas the charging overpotential of the cells using the conventional electrolytes became markedly larger with longer storage, the charging overpotential remained relatively constant regardless of the storage time for the cells using concentrated electrolytes because of the suppressed formation of byproducts.

The higher durability of the system was finally confirmed by using electrochemical cycling tests with repeated resting periods. Figure 3.23g shows the capacity retention capability of the cells using concentrated electrolytes with a storage time of 0 or 12 h introduced every cycle. The cells could sustain a high cyclic stability even with 12-h rest after every discharge process, which corresponds to approximately 60% of the original cycle reversibility for non-aged cells, as shown in Figure 3.23g and Figure 3.25. This is a remarkable improvement in the cyclability compared with that of the cells using conventional electrolytes, which maintained only 30% of the original cycle reversibility for the same storage time. It is also noteworthy that the cycle performance of the cells without storage was also improved by employing concentrated electrolytes. This improvement is believed to be due to the suppression of other parasitic reactions involving the free solvent in the electrolyte and the improved anodic stability in the high-concentration systems (Figure 3.26).

The fact that the concentrated electrolytes used in present study could not completely prevent the cycle-life decay over the storage period might be attributed to parasitic reactions with trace amounts of free solvents that were not completely removed, as discussed in the electrolyte structure analyses. Nevertheless, this study clearly verifies that the chemical stability of sodium superoxide could be significantly improved through electrolyte engineering, and we expect that further electrolyte design might provide a potential route to achieve much longer stability of sodium superoxide and better durability of sodium–oxygen batteries.

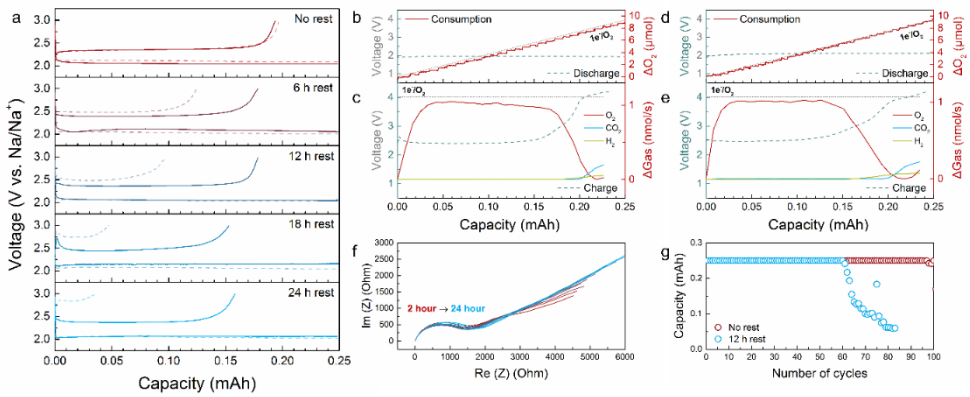

Figure 3.23. Enhanced storage properties of sodium–oxygen cells with concentrated electrolytes. (a) Charge/discharge profiles of sodium–oxygen cells with various resting times from 6 to 24 h after discharge. (b) Pressure monitoring during discharge and (c) real-time gas profiles during charge of sodium–oxygen cells stored for 3 h. (d) Pressure monitoring during discharge and (e) real-time gas profiles during charge of sodium–oxygen cells stored for 24 h. The dotted lines are voltage profiles. (f) Electrochemical impedance spectra of discharged sodium–oxygen cells during storage for 24 h. (g) Capacity retention of sodium–oxygen cells with and without resting periods.

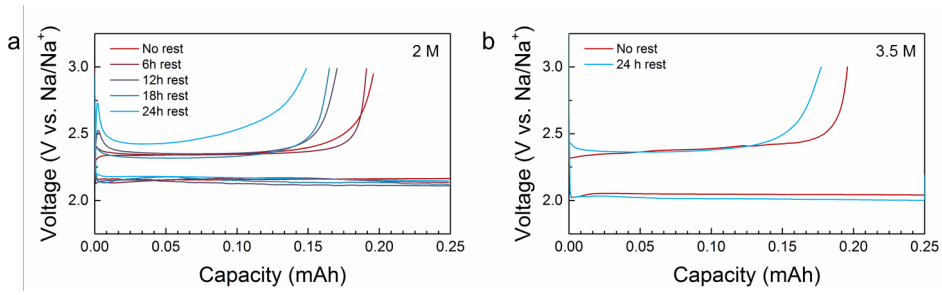

Figure 3.24. Voltage profile of sodium–oxygen cells using (a) 2 M and (b) 3.5 M electrolytes with different resting condition.

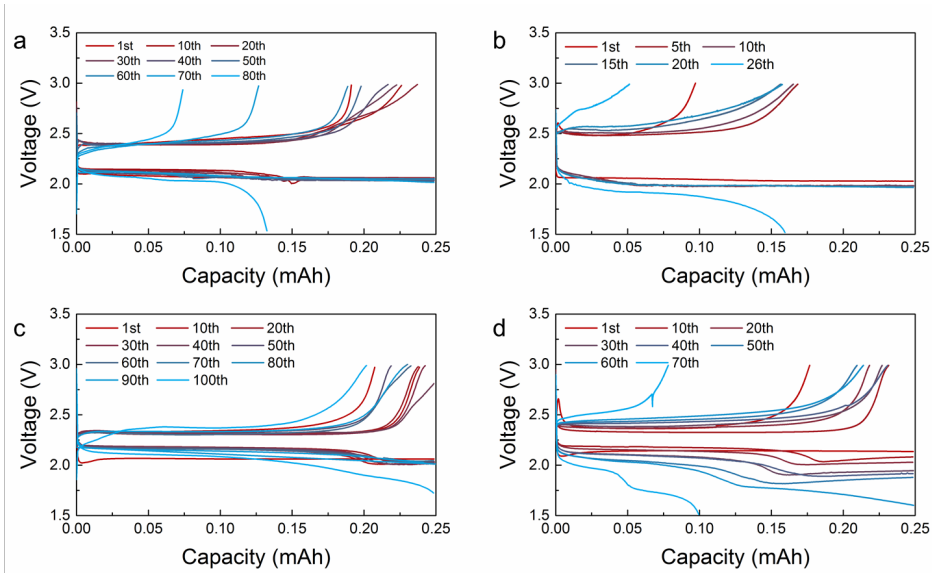

Figure 3.25. Voltage profiles of sodium–oxygen cells for individual cycle number. (a,b) Voltage profiles of sodium–oxygen cells for 0.5 M electrolytes (a) without and (b) with 12-h storage after discharge. (c,d) Voltage profiles of sodium–oxygen cells for 3 M electrolytes (c) without and (d) with 12-h storage after discharge.

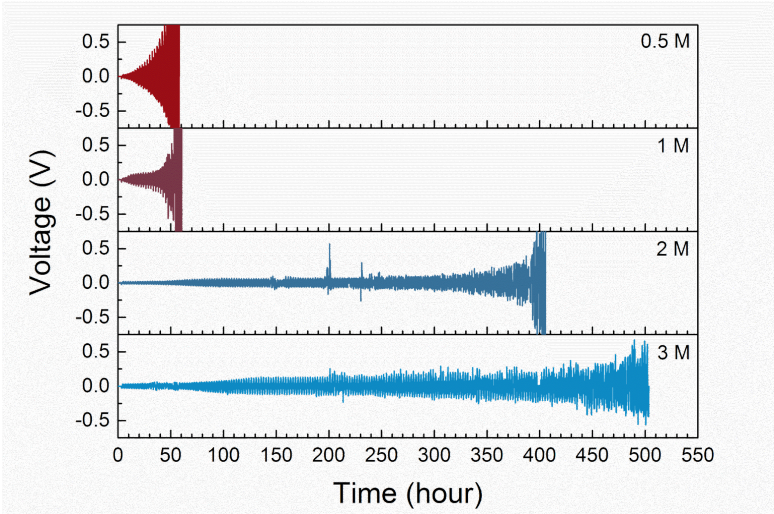

Figure 3.26. Investigation of Na metal stability of $NaClO_4$ in DEGDME electrolytes with different concentrations using Na/Na symmetric cell tests under a current density of 0.1 mA for 2.5 h within ±1.5 V.

3.2.4 Concluding Remarks

We addressed the issue of the chemical stability of sodium superoxide in sodium–oxygen batteries and successfully exploited concentrated electrolytes to improve the chemical durability and stability of sodium–oxygen batteries. The degradation of the oxygen efficiency and cell reversibility was shown to be caused by the poor chemical stability of sodium superoxide stored in conventional electrolytes. As a key solution, we adopted a new high-concentration electrolyte containing a significantly decreased amount of free solvents based on our understanding of the solvation structures formed in the electrolyte by tailoring the salt concentrations. The chemical stability of sodium superoxide was shown to be greatly enhanced in the concentrated electrolytes, which led to a prolonged lifetime of sodium superoxide. The use of concentrated electrolytes subsequently resulted in a markedly long shelf-life for sodium–oxygen batteries, which could preserve their intrinsic high efficiency and reversibility even with repeated storage periods. This work is the first to successfully improve the chemical stability of sodium superoxide for a better performing sodium–oxygen battery. We believe that our findings demonstrate the importance of the storage characteristics of metal–oxygen batteries with respect to the chemical stability of discharge products and offer general insights into the role of electrolyte properties in the chemistry of metal–oxygen batteries.

3.2.5 References

1 Hartmann, P. *et al.* A rechargeable room-temperature sodium superoxide (NaO_2) battery. *Nature Materials* **12**, 228-232 (2013).

2 Hartmann, P. *et al.* A comprehensive study on the cell chemistry of the sodium superoxide (NaO_2) battery. *Physical Chemistry Chemical Physics* **15**, 11661-11672 (2013).

3 Lim, H.-D. *et al.* Reaction chemistry in rechargeable Li-O_2 batteries. *Chemical Society Reviews* **46**, 2873-2888 (2017).

4 Bender, C. L., Hartmann, P., Vračar, M., Adelhelm, P. & Janek, J. On the Thermodynamics, the Role of the Carbon Cathode, and the Cycle Life of the Sodium Superoxide (NaO_2) Battery. *Advanced Energy Materials* **4**, 1301863 (2014).

5 Hartmann, P. *et al.* Pressure Dynamics in Metal–Oxygen (Metal–Air) Batteries: A Case Study on Sodium Superoxide Cells. *The Journal of Physical Chemistry C* **118**, 1461-1471 (2014).

6 McCloskey, B. D., Garcia, J. M. & Luntz, A. C. Chemical and Electrochemical Differences in Nonaqueous Li–O_2 and Na–O_2 Batteries. *The Journal of Physical Chemistry Letters* **5**, 1230-1235 (2014).

7 Kim, J. *et al.* Dissolution and ionization of sodium superoxide in sodium–

oxygen batteries. *Nature Communications* **7**, 10670 (2016).

8 Xia, C., Black, R., Fernandes, R., Adams, B. & Nazar, L. F. The critical role of phase-transfer catalysis in aprotic sodium oxygen batteries. *Nature Chemistry* **7**, 496-501 (2015).

9 Lutz, L. *et al.* High Capacity Na–O_2 Batteries: Key Parameters for Solution-Mediated Discharge. *The Journal of Physical Chemistry C* **120**, 20068-20076 (2016).

10 Hartmann, P. *et al.* Discharge and Charge Reaction Paths in Sodium–Oxygen Batteries: Does NaO_2 Form by Direct Electrochemical Growth or by Precipitation from Solution? *The Journal of Physical Chemistry C* **119**, 22778-22786 (2015).

11 Xia, C. *et al.* Direct Evidence of Solution-Mediated Superoxide Transport and Organic Radical Formation in Sodium-Oxygen Batteries. *Journal of the American Chemical Society* **138**, 11219-11226 (2016).

12 Lee, B. *et al.* Theoretical Evidence for Low Charging Overpotentials of Superoxide Discharge Products in Metal–Oxygen Batteries. *Chemistry of Materials* **27**, 8406-8413 (2015).

13 Chen, Y., Freunberger, S. A., Peng, Z., Fontaine, O. & Bruce, P. G. Charging a Li–O_2 battery using a redox mediator. *Nature Chemistry* **5**,

489-494 (2013).

14 Lim, H.-D. *et al.* Superior Rechargeability and Efficiency of Lithium–Oxygen Batteries: Hierarchical Air Electrode Architecture Combined with a Soluble Catalyst. *Angewandte Chemie* **126**, 4007-4012 (2014).

15 Lim, H.-D. *et al.* Rational design of redox mediators for advanced Li–O_2 batteries. *Nature Energy* **1**, 16066 (2016).

16 Liu, T. *et al.* Cycling Li-O_2 batteries via LiOH formation and decomposition. *Science* **350**, 530-533 (2015).

17 Bergner, B. J., Schürmann, A., Peppler, K., Garsuch, A. & Janek, J. TEMPO: A Mobile Catalyst for Rechargeable Li-O_2 Batteries. *Journal of the American Chemical Society* **136**, 15054-15064 (2014).

18 Gao, X. W., Chen, Y. H., Johnson, L. & Bruce, P. G. Promoting solution phase discharge in Li-O_2 batteries containing weakly solvating electrolyte solutions. *Nature Materials* **15**, 882-882 (2016).

19 Gao, X., Chen, Y., Johnson, L. R., Jovanov, Z. P. & Bruce, P. G. A rechargeable lithium–oxygen battery with dual mediators stabilizing the carbon cathode. *Nature Energy* **2**, 17118 (2017).

20 Lim, H.-D. *et al.* A New Perspective on Li–SO_2 Batteries for Rechargeable Systems. *Angewandte Chemie International Edition* **54**, 9663-9667 (2015).

21 Park, H. *et al.* High-efficiency and high-power rechargeable lithium–sulfur dioxide batteries exploiting conventional carbonate-based electrolytes. *Nature Communications* **8**, 14989 (2017).

22 Liu, Z. *et al.* Decomposing lithium carbonate with a mobile catalyst. *Nano Energy* **36**, 390-397 (2017).

23 Ortiz-Vitoriano, N. *et al.* Rate-Dependent Nucleation and Growth of NaO_2 in Na–O_2 Batteries. *The Journal of Physical Chemistry Letters* **6**, 2636-2643 (2015).

24 Sayed, S. Y. *et al.* Revealing instability and irreversibility in nonaqueous sodium-O_2 battery chemistry. *Chemical Communications* **52**, 9691-9694 (2016).

25 Yadegari, H. *et al.* How to Control the Discharge Products in Na–O_2 Cells: Direct Evidence toward the Role of Functional Groups at the Air Electrode Surface. *The Journal of Physical Chemistry Letters* **8**, 4794-4800 (2017).

26 Black, R. *et al.* The Nature and Impact of Side Reactions in Glyme-based Sodium–Oxygen Batteries. *ChemSusChem* **9**, 1795-1803 (2016).

27 Landa-Medrano, I. *et al.* New Insights into the Instability of Discharge Products in Na–O_2 Batteries. *ACS Applied Materials & Interfaces* **8**, 20120-20127 (2016).

28 Neng, X., Rooney, R. T., Gewirth, A. A. & Yiying, W. The Long-Term Stability of KO_2 in K-O_2 Batteries. *Angewandte Chemie International Edition* **57**, 1227-1231 (2018).

29 Sherman, J. Crystal Energies of Ionic Compounds and Thermochemical Applications. *Chemical Reviews* **11**, 93-170 (1932).

30 Hinton, J. F. & Amis, E. S. Solvation numbers of ions. *Chemical Reviews* **71**, 627-674 (1971).

31 Ratkova, E. L., Palmer, D. S. & Fedorov, M. V. Solvation Thermodynamics of Organic Molecules by the Molecular Integral Equation Theory: Approaching Chemical Accuracy. *Chemical Reviews* **115**, 6312-6356 (2015).

32 Ben-Naim, A. Y. *Solvation Thermodynamics* (Springer Science & Business Media, 1987).

33 Yamada, Y. & Yamada, A. Review—Superconcentrated Electrolytes for Lithium Batteries. *Journal of the Electrochemical Society* **162**, A2406-A2423 (2015).

34 Yamada, Y. *et al.* Unusual Stability of Acetonitrile-Based Superconcentrated Electrolytes for Fast-Charging Lithium-Ion Batteries. *Journal of the American Chemical Society* **136**, 5039-5046 (2014).

35 Suo, L., Hu, Y.-S., Li, H., Armand, M. & Chen, L. A new class of Solvent-in-Salt electrolyte for high-energy rechargeable metallic lithium batteries. *Nature Communications* **4**, 1481 (2013).

36 Shin, E. S., Kim, K., Oh, S. H. & Cho, W. I. Polysulfide dissolution control: the common ion effect. *Chemical Communications* **49**, 2004-2006 (2013).

37 Manthiram, A., Fu, Y., Chung, S.-H., Zu, C. & Su, Y.-S. Rechargeable Lithium–Sulfur Batteries. *Chemical Reviews* **114**, 11751-11787 (2014).

38 Yamada, Y. *et al.* Hydrate-melt electrolytes for high-energy-density aqueous batteries. *Nature Energy* **1**, 16129 (2016).

39 Suo, L. *et al.* "Water-in-salt" electrolyte enables high-voltage aqueous lithium-ion chemistries. *Science* **350**, 938-943 (2015).

40 Wang, J. *et al.* Superconcentrated electrolytes for a high-voltage lithium-ion battery. *Nature Communications* **7**, 12032 (2016).

41 Liu, B. *et al.* Enhanced Cycling Stability of Rechargeable Li–O_2 Batteries Using High-Concentration Electrolytes. *Advanced Functional Materials* **26**, 605-613 (2016).

42 He, M. *et al.* Concentrated Electrolyte for the Sodium–Oxygen Battery: Solvation Structure and Improved Cycle Life. *Angewandte Chemie* **128**,

15536-15540 (2016).

43 Suo, L. *et al.* Advanced High-Voltage Aqueous Lithium-Ion Battery Enabled by "Water-in-Bisalt" Electrolyte. *Angewandte Chemie International Edition* **55**, 7136-7141 (2016).

44 Tomiyasu, H. *et al.* An aqueous electrolyte of the widest potential window and its superior capability for capacitors. *Scientific Reports* **7**, 45048 (2017).

45 Yang, C. *et al.* Unique aqueous Li-ion/sulfur chemistry with high energy density and reversibility. *Proceedings of the National Academy of Sciences* **114**, 6197-6202 (2017).

46 Lee, J. *et al.* Ultraconcentrated Sodium Bis(fluorosulfonyl)imide-Based Electrolytes for High-Performance Sodium Metal Batteries. *ACS Applied Materials & Interfaces* **9**, 3723-3732 (2017).

47 Lee, G.-H. *et al.* $MnMoO_4$ Electrocatalysts for Superior Long-Life and High-Rate Lithium-Oxygen Batteries. *Advanced Energy Materials* **7**, 1601741 (2017).

48 Ahn, S. M. *et al.* High-Performance Lithium-Oxygen Battery Electrolyte Derived from Optimum Combination of Solvent and Lithium Salt. *Advanced Science* **4**, 1700235 (2017).

49 McCloskey, B. D., Bethune, D. S., Shelby, R. M., Girishkumar, G. & Luntz, A. C. Solvents' Critical Role in Nonaqueous Lithium–Oxygen Battery Electrochemistry. *The Journal of Physical Chemistry Letters* **2**, 1161-1166 (2011).

50 Knudsen, K. B. *et al.* An Electrochemical Impedance Study of the Capacity Limitations in Na–O_2 Cells. *The Journal of Physical Chemistry C* **120**, 10799-10805 (2016).

51 Nichols, J. E. & McCloskey, B. D. The Sudden Death Phenomena in Nonaqueous Na–O_2 Batteries. *The Journal of Physical Chemistry C* **121**, 85-96 (2017).

52 Geysens, P. *et al.* Solvation Structure of Sodium Bis(fluorosulfonyl)imide-Glyme Solvate Ionic Liquids and Its Influence on Cycling of Na-MNC Cathodes. *The Journal of Physical Chemistry B* **122**, 275-289 (2018).

53 Yamada, Y., Yaegashi, M., Abe, T. & Yamada, A. A superconcentrated ether electrolyte for fast-charging Li-ion batteries. *Chemical Communications* **49**, 11194-11196 (2013).

54 Johansson, P., Grondin, J. & Lassègues, J.-C. Structural and Vibrational Properties of Diglyme and Longer Glymes. *The Journal of Physical Chemistry A* **114**, 10700-10705 (2010).

55 Sun, S., Niu, Y., Sun, Z., Xu, Q. & Wei, X. Solubility properties and spectral characterization of sulfur dioxide in ethylene glycol derivatives. *RSC Advances* **5**, 8706-8712 (2015).

56 Ha, S.-Y. *et al.* Magnesium(II) Bis(trifluoromethane sulfonyl) Imide-Based Electrolytes with Wide Electrochemical Windows for Rechargeable Magnesium Batteries. *ACS Applied Materials & Interfaces* **6**, 4063-4073 (2014).

57 Erlich, R. H. & Popov, A. I. Spectroscopic studies of ionic solvation. X. A Study of the solvation of sodium ions in nonaqueous solvents by ^{23}Na nuclear magnetic resonance. *Journal of the American Chemical Society* **93**, 5620-5623 (1971).

58 Templeman, G. J. & Van Geet, A. L. Sodium magnetic resonance of aqueous salt solutions. *Journal of the American Chemical Society* **94**, 5578-5582 (1972).

59 Greenberg, M. S. & Popov, A. I. Spectroscopic studies of ionic solvation. XXI. A raman, infrared, and NMR study of sodium perchlorate solutions in nonaqueous solvents. *Journal of Solution Chemistry* **5**, 653-665 (1976).

60 DeWitte, W. J. & Popov, A. I. Spectroscopic studies of ionic solvation. XIX. Fluorine-19 and sodium-23 NMR studies of ionic interactions in nonaqueous solutions of hexafluorophosphate salts. *Journal of Solution*

Chemistry **5**, 231-240 (1976).

61 Alessandro, B., Stefano, M., Cristina, P. & Gianfranco, S. Investigation of Cation−Anion Interactions in 2-Propanol Solutions of Sodium Alkoxides and Thiolates by ^{23}Na-NMR Spectroscopy. *European Journal of Organic Chemistry* **2000**, 1953-1957 (2000).

62 Wong, A. & Wu, G. Solid-State ^{23}Na Nuclear Magnetic Resonance of Sodium Complexes with Crown Ethers, Cryptands, and Naturally Occurring Antibiotic Ionophores: A Direct Probe to the Sodium-Binding Sites. *The Journal of Physical Chemistry A* **104**, 11844-11852 (2000).

63 Burke, C. M., Pande, V., Khetan, A., Viswanathan, V. & McCloskey, B. D. Enhancing electrochemical intermediate solvation through electrolyte anion selection to increase nonaqueous Li–O_2 battery capacity. *Proceedings of the National Academy of Sciences* **112**, 9293-9298 (2015).

64 Aldous, I. M. & Hardwick, L. J. Solvent-Mediated Control of the Electrochemical Discharge Products of Non-Aqueous Sodium–Oxygen Electrochemistry. *Angewandte Chemie* **128**, 8394-8397 (2016).

65 Wahlers, J. *et al.* Solvation Structure and Concentration in Glyme-Based Sodium Electrolytes: A Combined Spectroscopic and Computational Study. *The Journal of Physical Chemistry C* **120**, 17949-17959 (2016).

66 Xu, K. Electrolytes and Interphases in Li-Ion Batteries and Beyond. *Chemical Reviews* **114**, 11503-11618 (2014).

67 Zhao, N. & Guo, X. Cell Chemistry of Sodium–Oxygen Batteries with Various Nonaqueous Electrolytes. *The Journal of Physical Chemistry C* **119**, 25319-25326 (2015).

68 Pinedo, R. *et al.* Insights into the Chemical Nature and Formation Mechanisms of Discharge Products in Na–O_2 Batteries by Means of Operando X-ray Diffraction. *The Journal of Physical Chemistry C* **120**, 8472-8481 (2016).

Chapter 4. Conclusion

Search for new battery chemistry which can outperform current state-of-the-art Li ion battery technilogies has been vigorously deveoted to satisfying ongoing increasing demands for energy storage deviecs to be adpoted in electric vehicles and grid-scale energy stroage systems. Although a Li–O_2 battery, the most representative metal–gas system, has been extensively studied as a promising candidate for future high-energy storage devices, intrinsically poor efficiency and reversibility of Li–O_2 chemistry hinders the developments of practical commercializations. In this thesis, electrochemical couplings of metal–gas have been examined to develop high-energy-density batteries, taking advantage of the use of light metal and gas.

Primary Li–SO_2 batteries, which can offer high energy/power density and exceptionally long shelf-life, have been believed only as a primary battery not a rechargeable battery due to the formation of solid products. Taking inspiration from the electrochemically decomposable property of solid Li_2O_2 in Li–O_2 battery, however, I shed a new light on primary Li–SO_2 battery by adopting Li–O_2 cell configuration in Chapter 2. I proved a reversible decomposition of solid $Li_2S_2O_4$ accompanying clear evolution of SO_2 gas during the charge of Li–SO_2 battery and thus successfully proposed a new promising rechargeable Li–SO_2 chemistry. In-depth study through combined calculations and experiments revealed that underlying reaction mechanism and battery performance of Li–SO_2 chemistry are critically affected by the electrolyte solvating properties. Although commercial carbonate-based electrolytes for Li ion batteries have not been considered for current metal-gas

type rechargeable batteries due to the occurrence of serious side reactions, I succeeded in exploiting commercial carbonate-based electrolytes into Li–SO_2 battery with significantly boosting battery performances. To be much practically feasible, I proposed a novel class of Li–SO_2 chemistry as a high performance rechargeable battery by introducing soluble catalysts, achieving one of the highest energy efficiencies, power capabilities, and cycle stabilities.

Na–O_2 chemistry has also been recently proposed as a promising candidate for next-generation battery owing to intrinsically high energy density and efficiency. However, conflicting observations concerning Na–O_2 reactions with different discharge products have inhibited the understanding of the precise reactions occurring in the battery. By addressing the issue of discrepancy on discharge products, I verified that the origin of different discharge products is due to the phase transition of NaO_2 material to the other product of $Na_2O_2 \cdot 2H_2O$ triggered by its dissolution property in the electrolyte in Chapter 3. It was also found that the formation of byproducts leads to lower cell efficiency and oxygen reversibility of the cells. Based on the understanding of reaction mechanism in Na–O_2 batteries, I proposed a strategy to prevent dissolution of NaO_2 by a rational tuning of electrolytes. I explored concentrated electrolytes which have significantly small number of free solvents to suppress the dissolution of NaO_2 in Na–O_2 batteries. I found out that solid NaO_2 stored in concentrated electrolytes exhibit markedly prolonged chemical stability and thus could demonstrate the enhanced durability and storage properties of Na–O_2 batteries with the introduction of concentrated electrolytes..

In summary, I proposed a new design strategy of metal–gas rechargeable batterise, addressed the fundamenatl understanding on the reaction mechanism of the batteris and attempted to develop high-performing metal–gas batterises. Although the research on the metal–gas battery is at the infant stage, I expect that all the efforts and approaches in this thesis contribute to open up a new battery chemistry and enrich scientific understanding on metal–air electrochemistry.

Chapter 5. Abstract in Korean

초 록

최근 전기자동차 등의 에너지 저장 기술 기반 시장의 성장과 함께 에너지 저장 장치에 대한 수요가 폭발적으로 증가하고 있다. 현재 최첨단 에너지 저장 기술로 여겨지는 리튬이온전지는 높은 에너지 밀도와 출력을 바탕으로 다양한 소형 전자기기의 전력 공급원으로 사용되고 있다. 하지만 전지의 양극 소재 내 무거운 전이 금속과 제한된 저장 용량으로 인해, 현재 리튬이온전지의 에너지 밀도는 전기자동차와 같은 대형 에너지 저장 기술에 적용되기에 부족하다. 이에 리튬이온전지의 성능을 뛰어 넘는 차세대 전지 화학(리튬-공기, 리튬-황, 소듐 전지 등)을 개발하기 위한 많은 연구들이 진행되어 왔다. 그 중 리튬-공기 전지는 무거운 원소를 활용하지 않으며 매우 높은 이론 에너지 밀도를 갖고 있어 차세대 전지로 상당한 주목을 받고 있다. 하지만, 리튬과 산소의 화학 반응의 낮은 효율과 가역성으로 인해 실제 상용 전지로서 차세대 리튬-공기 전지의 개발에 어려움을 겪고 있다.

본 논문에서는, 새로운 금속과 기체의 전지 화학을 탐구하여 차세대 대용량 이차 전지를 개발하는 방법을 제시한다. 기존 리튬-공기 전지의 개발 배경과 원론적인 이해를 바탕으로, 전기화학 활성을 나타내는 다양한 기체 활물질을 알칼리 금속과 조합하여 전기화학 전지를 구성하면 높은 효율과 가역성의 전지를 개발하는 한 방법이 될 수 있다. 본 논문에서 기존 일차 리튬-이산화황 일차전지를 재조명하여 새로운 이차 전지를 제안하고, 에너지 저장 기작 규명과 함께 고성능의 리튬-이산화황 전지를 개발했다. 또한, 최근 각광 받고 있는 나트륨-공기 전지의 초과산화물 반응 기작을 밝혀내고, 반응 생성물을 제어할 수

있는 전해질을 도입하여 화학적으로 안정성이 높은 나트륨-공기 전지 시스템을 개발했다.

2장에서는, 새로운 이차 전지를 개발하기 위해 기존 리튬-이산화황 일차전지를 재조명한다. 리튬-이산화황 전지는 고체 방전 산물의 생성으로 인해 재충전이 불가능하다고 여겨졌으나 본 연구에서 아이티온산리튬의 가역적인 생성과 분해를 통한 리튬-이산화황 전지의 충전 가능성을 증명했다. 리튬-이산화황 이차 전지는 약 2.8 V의 반응 전압과 5,400 $mA\,h\,g^{-1}$의 용량을 발현하며, 기존 리튬-공기 전지 보다 높은 에너지 효율과 전지 가역성을 나타냈다. 메커니즘에 대한 심도 있는 연구를 바탕으로 리튬이온전지에 사용되는 상용 탄산염계 전해질을 리튬-이산화황 전지에 도입해냈다. 탄산염계 전해질을 사용한 전지는 출력과 가역성 등에서 우수한 성능을 나타냈다. 액상 촉매 또한 적용되어 리튬-기체 형태 전지들 중 가장 우수한 수준의 전지 성능을 보이는 리튬-이산화황 전지를 개발했다.

3장에서는, 나트륨-공기 전지에서 발견되는 이종 반응 산물의 원인과 그 메커니즘에 대해 밝혀냈다. 매우 낮은 충전 과전압으로 충전이 가능하기 때문에 나트륨초과산화물 기반 전지는 최근 많은 관심을 받고 있다. 본 연구에서 나트륨초과산화물이 전해질 내 용해 및 해리되어 자유 산소 라디칼을 발생시키고 수화된 나트륨과산화물을 형성하는 부반응을 촉진한다는 것을 밝혀냈다. 이러한 부반응은 충전 시 높은 과전압을 요하며 전지 성능의 급격한 열화를 초래한다. 이에 메커니즘에 대한 이해를 바탕으로 나트륨초과산화물의 용해를 막기 위한 전해질을 탐색했다. 고농도의 전해질을 도입하여 나트륨초과산화물의 부반응을 억제할 수 있음을 규명해냈고, 높은 저장 수명을 나타내는 높은 화학 안정성의 나트륨-공기 전지를 개발해냈다.

본 논문은 금속-기체 타입의 새로운 이차전지라는 연구 방향을 제시해

줄 뿐만 아니라 에너지 저장 메커니즘을 이해하는데 영감을 줄 수 있을 것으로 기대된다. 또한 본 연구에서 기존 전지에 대해 재조명한 연구 방식은 새로운 이차 전지를 개발하는 하나의 방안을 제시해주며, 전해질 및 촉매 개발 등의 연구는 금속-기체 전지 성능 향상을 위한 연구 방향을 제시해 줄 것으로 기대된다.

주요어: 전기화학, 이차 전지, 금속-공기 전지, 이산화황, 초과산화물, 전해질, 액상 촉매.

학 번: 2014-21476

Curriculum Vitae

Hyeokjun Park

Seoul National University

Department of Materials Science and Engineering

1 Gwanak-ro, Gwanak-gu, Seoul, Republic of Korea

E-mail: hyuckjun7@snu.ac.kr

Office: +82-2-880-7165

Cell: +82-10-9797-9286

ORCID: 0000-0003-3367-8881

Educational Background

- **Integrated Course of Master and Ph. D. Candidate**

March 2014 – February 2019

Advanced Energy Materials Laboratory

Department of Materials Science and Engineering

Seoul National University | Republic of Korea

(Supervisor: Prof. Kisuk Kang)

- **Bachelor of Science**

March 2010 – February 2014

Department of Materials Science and Engineering

Seoul National University | Republic of Korea

Research Interests

Materials science for high-energy rechargeable batteries

New metal-gas chemistry for advanced secondary batteries

- Advanced metal–air/gas rechargeable batteries
- Lithium/Sodium metal electrodes for next-generation batteries
- Electrolytes designs for advanced batteries (Redox mediators, Concentrated electrolytes, Gas-phase additives)

Fundamental studies on battery mechanisms

- Understanding solution dominant reaction in metal-air batteries (Impact of electrolyte properties, Redox mediators)
- Surface chemistry on SEI layer of metal electrodes
- *In situ* characterizations for battery reactions (Differential electrochemical mass spectroscopy, Liquid cell transmission electron microscope, In situ Raman spectroscopy)

Honors and Scholarships

- Korea National Science & Technology Scholarship (2012 – 2013)
- Global Ph. D. Fellowship (2015-2019, NRF-2015H1A2A1033886)
- Best poster award in Nano Korea 2014
- Best paper award in The Korean Society of Industrial and Engineering Chemistry 2016 Spring meeting
- Best poster award in The Korean Electrochemical Society 2017 Fall meeting

List of Publications

(1) Journals (First author)

† These authors contributed equally.

1) Donghoon Lee†, **Hyeokjun Park**†, Youngmin Ko, Hayoung Park, Taeghwan Hyeon, Kisuk Kang and Jungwon Park "Direct observation of solution-phase discharge in Li–O_2 battery by liquid phase transmission electron microscopy", in preparation (2018)
2) **Hyeokjun Park**, Hee-Dae Lim, Youngjoon Bae, Sung Kwan Park, Youngmin Ko, Byungju Lee and Kisuk Kang "A New High-Power Rechargeable Sodium–Sulfur Dioxide Battery", in preparation (2018)
3) Youngmin Ko†, **Hyeokjun Park**†, Byunghoon Kim†, Juseong Kim and Kisuk Kang "Redox mediators: A solution for advanced lithium–oxygen batteries", *Trends in Chemistry,* Submitted (2018)
4) Youngjoon Bae†, **Hyeokjun Park**†, Youngmin Ko†, Hyunah Kim†, Sung Kwan Park and Kisuk Kang "Bifunctional Oxygen Electrocatalysts for Lithium–oxygen Batteries", *Batteries & Supercaps*, Accepted (2018)
5) **Hyeokjun Park**, Jinsoo Kim, Myeong Hwan Lee, Sung Kwan Park, Do-hoon Kim, Youngjoon Bae, Youngmin Ko, Byungju Lee and Kisuk Kang "Highly durable and stable sodium superoxide in concentrated electrolytes for sodium–oxygen batteries", *Advanced Energy Materials*, Vol. 8, pp. 1801760 (2018)
6) Sehwan Moon†, **Hyeokjun Park**†, Gabin Yoon, Myeong Hwan Lee, Kyu-Young

Park and Kisuk Kang "Simple and Effective Gas-Phase Doping for Lithium Metal Protection in Lithium Metal Batteries", *Chemistry of Materials*, Vol 29, pp. 9182-9191 (2017)

7) **Hyeokjun Park**, Hee-Dae Lim, Hyung-Kyu Lim, Won Mo Seong, Sehwan Moon, Youngmin Ko, Byungju Lee, Youngjoon Bae, Hyungjun Kim and Kisuk Kang "High-efficiency and high-power rechargeable lithium–sulfur dioxide batteries exploiting conventional carbonate-based electrolytes", *Nature Communications*, Vol 8, pp. 14989 (2017)

8) Jinsoo Kim†, **Hyeokjun Park**†, Byungju Lee, Won Mo Seong, Hee-Dae Lim, Youngjoon Bae, Haegyeom Kim, Won Keun Kim, Kyoung Han Ryu and Kisuk Kang "Dissolution and ionization of sodium superoxide in sodium–oxygen batteries", *Nature Communications*, Vol 7, pp. 10670 (2016)

9) Hee-Dae Lim†, **Hyeokjun Park**†, Hyungsub Kim, Jinsoo Kim, Byungju Lee, Youngjoon Bae, Hyeokjo Kwon and Kisuk Kang "A New Perspective on Li–SO_2 Batteries for Rechargeable Systems", *Angewandte Chemie International Edition*, Vol 54, pp. 9663-9667 (2015)

(2) Journals (Contributing author)

† These authors contributed equally.

1) Sehwan Moon†, Orapa Tamwattana†, **Hyeokjun Park**, Gabin Yoon, Won Mo Seong, Kyu-Young Park, Nonglak Meethong and Kisuk Kang “An auxiliary electrode for safe lithium metal batteries”, In preparation (2019)
2) Youngmin Ko, **Hyeokjun Park**, Sung Kwan Park, Youngjoon Bae, Byungju Lee and Kisuk Kang "Comparative kinetic study of redox mediators for high-power lithium–oxygen batteries", Submitted (2019)
3) Zheng-Long Xu, Gabin Yoon, Kyu-Young Park, **Hyeokjun Park**, Orapa Tamwattana, Sung Joo Kim, Won Mo Seong and Kisuk Kang "Tailoring sodium intercalation in graphite for high energy and power sodium ion batteries", Submitted (2019)
4) Myeong Hwan Lee†, Sung Joo Kim†, Donghee Chang, Sehwan Moon, Kyungbae Oh, Kyu-Young Park, Won Mo Seong, **Hyeokjun Park**, Giyun Kwon, Byungju Lee and Kisuk Kang "Toward a low-cost high-voltage sodium aqueous rechargeable battery", *Materials Today*, under review (2018)
5) Youngmin Ko, **Hyeokjun Park**, Jinsoo Kim, Hee-Dae Lim, Byungju Lee, Giyun Kwon, Sechan Lee, Youngjoon Bae, Sung Kwan Park and Kisuk Kang "Biological redox mediation in electron transport chain of bacteria for oxygen reduction reaction catalysts in lithium–oxygen batteries", *Advanced Functional Materials*, 1805623 (2018)
6) Mi Young Oh, Sung Kwan Park, **Hyeokjun Park**, Hanbit Kim, Kisuk Kang,

Kwang Chul Roh and Tae Ho Shin "Enhancement of oxygen reduction reaction catalytic activity via the modified surface of $La_{0.6}Sr_{0.4}Co_{0.2}Fe_{0.8}O_{3-\delta}$ with Palladium nanoparticles as cathode for lithium–air battery", *ACS Applied Energy Materials*, Vol 1, pp. 5518-5526 (2018)

7) Kyeongse Song†, Jaepyeong Jung†, Mihui Park, **Hyeokjun Park**, Hyung-Jin Kim, Sang-Il Choi, Junghoon Yang, Kisuk Kang, Young-Kyu Han and Yong-Mook Kang "Anisotropic surface modulation of Pt catalysts for highly reversible Li-O_2 batteries; High index facet as a critical descriptor", *ACS Catalysis*, Vol 8, pp. 9006-9015 (2018)

8) Kyojin Ku†, Jihyun Hong†, Hyungsub Kim, **Hyeokjun Park**, Won Mo Seong, Sung-Kyun Jung, Gabin Yoon, Kyu-Young Park, Haegyeom Kim and Kisuk Kang "Suppression of voltage decay through manganese deactivation and nickel redox buffering in high-energy layered lithium-rich electrodes", *Advanced Energy Materials*, Vol 8, pp. 1800606 (2018)

9) Won Mo Seong, Kyu-Young Park, Myeong Hwan Lee, Sehwan Moon, Kyungbae Oh, **Hyeokjun Park**, Sechan Lee and Kisuk Kang "Abnormal self-discharge in lithium-ion batteries", *Energy and Environmental Science*, Vol 11, pp. 970-978 (2018)

10) Youngjoon Bae, Dong-Hyun Ko, Sunyoung Lee, Hee-Dae Lim, Yun-Jung Kim, Hyun-Soo Shim, **Hyeokjun Park**, Youngmin Ko, Sung Kwan Park, Hyuk Jae Kwon, Hyunjin Kim, Hee-Tak Kim, Yo-Sep Min, Dongmin Im and Kisuk Kang "Enhanced Stability of Coated Carbon Electrode for Li-O_2 Batteries and Its

Limitations", *Advanced Energy Materials*, Vol 8, pp. 1702661 (2018)

11) Sangmin Kang†, Kyungmi Lim†, **Hyeokjun Park**, Jong Bo Park, Seong Chae Park, Sung-Pyo Cho, Kisuk Kang and Byung Hee Hong "Roll-to-roll laser-printed graphene-graphitic carbon electrodes for high-performance supercapacitors", *ACS Applied Materials & Interfaces*, Vol 10, pp. 1033-1038 (2018)

12) Hee-Dae Lim†, Byungju Lee†, Youngjoon Bae, **Hyeokjun Park**, Youngmin Ko, Haegyoen Kim, Jinsoo Kim and Kisuk Kang "Reaction chemistry in rechargeable Li-O_2 batteries", *Chemical Society Reviews*, Vol 46, pp. 2873-2888 (2017)

13) Youngjoon Bae†, Young Soo Yun†, Hee-Dae Lim, Hongkyung Lee, Yun-Jung Kim, Jinsoo Kim, **Hyeokjun Park**, Youngmin Ko, Sungho Lee, Hyuk Jae Kwon, Hyunjin Kim, Hee-Tak Kim, Dongmin Im and Kisuk Kang "Tuning the Carbon Crystallinity for Highly Stable Li-O_2 Batteries", *Chemistry of Materials*, Vol 28, pp. 8160-8169 (2016)

(3) Conferences

1) **HyeokJun Park**, Hee-Dae Lim and Kisuk Kang, The Korean Electrochemical Society 2014 Spring meeting (Changwon, Republic of Korea, April1 10-12, 2014), Poster presentation, "A Catalyst-embedded Hierarchical Air Electrode for High-performance Li−O_2 Batteries"
2) Hee-Dae Lim, **Hyeokjun Park**, Hyelynn Song, Jinsoo Kim, Hyeokjo Gwon, Yong Hyup Kim and Kisuk Kang, NANO KOREA 2014 (Seoul, Republic of Korea, July 2-4, 2014), Poster presentation, "A New Catalyst-embedded Hierarchical Air Electrode for High-performance Li−O_2 Batteries"
3) **Hyeokjun Park**, Hee-Dae Lim, Hyungsub Kim, Jinsoo Kim, Byungju Lee, Youngjoon Bae, Hyeokjo Gwon and Kisuk Kang, IUPAC-2015, 45th World Chemistry Congress (Busan, Republic of Korea, August 9-14, 2015), Oral presentation, "A new perspective on Li-SO_2 batteries for rechargeable systems"
4) **Hyeokjun Park**, Hee-Dae Lim, Hyungsub Kim, Jinsoo Kim, Byungju Lee, Youngjoon Bae and Kisuk Kang, International Symposium on Emerging Functional Materials 2015 (Songdo, November 4-6, 2015), Poster presentation, "A New Perspective for Rechargeable Li-SO_2 batteries"
5) **Hyeokjun Park**, Hee-Dae Lim, Hyungsub Kim, Jinsoo Kim, Byungju Lee, Youngjoon Bae, Hyeokjo Gwon and Kisuk Kang, Materials Research Society 2015 Fall Meeting (Boston, United States of America, November 29-December 4, 2015), Oral presentation "A New Perspective on Rechargeable Li-SO_2 batteries"

6) **Hyeokjun. Park**, Jinsoo. Kim, Byungju. Lee, Hee-Dae Lim, Young Joon. Bae, Won Keun. Kim, Kyoung Han. Ryu and Kisuk. Kang, The Korean Electrochemical Society 2016 Spring Meeting (Gwangju, South Korea, April 7-9, 2016), Oral presentation, "Dissolution and ionization of sodium superoxide (NaO_2) in sodium-oxygen batteries"

7) **Hyeokjun Park**, Jinsoo Kim, Byungju Lee, Won Mo Seong, Hee-Dae Lim and Kisuk Kang, The Korean Society of Industrial and Engineering Chemistry 2016 Spring meeting (Yeosu, Republic of Korea, May2-4, 2016), Poster presentation, "Dissolution and ionization of sodium superoxide (NaO_2) in sodium-oxygen batteries"

8) **Hyeokjun Park**, Jinsoo Kim, Byungju Lee, Won Mo Seong, Hee-Dae Lim, Youngjoon Bae and Kisuk Kang, International Conference on Electronic Materials and Nanotechnology for Green Environment 2016 (Jeju, Republic of Korea, November 6-9, 2016), Oral presentation, "Dissolution and Ionization of Sodium Superoxide (NaO_2) in Non-aqueous Sodium-oxygen Batteries"

9) **Hyeokjun Park**, Hee-Dae Lim, Hyung Kyu Lim, Youngjoon Bae, Hyungjun Kim and Kisuk Kang, The Electrochemical Society 231st ECS Spring meeting (New Orleans, United States of America, May 28-June 1, 2017), Oral presentation, "High-Performance Rechargeable Lithium-Sulfur Dioxide Batteries Exploiting Conventional Carbonate-Based Electrolytes"

10) **Hyeokjun Park**, Hee-Dae Lim, Hyung Kyu Lim, Hyungjun Kim and Kisuk Kang, 2017 Fall Conference of the Korean Institute of Metals and Materials

(Daegu, Republic of Korea, October 25-27, 2017), Poster presentation, "Superior efficiency and power of rechargeable Li-SO_2 batteries exploiting conventional carbonate-based electrolytes"

11) **Hyeokjun Park**, Hee-Dae Lim, Hyung Kyu Lim, Hyungjun Kim and Kisuk Kang, The Korean Electrochemical Society 2017 Fall meeting (Daejeon, Republic of Korea, November 2-4, 2017), Poster presentation, "High-performance Li-SO_2 Batteries Exploiting Conventional Carbonate-based Electrolytes"

12) **Hyeokjun Park**, Hee-Dae Lim, Hyung Kyu Lim, Hyungjun Kim and Kisuk Kang, Materials Research Society 2017 Fall Meeting (Boston, United States of America, November 26-December 1, 2017), Poster presentation, "High-performance Lithium-Sulfur Dioxide Batteries Exploiting Conventional Carbonate-based Electrolytes"

13) **Hyeokjun Park**, Hee-Dae Lim, Hyung Kyu Lim, Hyungjun Kim and Kisuk Kang, Gordon Research Conference 2018 Electrochemistry (Ventura, United States of America, January 6-12, 2018), Poster presentation, "Superior efficiency and power of Li-SO_2 batteries exploiting conventional carbonate-based electrolytes"

14) **Hyeokjun Park**, Hee-Dae Lim, Hyung Kyu Lim, Hyungjun Kim and Kisuk Kang, International Battery Association 2018 (Jeju, Republic of Korea, March 11-16, 2018), Poster presentation, "Superior efficiency and power of rechargeable Li-SO_2 batteries exploiting conventional carbonate-based

electrolytes”

15) **Hyeokjun Park**, Jinsoo Kim, Myeong Hwan Lee, Youngmin Ko and Kisuk Kang, Americas International Meeting on Electrochemistry and Solid State Science (AIMES) 2018 (Cancun, Mexico, September 30-October 4, 2018), Oral presentation, “Highly Durable and Stable Sodium Superoxide in Concentrated Electrolytes for Sodium–Oxygen Batteries”

16) **Hyeokjun Park**, Sehwan Moon, Gabin Yoon and Kisuk Kang, Americas International Meeting on Electrochemistry and Solid State Science (AIMES) 2018 (Cancun, Mexico, September 30-October 4, 2018), Poster presentation, “Simple and Effective Gas-Phase Doping for Lithium Metal Protection in Lithium Metal Batteries”

17) **Hyeokjun Park**, Hee-Dae Lim and Kisuk Kang, Winter School 2019 - Nanomaterials for Energy Storage and Conversion (Tel Aviv, Israel, January 14–17, 2019), Poster presentation, “New Perspectives on SO_2 Chemistry for Rechargeable Batteries”

(4) Patents

1) “액체 촉매가 포함된 충전가능한 리튬-이산화황 전지 / Rechargeable Li-SO2 battery with soluble catalyst”

   - Korean Patent, [KR] Registration Number 1017902450000

2) “리튬 이차전지용 전해질 및 이를 포함하는 리튬 이차전지 / ELECTROLYTE FOR LITHIUM SECONDARY BATTERY AND SECONDARY BATTERY COMPROSING THE SAME”

   - Korean Patent, [KR] Application Number 1020170039357

3) “고농도 전해질을 포함하는 나트륨 공기 전지 / A SODIUM AIR BATTERY COMPRISING HIGH-CONCENTRATION ELECTROLYTE”

   - Korean Patent, [KR] Application Number 1020170063848

   - United States of America Patent [US] Application Number 15/845807

   - China Patent [CN] Application Number 201711402729.1

4) “보조전극 센서를 포함하는 이차전지 및 이차전지의 이상 검출 방법 / SECONDARY BATTERY CONTAINING AUXILIARY ELECTRODE SENSOR AND DETECTION METHOD FOR A SHORT CIRCUIT OF SECONDARY BATTERY”

   - Korean Patent, [KR] Registration Number 1019229920000

   - United States of America Patent [US] Application Number 16/052455